RESEARCH ARTICLE

Sediment waves and the gravitational stability of volcanic jets

Johan T. Gilchrist[1] · A. Mark Jellinek[1]

Abstract

It is increasingly recognized that the gravitational stability of explosive eruption columns is governed by complex ash-pumice-gas (multiphase) interactions as well as the mechanics of turbulent entrainment in the lower momentum-driven (fountain) and upper buoyancy-driven (plume) regions of typical Plinian eruption columns (volcanic jets). We use analog experiments on relatively dense mono- and bi-disperse particle-freshwater and particle-saltwater jets injected into a linearly stratified saltwater layer to revisit, characterize and understand how transitions among Buoyant Plume (BP), Total Collapse (TC) and Partial Collapse (PC) multiphase jet regimes in a traditional source strength $(-Ri_0)$ - particle concentration (ϕ_0) parameter space are modified by particle inertial effects expressed through a Stokes number (St) and particle buoyancy effects expressed through a Sedimentation number (Σ). We show that "coarse particles" $(1.4 \leq St \leq 6.0)$ enhance entrainment and modify significantly published conditions favoring BP and TC jets. Furthermore, the transition between BP and TC regimes occurs smoothly over a PC regime that extends a large $-Ri_0 \leftrightarrow \phi_0$ parameter space. Large volume annular sedimentation waves excited periodically at the fountain-plume transition height and the cloud level of neutral buoyancy (LNB) in PC and TC regimes lead to "phoenix clouds" spreading at multiple altitudes and build terraced deposits. Applied to volcanic jets, we develop a new set of conceptual models for jets in the BP, TC and PC regimes that make explicit links among source parameters, column heights, sedimentation wave properties, cloud structures and deposit architectures. These conceptual models make predictions for cloud structures and deposit characteristics that agree with observations made for well-studied historic and pre-historic eruptions and explain the origin of common but enigmatic features of proximal explosive eruption deposits, such as alternating air-fall and pyroclastic flow layering in subaerial deposits and terracing in submarine Catastrophic-Caldera Forming (CCF) eruption deposits. Additionally, our models provide guidance for real-time monitoring of eruption column stability for eruptions undergoing a typical BP→PC→TC regime evolution and predict pyroclastic flows to occur more frequently as columns transition from the PC→TC regime. Our experimental results combined with scaling considerations expressed through a set of new conceptual models provide exciting new pathways for future laboratory-, computer- and field-based studies of explosive eruptions.

Keywords Explosive eruptions · Entrainment · Column collapse · Sediment waves · Pyroclastic density currents · Terraced deposits · Multiply layered ash clouds · Phoenix clouds

Introduction

Explosive volcanic eruptions inject columns of rock fragments, pumice and ash (tephra), and volcanic gases into the atmosphere and ocean (Fig. 1a–c; Woods 2010; White et al. 2015). Extensive studies carried out over the last few decades show that the proclivity of such events to lead to devastating pyroclastic density currents (PDCs) or to long-lived umbrella-shaped clouds of ash, pyroclasts and entrained gas (umbrella clouds) is governed by spatially averaged "source parameters" including the mass flow rate, mixture density, particle volume fraction and particle size distribution (PSD), time-averaged "environmental conditions" including the atmospheric density stratification and wind stress conditions (e.g. Woods 1995; Suzuki 2005; Woods 2010; Carazzo and Jellinek 2012; Degruyter and Bonadonna 2013; Suzuki and Takehiro 2013; Cioni and Pistolesi 2015; Roche et al.
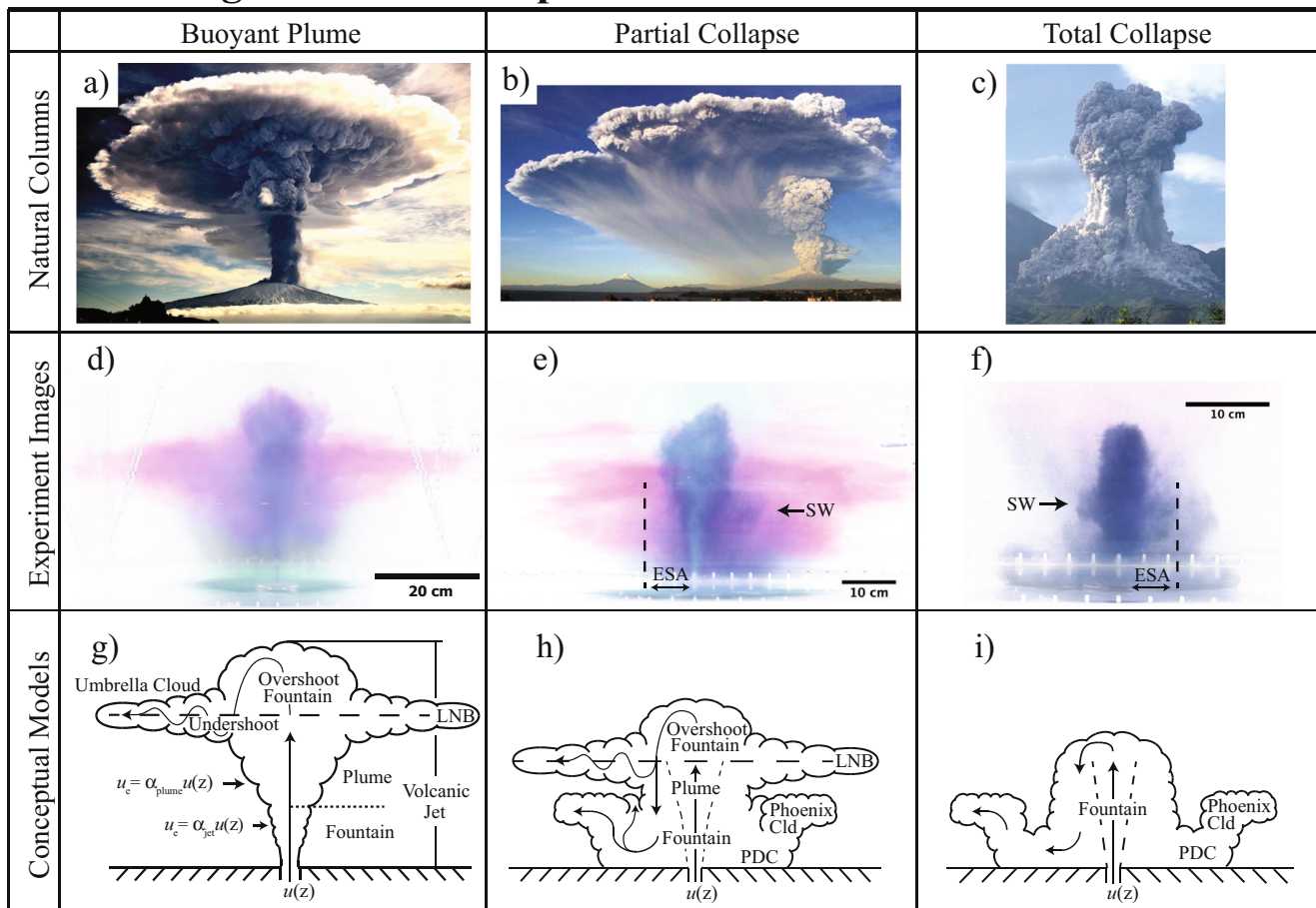
✉ Johan T. Gilchrist
  jgilchri@eoas.ubc.ca

[1] Department of Earth, Ocean and Atmospheric Sciences, Faculty of Science, University of British Columbia, Vancouver, BC, Canada

Column Regimes and Conceptual Models

Fig. 1 **Top panel:** images of natural eruptions showing three regimes of explosive eruptions: Buoyant Plume (left column), Partial Collapse (middle column) and Total Collapse (right column). (a) Buoyant Plume (BP) regime where erupted mass rises to spread in the atmosphere as an "umbrella cloud" (December 4, 2015 eruption of Mt Etna, Italy; photo courtesy of Giuseppe Famiani). (b) Partial Collapse (PC) regime where erupted mass is partitioned between buoyant rise and dense collapse in the eruption column, feeding an umbrella cloud and pyroclastic flows simultaneously (April 22–23, 2015 eruption of Calbuco Volcano, Chile). Reprinted from Castruccio et al. (2016) by permission from Springer Nature. (c) Total Collapse regime where erupted mass collapses back to Earth to form pyroclastic flows (August 16, 2016 eruption of Santiaguito Volcano, Guatemala; photo courtesy of CONRED, Guatemala). **Middle panel:** Color inverted images of experiments with multiphase jet columns in the BP, PC and TC regimes. Black arrows mark sediment waves (SW) and dashed line marks outer boundary of enhanced settling annulus (ESA). Particle-fluid mixtures appear blue and spreading jet fluid appears pink. (d) Jet in the BP regime where the injected mass spreads into an umbrella cloud before particles settle individually to the tank base. (e) Jet in the PC regime where jet mixture is partitioned simultaneously between dense collapse via sediment waves and buoyant rise to spread into clouds. (f) Jet in the TC regime where > 90% of the jet mixture collapses to the tank base via sediment waves. Sediment waves transform into gravity currents along the tank base with phoenix clouds ascending above and spreading into phoenix cloud layers. **Bottom panel:** Conceptual models of multiphase jet regimes. (g) Sketch of eruption column in the BP regime. Lower dashed line marks boundary between jet and plume regions of the column where a buoyancy reversal of the mixture occurs and above which entrainment is enhanced ($\alpha_{jet} < \alpha_{plume}$). The BP mixture ascends above the level of neutral buoyancy (LNB) and enters the overshoot (OS) region. The mixture then descends to the LNB to spread away from the jet axis into an umbrella cloud. (h) Jet in the PC regime with an overshoot region above the LNB that where mixture is simultaneously partitioned into a spreading umbrella cloud and collapse around the column. The collapsing mixture descends to the ground and spreads as pyroclastic flows with phoenix clouds ascending above. (i) Jet in the TC regime with spreading pyroclastic flows and ascending phoenix clouds, but no umbrella cloud. For all sketches, arrows on left side show direction of jet mixture flow through the overshoot, umbrella cloud, LNB and phoenix cloud regions. The boundary of the jet is marked by diagonal dashed lines extending from the nozzle at the tank base

2013, Aubry et al. 2017a, 2017b), as well as the mechanics of atmospheric entrainment and mixing, which are governed by lateral variations in velocity, mean density and median particle size across jet edges (Fig. 1 Morton et al. 1956; Turner 1986; Carazzo et al. 2010; Jessop and Jellinek 2014).

However, in addition to these source and environmental conditions, recent work also highlights key microphysical and vent geometrical controls on eruptive behavior, which arise in response to the characters of particle-size distributions and the subtle dynamics of particle ↔ fluid and

particle ↔ particle interactions (Carazzo and Jellinek 2012; Carazzo et al. 2014; Carazzo et al. 2014; Girault et al. 2014; Jessop and Jellinek 2014; Lherm and Jellinek 2019).] Crucially, as our understanding of the major controls on eruption behavior grows, an acute emerging issue is that our ability to predict confidently whether a given eruption will more likely produce PDCs, tropospheric or stratospheric ash clouds or combinations of all three behaviors is unclear. Consequently, our ability to forecast or assess, for example, PDC hazards to local populations (Dufek et al. 2015; Cole et al. 2015), short-term ash hazards to air travel (Prata and Bill 2015), longer term contributions to decadal or millenial climate variability (Robock 2015; Ridley et al. 2014; Aubry et al. 2016; Prata et al. 2017) as well as the reality of profound volcanically induced shifts in Earth's climate and biosphere (Rampino and S. Self 1992; Huybers and Langmuir 2009; Schmidt et al. 2010; Schmidt et al. 2012; Black et al. 2015; Newhall et al. 2018) is limited.

The character, magnitude and longevity of volcanic effects depend on how the erupted mass is transported after leaving the vent. It is widely recognized that with sufficient atmospheric entrainment, volcanic jets can undergo a buoyancy reversal, causing the otherwise dense mixture erupted as a momentum-driven fountain to continue rising as a turbulent buoyant plume (Fig. 1a & g; Morton et al. 1956; Turner 1966; Woods 2010). Where buoyant plumes rise to a level of neutral buoyancy (LNB) height in the atmosphere, their momentum causes them to oscillate ("overshoot" and "undershoot") about this LNB height as they spread as a gravity current (Fig. 1g; see oscillation of initial spreading of pink cloud in Supplemental Video 4; see Supplemental Videos in Carazzo and Jellinek 2012). We will use "volcanic jet" to refer to the upward flow of material forming the eruption column, "fountain" and "overshoot fountain" to refer to the momentum-driven lower part and overshoot region of the volcanic jet. We use "plume" for the part of the jet that is buoyancy-driven (Fig. 1g). Consistent with the expectation of a discrete fountain-plume transition, evident in experiments on particle-free and particle-laden analog jets, explosive eruptions are generally classified into two end-member regimes (cf. Woods 2010; Carazzo and Jellinek 2012; Jessop et al. 2016: 1) the "Buoyant Plume" (BP) regime where the volcanic jet rises as a plume to form a gravitationally stable and long-lived atmospheric umbrella cloud (Carey and Bursik 2015; Bonadonna et al. 2015); and 2) the "Total Collapse" (TC) regime in which a gravitationally unstable volcanic jet rises as a fountain that collapses to form devastating PDCs and more dilute pyroclastic surges (both referred to as "pyroclastic flows" hereafter) (Fig 1c & i; Dufek et al. 2015). A key new prediction from the experiments in this study is that particle-laden jets entering a stratified environment akin to Earths troposphere will collapse to varying extents

in periodic and aperiodic (intermittent) annular waves of particles and entrained jet fluid (sedimentation waves) that descend around the volcanic jet (marked SW in Fig. 1e–f; Supplemental Video 3; Section 3.2).

Assuming that there is a discrete transition from the BP to TC regime makes it possible to define critical source and environmental conditions defining this regime boundary (Woods 1995; Carazzo and Jellinek 2012). Distinct tephra layers in explosive eruption deposits can be used to characterize deposits in terms of BP or TC eruption dynamics (Houghton and Carey 2015; Dufek et al. 2015). In the BP regime, depending on their size, pyroclastic particle loss from umbrella clouds is by individual settling particle aggregation or by convective fingering processes (Hoyal et al. 1999; Durant et al. 2008; Carazzo and Jellinek 2012; 2013; Manzella et al. 2015; Scollo et al. 2017). Although both processes produce tephra fall deposits that mantle topography, individual settling of larger than order 100-µm particles produces a deposit that smoothly decreases in thickness with increasing distance from the vent (e.g. Lirer et al. 1973; Bonnecaze et al. 1995; Bonadonna et al. 1998; Hoyal et al. 1999), whereas convective fingering or diffusive convective loss of ash and fine produce deposits that can thicken or thin over distances of kilometers both with distance from the vent, as well as with azimuth. Generally for BP deposits, median pumice and maximum lithic size, as well as the standard deviation of particle size, decrease with increasing distance from the eruption source (Walker and Croasdale 1970; Walker 1973; Papale and Mauro 1993; Di Muro et al. 2008; Houghton and Carey 2015). By contrast, in the TC regime, mass is transported predominantly by pyroclastic flows, which can form laterally continuous or discontinuous layers with characteristic features including cross-cutting relationships indicating flow direction. Deposits can have thicknesses that vary abruptly both in the direction of flow and in cross-flow directions, fill local topographical lows and thin over local topographical highs. In addition, median pumice size, maximum lithic size and their standard deviation do not vary systematically with distance from their vent Carazzo and Jellinek (2012, 2013).

However, despite the existence of compelling examples of sharp BP-TC transitions related to some of the largest events in the geological record (Hahn et al. 1979; Aramaki 1984; Fisher et al. 1993), such discrete transitions are not general features of deposits related to well-documented explosive volcanic eruptions (Carey et al. 1990; Wilson 2001; Cioni et al. 2003; Houghton et al. 2004; Hildreth and Fierstein 2012; Castruccio et al. 2016; Edgar et al. 2017). The 0.8 ka Quilotoa, Ecuador eruption is a prime example of a complex BP-TC transition. Although exposures of distal tephra fall units in the deposit are typical air-fall units produced in a BP regime (Fig. 3a), proximal exposures

are constructed of alternating air-fall and pyroclastic flow units that record intermittent as well as abrupt BP ↔ TC transitions to transient eruptive conditions of varying longevity (Di Muro et al. 2008). Such textural oscillations over the full height of these deposits cannot be easily reconciled with sedimentation predominantly in either BP or TC regimes but is consistent with the majority of this eruption operating in a PC regime in which both behaviours occur (Neri and Dobran 1994; Kaminski and Jaupart 2001; Neri et al. 2002; Di Muro et al. 2004; Carazzo and Jellinek 2012).
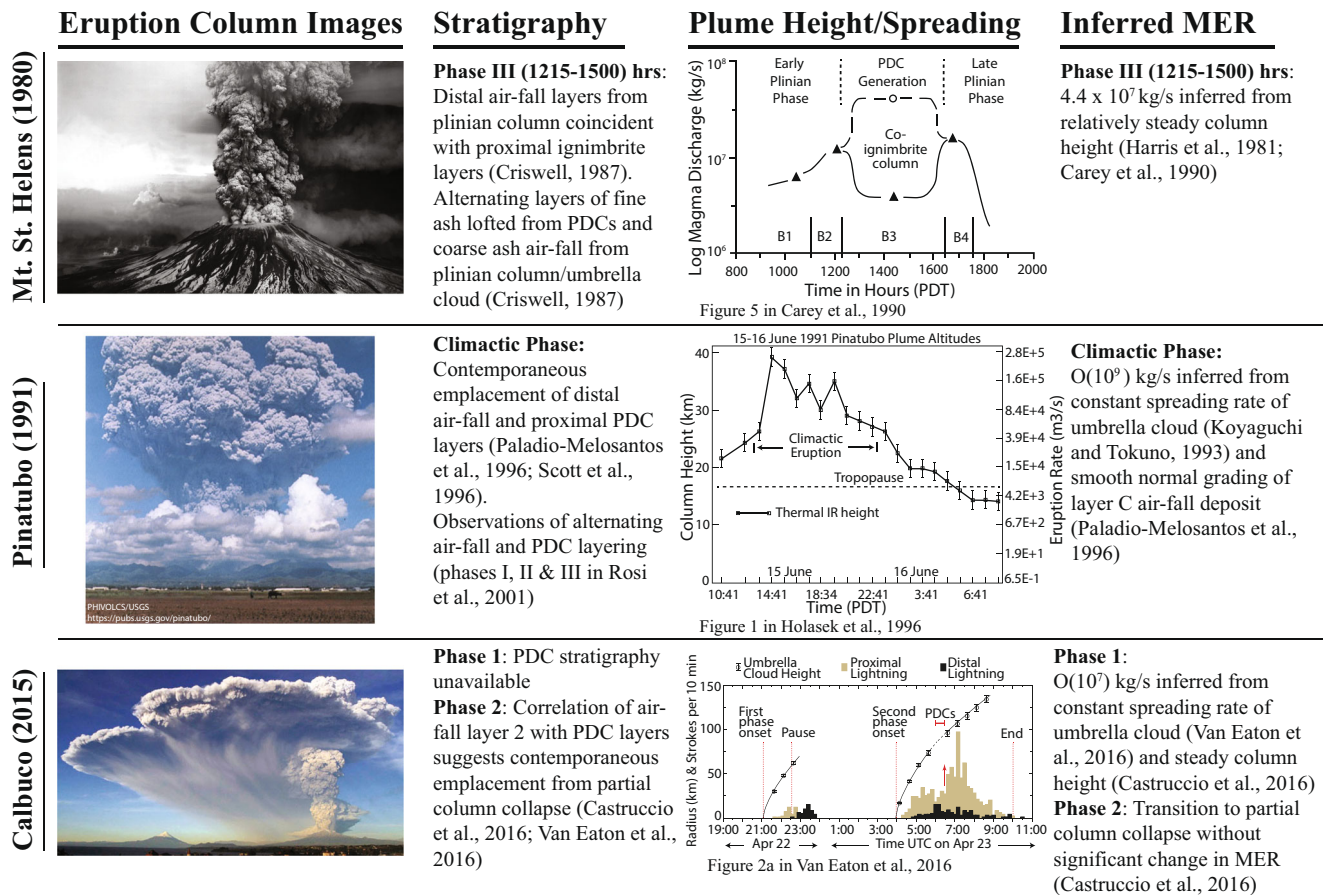
Further evidence for the existence and persistence of a PC eruption column regime is reviewed by (Kaminski and Jaupart 2001), who compile observations of deposit architectures for ten well-studied eruptions that all display alternating air-fall and pyroclastic flow layering in proximal deposits, which are defined to be within the furthest lateral extent of pyroclastic flow units (Fisher and Schmincke 1984; Cas and Wright 1987; Houghton and Carey 2015; Brown and Andrews 2015). Examples include the Bishop Tuff (0.76 Ma; Wilson and Hildreth 1997), Fogo A (4.6 ka; Walker and Croasdale 1970), Taupo (1.8 ka Wilson 1993), Veusvius (1.9 ka; Thomas et al. 2011), Novarupta (1912; Hildreth and Fierstein 2012), Mount St. Helens (1980 Carey et al. 1990) and El Chichon (1982; Sigurdsson et al. 1987) plinian eruption deposits. In addition to these eruptions and the 0.8 ka Quilotoa eruption discussed above, the eruption deposits of Las Cañadas caldera on Tenerife, Spain (312 ka), Mt. Pinatubo, Philippines (1991) and Calbuco Volcano, Chile (2015) also exhibit alternating air-fall and pyroclastic flow layering in proximal deposits (Rosi et al. 2001; Castruccio et al. 2016). Furthermore, visual observations of the eruptions of Mt. St. Helens (1980), Mt. Pinatubo (1991) and Calbuco (2015) record simultaneous spreading of an umbrella cloud at the top of the eruption column, multiple underlying ash cloud layers and pyroclastic flows at the base of the eruption column (first column in Fig. 2; Lipman and Mullineaux 1981; Castruccio et al. 2016). Since, Edgar et al. 2017 describe twenty-two intercalated air-fall and pyroclastic flow layers in the 312-ka eruption deposit of Las Cañadas caldera on Tenerife, Spain. Taken together, these observations indicate that alternating air-fall and pyroclastic flow layering are common features of proximal sub-plinian and plinian eruption deposits and suggest that pyroclastic flows occur intermittently or periodically with locations that vary around the vent during these eruptions. In addition, the simultaneous sedimentation by air-fall and pyroclastic flow processes makes any recognition of distinct airfall deposits challenging (Valentine and Giannetti 1995; Wilson and Hildreth 1998). This property suggests that proximal deposits characterized by pyroclastic flow layers are not strictly linked to the TC regime. More insightful, real-time observations (e.g. first and third column in Fig. 2) show that

the underlying eruption dynamics can occur concurrently, which is in marked contrast to conventional explanations involving an eruption column alternating between the end-member BP and TC regimes in response to periodic shifts in, say, source parameters (Woods 2010).

Alternating air-fall-pyroclastic flow layering in proximal deposits, together with inferred approximately constant eruption source parameters (Carey et al. 1990; Holasek et al. 1996; Rosi et al. 2001; Castruccio et al. 2016; Van Eaton et al. 2016), support a hypothesis that the simultaneous production of multiply layered ash clouds and pyroclastic flows are inherent features of the dynamics of quasi steady-state volcanic jets operating in a PC regime (Neri and Dobran 1994; Kaminski and Jaupart 2001; Neri et al. 2002; Di Muro et al. 2004; Di Muro et al. 2008; Ogden et al. 2008; Carazzo and Jellinek 2012; Van Eaton et al. 2012; Suzuki et al. 2016). Neri and Dobran (1994) were first to address the extent to which this combined behavior may be a consequence of the multiphase character of volcanic jets. In numerical simulations of monodisperse particle-gas fountains under conditions appropriate for a range of plinian eruptive behaviors, they identify periodic oscillations of mixture density, velocity and particle volume fraction excited both within and along the edges of model eruption columns. These authors attribute this behavior to effects of the re-entrainment of collapsing material in a zone of recirculation adjacent to the jet (see Figs. 5 and 6 in their study). However, power spectra of velocity oscillations at the top of the collapsing column shows multiple distinct peaks that are not harmonics, suggesting that multiple underlying processes are at work in their simulations.

More recently, Veitch and Woods (2000) revisit effects of a plume re-entraining particles settling from a spreading umbrella cloud (see Fig. 1 in their study) in analogue experiments on multiphase buoyant plumes. They show that when source parameters are near the BP-TC regime boundary, periodic column collapse can occur potentially as a result of destabilizing buoyancy effects arising through the re-entrainemnt of dense particle-fluid mixtures descending along the plume margins. In experiments on multiphase jets near the BP-TC regime in 2-layer systems, Carazzo and Jellinek (2012; see their Fig. 6) show that "late collapse" of initially stable umbrella clouds can occur where the flow rate of entrained particles delivered by jets from the overshoot region into gravitationally unstable particle boundary layers forming at the cloud base is sufficiently large.

Visual observations during the onset of the eruptions of Mt. Pinatubo (1991) and Calbuco (2015) show multiple ash clouds and pyroclastic flows spreading from the lower half of the eruption column before significant airfall from the overlying umbrella cloud interacts with the lower half of the column (see eruption column images

Eruption Column Images	**Stratigraphy**	**Plume Height/Spreading**	**Inferred MER**

Mt. St. Helens (1980)

Stratigraphy: **Phase III (1215-1500) hrs**: Distal air-fall layers from plinian column coincident with proximal ignimbrite layers (Criswell, 1987). Alternating layers of fine ash lofted from PDCs and coarse ash air-fall from plinian column/umbrella cloud (Criswell, 1987)

Plume Height/Spreading: Figure 5 in Carey et al., 1990

Inferred MER: **Phase III (1215-1500) hrs**: 4.4×10^7 kg/s inferred from relatively steady column height (Harris et al., 1981; Carey et al., 1990)

Pinatubo (1991)

Stratigraphy: **Climactic Phase:** Contemporaneous emplacement of distal air-fall and proximal PDC layers (Paladio-Melosantos et al., 1996; Scott et al., 1996). Observations of alternating air-fall and PDC layering (phases I, II & III in Rosi et al., 2001)

Plume Height/Spreading: 15-16 June 1991 Pinatubo Plume Altitudes. Figure 1 in Holasek et al., 1996

Inferred MER: **Climactic Phase:** $O(10^9)$ kg/s inferred from constant spreading rate of umbrella cloud (Koyaguchi and Tokuno, 1993) and smooth normal grading of layer C air-fall deposit (Paladio-Melosantos et al., 1996)

Calbuco (2015)

Stratigraphy: **Phase 1**: PDC stratigraphy unavailable. **Phase 2**: Correlation of air-fall layer 2 with PDC layers suggests contemporaneous emplacement from partial column collapse (Castruccio et al., 2016; Van Eaton et al., 2016)

Plume Height/Spreading: Figure 2a in Van Eaton et al., 2016

Inferred MER: **Phase 1**: $O(10^7)$ kg/s inferred from constant spreading rate of umbrella cloud (Van Eaton et al., 2016) and steady column height (Castruccio et al., 2016). **Phase 2**: Transition to partial column collapse without significant change in MER (Castruccio et al., 2016)

Fig. 2 Three well-studied subplinian/plinian eruptions with climactic phases occuring in the PC regime. **Top panel:** Mt. St. Helens (1980), **middle panel:** Pinatubo (1991) and **bottom panel:** Calbuco (2015). **Columns** from left to right are images of eruption column, stratigraphic features linked to PC regime, plume height and umbrella cloud spreading rate time series, and inferred MER. Photos of Mt. St. Helens (1980) and PInatubo (1991) are from the U.S. Geological Survey. Photo of Calbuco (2015) reprinted from Castruccio et al. (2016) by permission from Springer Nature. Plume height graph for Mt. St. Helens (1980) modified from Carey et al. (1990) with permission from Elsevier. Plume height graph for Pinatubo (1991) modified from Holasek et al. (1996) with permission from John Wiley and Sons. Umbrella cloud spreading graph for Calbuco (2015) reprinted from Van Eaton et al. (2016) with permission from John Wiley and Sons

in Fig. 2; https://www.youtube.com/watch?v=UsUKMtpq 3w8). These observations indicate that partial collapse of approximately the lower half of the eruption column, which involves the fountain region of the column, occurs before significant re-entrainment of air-fall from the overlying umbrella cloud occurs. Further evidence for partial collapse prior to air-fall re-entrainment can be found in the proximal deposit stratigraphy where, in both cases, pyroclastic flows were emplaced directly on pre-eruption material (e.g. bedrock or lahar deposits), indicating that either pyroclastic flows were active prior to the deposition of initial air-fall, which agrees with visual observations discussed above, or that pyroclastic flows scoured initial air-fall layers (Rosi et al. 2001; Castruccio et al. 2016). Rosi et al. (2001) note that "This is a feature of many other eruptions producing significant volumes of intraplinian flows such as the Bishop Tuff (Wilson and Hildreth 1997) and the Taupo AD186 eruption (Wilson and

Walker 1985)". The occurrence of partial collapse, combined with the simulations of Neri and Dobran (1994) provide strong evidence that oscillations in mixture density, velocity and particle volume fraction occur in the fountain region of an eruption column, which in turn lead to oscillations in the source parameters of the plume region of an eruption column, in contrast to the assumption of steady source parameters for the plume region in the re-entrainment model of Veitch and Woods (2000). Consequently, the mechanical link between the proposed mechanism for particle re-entrainment and partial column collapse is unclear and a basic question remains: What process drives the initial partial collapse of the lower fountain region of eruption columns in the PC and TC regimes and does this process continue to operate thereafter?

A clue for one underlying process is the recognition that turbulent fountains with statistically steady source parameters undergo periodic height fluctuations (see Supplemental
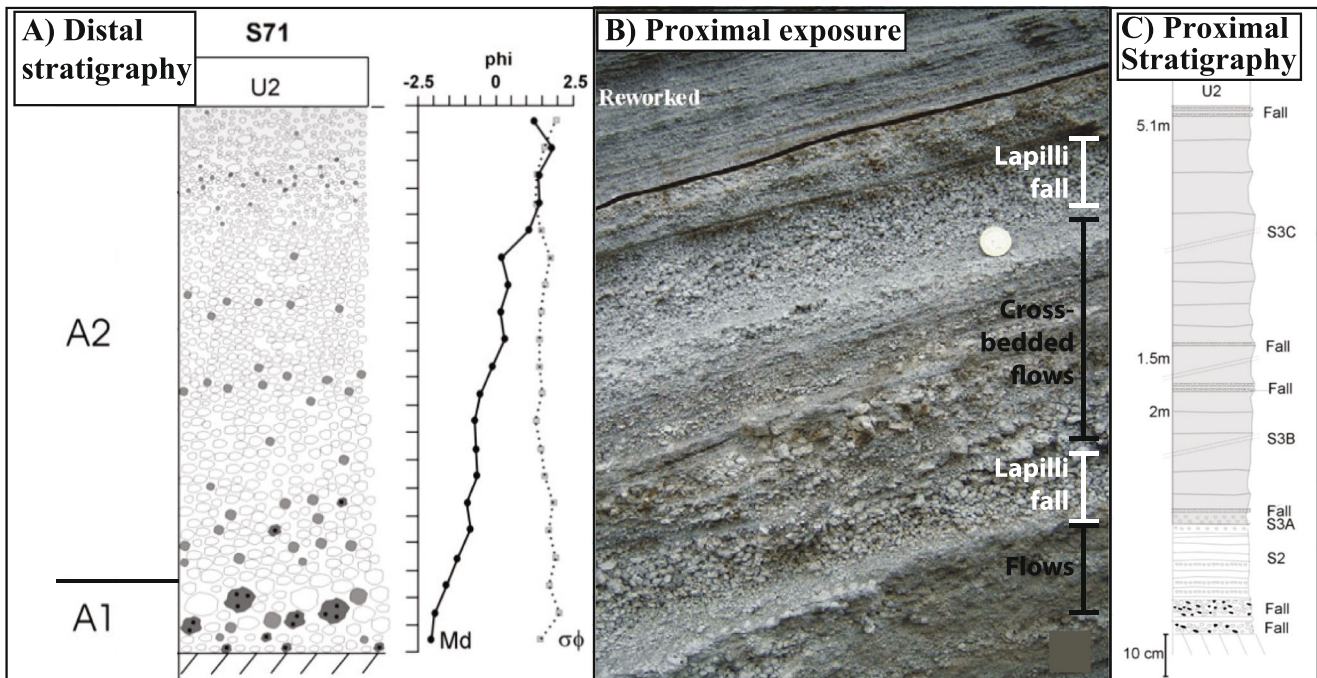
Fig. 3 (a) Stratigraphic section S71 illustrating general trends in the texture of the distal Unit 1 tephra fall sequence from the Quilotoa eruption in Ecuador (0.8 ka). Normally graded deposits, with median grain size (M_d) decreasing upwards, are characterized by particle size distributions with nearly constant standard deviations (σ_ϕ), consistent with expectations from sedimentation by individual particle settling in a BP regime. (b) A proximal exposure coeval with S71 section with alternating and sharply bounded tephra fall and pyroclastic flow layers. (c) Sketch of proximal stratigraphic section, from a location on the opposite side of the volcanic vent from exposure in (b), showing alternating tephra fall ("Fall") and pyroclastic flow ("S") layers for Unit 1. Reprinted from Di Muro et al. (2008) with permission from Elsevier

Video 1 in Hunt and Burridge 2015; Turner 1979; Baines et al. 1990; Bloomfield and Kerr 2000; Ogden et al. 2008; Burridge and Hunt 2013; Suzuki et al. 2016). Michaud-Dubuy et al. (2018) perform analogue experiments on salt-water fountains and on monodisperse particle-fresh water fountains to investigate whether the presence of low concentrations of 18–106-μm particles modifies this oscillatory behavior. These authors find that, for populations of particles with settling speeds that are much smaller than the mean fountain rise speed, particles remain entrained and fountain height oscillations and resultant mixture collapses are similar to particle-free cases. Applied to the dynamics of the lower fountain region of volcanic jets, these results suggest that whereas fine ash will not significantly affect the partial collapses related to jet height oscillations, the steady loss of larger particles may affect the buoyancy flux carried by descending pyroclastic density currents. Although insightful, Michaud-Dubuy et al. (2018) focus on particle buoyancy effects neglects well-known, potentially major effects of particle inertia, which will affect the character of particle-fluid coupling and, consequently, the distribution of particle mass loading and mixture buoyancy even in very dilute fountains (Crowe et al. 1995; Elghobashi and Truesdell 1993; Crowe et al. 1997; Raju and Meiburg 1997; Hwang and Eaton 2006; Balachandar and Eaton 2010;

Crowe et al. 2011; Hoque et al. 2016; Mallouppas et al. 2017; Del Bello et al. 2017).

Deposits emplaced by submarine caldera eruptions exhibit curious features that may provide important clues for building understanding of the predominant source condition controls on the lower fountain dynamics of column collapse in a TC regime. In particular, the surface topography of the proximal submarine deposits of Santorini, Greece (1.8 ka), Macauley Caldera, Kermandec Arc (5.7 ka) and Sumisu, Izu-Bonin Arc (30–60 ka) are each characterized by concentric terracing and are composed of unconsolidated and relatively coarse tephra (Wright et al. 2006; Tani et al. 2008; Hooft et al. 2019). Jessop et al. (2016) show that Catastrophic Caldera-Forming (CCF) eruptions have an increased tendency towards total collapse than eruptions from stratovolcanoes, as evinced by the relatively large ratio of pyroclastic flow volume relative to total erupted volume for CCF eruptions. The regular striking spacing of concentric terracing in submarine CCF deposits suggests a periodic rather than intermittent depositional process that potentially reflects expected fountain collapse dynamics discussed above. Forming reliable links between the architecture of CCF eruption deposits and the dynamics of their ancient eruption columns is key for hazard assessment of the largest explosive eruptions documented
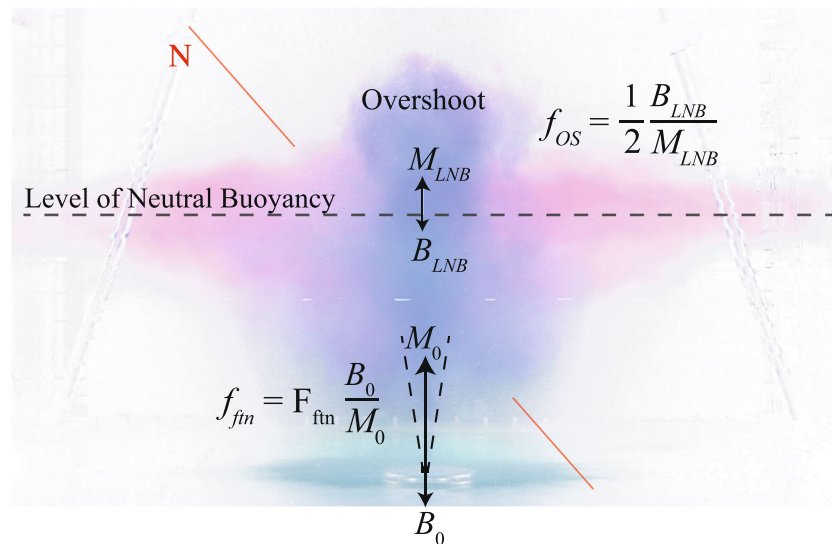
Fig. 4 Inverted color image of a multiphase jet in the BP regime with coarse particles $1.2 \leq \mathrm{St} \leq 4.9$ appearing blue, particle-free jet fluid appearing pink and coarse particle deposition on the tank base appearing blue-green. f_{ftn} and f_{OS} are the frequencies of oscillation in two regions of the jet column, above the source (subscript 0) and above the umbrella cloud spreading LNB, where the competing momentum, M_0, and buoyancy fluxes, B_0 drive fountain dynamics. N is the Brunt-Väisälä frequency of the ambient fluid density stratification. $F_{ftn} \approx 0.7$ is a geometric constant (Burridge and Hunt, 2013). The jet region is outlined with diagonal dashed lines and the horizontal dashed line marks the LNB. The maximum extent of blue-green particle deposition on the tank base indicates maximum distance of particle transport via the umbrella cloud from the jet axis

on Earth. However, to our knowledge, only one study (Pope et al. 2018) has investigated the emplacement mechanism of these striking deposits using insights gained from studies of turbidity currents to develop a conceptual model of terrace formation (Pope et al. 2018). Pope et al. (2018) refer to submarine concentric terracing features as "sediment waves". However, we reserve this term for the dynamic process of waves of sediment descending intermittently or periodically around jet columns (Fig. 4 1e–f).

In addition to the source parameters, entrainment of ambient air governs the evolution of the mean density of a turbulent volcanic jet as it rises and thus exerts a strong control over eruptive regime (Turner 1986; Woods 2010). The amount of air entrained into and mixed across an initially dense volcanic jet before the jet exhausts its intial momentum determines whether a jet undergoes a buoyancy reversal to rise as a plume. In turn, this can cause the jet to transition to buoyant rise and affect the proclivity for BP, PC or TC behavior (Fig. 1g–i). In developing the "entrainment hypothesis" (Morton et al. 1956) proposed that the rate of entrainment at any height is proportional to the mean rise speed of the plume

$$u_e(z) = \alpha_e u(z). \tag{1}$$

Here, α_e is a constant entrainment parameter and is generally order 0.1. Extensive measurements of α_e in particle-free jets show that the entrainment speed into plumes can be a factor of 2 larger than into fountains (Fig. 1g;

Turner 1966; Bloomfield and Kerr 1998; Linden 2000; Wang and Law 2002; Lin and Armfield 2004; Kaminski et al. 2005; Carazzo et al. 2006; Burridge and Hunt 2013). More importantly, recent studies show that α_e for multiphase jet analogues of eruption columns also varies significantly depending on particle inertial effects expressed through a Stokes number we discuss below ("Scaling natural volcanic jets to the laboratory setting"). In particular, simplified analogue experiments and numerical simulations show that whereas coarser particles (e.g. lapilli, $0.1 < \mathrm{St} < 10$) can enhance entrainment and increase a likelihood for buoyancy reversal an eruption in a BP regime, fine particles (e.g. ash, $\mathrm{St} < 0.01$) act to inhibit entrainment, enhancing a tendency for partial or total collapse (Jessop and Jellinek 2014; Cerminara et al. 2016; Jessop et al. 2016; Lherm and Jellinek 2019).

To make progress on key mechanical controls over the characters of multiphase jets erupting in BP, PC and TC regimes as well as expressions of these eruption dynamics in deposits we use analogue experiments, spectral analysis, scaling theory and simple models to address the following questions:

1. What critical source conditions, environmental conditions, particle volume fractions and median particle sizes reliably define BP and TC regimes and over what range of these conditions will transitional PC behavior occur?

2. How is a plausible BP-PC-TC regime diagram modified by variations in entrainment rates that depend on the presence and size of particles?

3. How are the differing dynamics of BP, TC, and PC regimes reliably distinguished in the structure of spreading ash clouds and architectures of resulting deposits?

We will show that the transition from BP to TC regimes occurs smoothly and over a broad PC parameter space. In particular, a principal discovery in experiments predominantly with coarse particles ($1.2 < \text{St} < 4.9$) is that descending annular "sediment waves" of varying size in all three regimes govern column collapse extent, cloud structure and deposit architecture. To facilitate a discussion of sedimentation near the edge of experimental jet columns, it will be useful to define an "enhanced settling annulus" region with an inner diameter bounded by the jet edge (cf. Turner 1966) and an outer diameter set by the maximum radius of falling sediment waves (marked ESA in Fig. 1d–f). Hereafter, the extent to which a jet occurs in the BP, TC or PC regime will be referred to as "jet stability" with gravitationally "stable" jets occurring in the BP regime and jets becoming progressively more "unstable" as they occur in the PC and TC regimes. We focus our quantitative analysis on entrainment of ambient fluid into the jet column mixture, jet height fluctuations and sediment wave dynamics within this enhanced settling annulus. We also discuss qualitative observations of cloud and gravity current dynamics outside of the enhanced settling annulus and provide diagnostic links between jet regimes and distinct cloud structures and deposit architectures.

We organize our paper by introducing the experimental setup, scaling considerations and a 1D integral plume model for estimating jet properties above the source ("Methods") in the next section. We then discuss qualitative observations of jet collapse behavior in each regime focusing on the dynamics of sediment waves, gravity currents, cloud structure and resulting deposit architecture. Next, we analyze time series of sediment wave and jet properties quantitatively. We then discuss our constraints on volcanic jet stability and behavior across a new regime diagram that identifies BP-PC-TC regimes as a function of source parameters and median particle size. Finally, we revisit four well-known eruptions to verify our predictions for eruption dynamics and their expression in deposits ("Case studies: Implications for observations of explosive eruption columns and their deposits"): (1) Pinatubo, Philippines (1991), (2) Quilotoa, Ecuador (0.8 ka), (3) Calbuco, Chile (2015) and (4) Sumisu, Izu-Bonin Arc (30–60 ka).

Methods

Experimental Setup

Building on Carazzo and Jellinek (2012) and Jessop and Jellinek (2014) and Jessop et al. (2016), we carry out analogue experiments on axisymmetric particle-laden (multiphase) freshwater and saltwater jets (i.e. jets with buoyant and dense interstitial fluid, respectively) injected from below into a 1 m × 1 m × 1 m ambient layer of salt water with a linear density stratification (Fig. 5a and Table 1 Oster and Masahide 1963). In the majority of jet mixtures, the particle phase is approximately monodisperse "coarse" silica sand with a median diameter $d_{cp} = 225\ \mu$m, density of $\rho_{cp} = 2693$ kg/m^3 and a median terminal settling velocity in pure water $u_{s,cp} = 2.93 \times 10^{-2}$ m/s (see Table 1 in Jessop and Jellinek 2014). In a smaller suite of experiments the particle phase in the jet is composed of "fine" silica particles with a median diameter $d_{fp} = 100\ \mu$m, density of $\rho_{fp} = 2525$ kg/m^3 and a median terminal settling velocity in pure water $u_{s,fp} = 1.34 \times 10^{-2}$ m/s. In a few experiments we inject approximately bidisperse jets with particle phase drawn from these two populations. Our choice of particle size and density is motivated by scaling considerations we discuss in "Scaling natural volcanic jets to the laboratory setting".

Prior to the start of each experiment, a 10–20-L volume of jet mixture with prescribed physical properties is prepared and stirred vigorously in a delivery bucket that is perched above the top of the ambient fluid layer (Table 1 and Appendix A). We introduce fluorescein dye to this mixture to distinguish the interstitial fluid from the suspended particle phase (Fig. 5a). At the start of each experiment, a valve at the base of the delivery bucket is opened and the particle-fluid mixture (Table 1) is injected through a nozzle with a radius $r_0 = 3.2 \times 10^{-2}$ m (Fig. 5a). We vary the height of the delivery bucket to attain a range of jet mixture injection rates. Although the mean injection velocity declines approximately with the square root of the jet mixture layer height, this change is $<1\%$ for the duration of an experiment and, thus, the injection rate is approximately constant (Table 1 & 2). Experiments generally begin with a 5–10 second long "transient" period in which the injected mixture rises to a maximum height and descends back down to a LNB or to the tank base. After this initial period, jet column height oscillations become quasi stationary with an approximately constant mean and relatively much smaller fluctuation. We make measurements during subsequent statistically "steady-state" periods that persist for 35–60 s.

a) Front view experiment apparatus

b) Key experiment regions
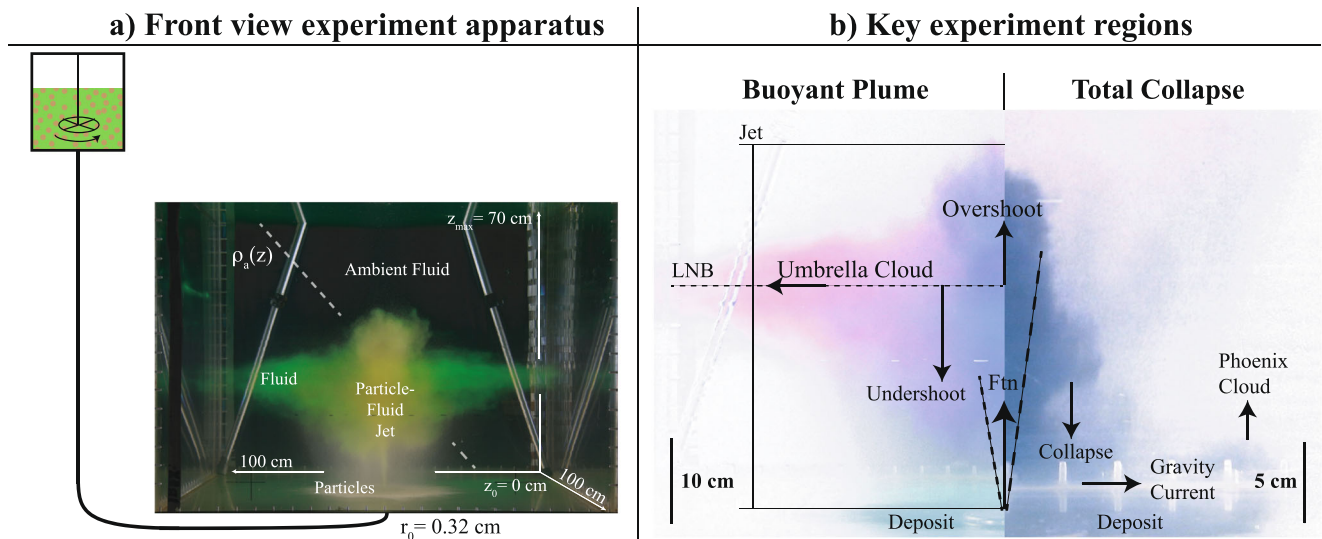
Fig. 5 (a) Front view of jet mixture delivery bucket with stirrer on the left and 3D water tank on right. Fluid dyed green, particles appear brown and particle-fluid mixture appears yellow. 3D tank dimensions marked with white lines and red line marks saltwater density decreasing with height. Tank is illuminated from the left and right side. (b) Color inverted images halfway through experiments with jets in the BP regime (left) and TC regime (right). Key regions of each regime are marked with white labels. Fountain region marked by "Ftn". Jet boundary in both regimes and Level of LNB in the BP regime are marked with dotted black lines

Visualizing and analyzing analogue jets

The tank is illuminated on two sides and time series of images are captured with as many as 3 DSLR cameras at a frame rate of 1–3 Hz (Fig. 5a). On the basis of the main qualitative features in these image data, it will be useful to define characteristic steady-state geometric properties of the experimental jets to which we will refer below. The "jet" is the inverted cone bounding the upward flowing mixture injected into the tank. In BP experiments (left side of Fig. 5b), relatively dense jets ascend above the LNB to form the "overshoot" region the height of which corresponds to where their momentum flux is exhausted. Relatively dense mixture collapses, in turn, from the overshoot region as a jet that crosses the LNB to penetrate the relatively dense layer beneath the LNB to form a corresponding "undershoot" region. (cf. Carazzo and Jellinek 2012). For coarse particle experiments, the undershoot height is identified in the experiments as the height where particle-fluid separation occurs. In addition to being readily identified visually, this penetration depth into the stratification beneath the LNB corresponds approximately to where the momentum flux carried by undershooting jets is exhausted. The height at which interstitial jet fluid spreads as a gravity current to form an umbrella cloud marks the LNB for the experiment. For experiments in the TC regime (right side of Fig. 5b), collapsing jet mixtures reach the tank base before particle-fluid separation occurs and spread as "gravity currents" along the tank base. As particles are deposited, buoyant interstitial fluid ascends to form "phoenix clouds" above the gravity current (Dobran and Neri 1993; Carazzo and

Jellinek 2012). In experiments where buoyant interstitial fluid escapes from collapsing mixtures before reaching the tank base, we refer to this escaping buoyant fluid as phoenix clouds. The height to which phoenix clouds rise and spread as "phoenix cloud layers" marks the characteristic LNB for TC experiments (see Fig. 11c, TC column in Fig. 12c and Section "Phoenix clouds"). This height marks the base of the overshoot region in the jet. For jets in the PC regime, all of the features in Fig. 11c can exist simultaneously. The sedimentation of particles form deposits at the tank base of varying architecture in all regimes and we will discuss characteristics for BP, PC and TC regimes, in detail.

Images of each experiment are post processed to highlight and measure various jet and particle settling dynamics. First, a background image is subtracted to highlight the jet, intruding fluid layers and particle deposit. Next, frames are color inverted so that particles appear blue and fluid appears pink on a white background (Fig. 6a). Individual particle settling is assumed to occur where coarse particles are observed by eye to settle through the ambient without carrying dyed fluid. Blue or blue-green colors on the tank base represent coarse particle deposition and the maximum extent of this region indicates the maximum distance coarse particles are transported from the jet axis by the umbrella cloud. At a given height, a sediment wave appears as an intermittent or periodic increase in the radius of the down-flow next to the jet. To highlight motion beside the jet edge, images are frame differenced, which allows sediment wave fronts to be tracked as sediment waves descend (Fig. 6b). The average jet radius, at the LNB height for BP and PC jets and at the average jet top heights for TC jets, as well

Table 1 Brunt-Väisälä frequency and source parameters for experiments in this study. $g'_{f,0}$ is the effective gravitational acceleration of the interstitial jet fluid. B_0 is the source buoyancy flux of the mixture

Exp #	N (s^{-1})	$g'_{f,0}$ $(m\ s^{-2})$	$\phi_{fp,0}$ $(-)$	$\phi_{cp,0}$ $(-)$	Q_0 $(m^3\ s)$	M_0 $(m^4\ s^{-2})$	B_0 $(m^4\ s^{-3})$
13	0.12	1.4×10^{-1}	2.2×10^{-2}	2.0×10^{-2}	3.0×10^{-5}	2.9×10^{-5}	-1.4×10^{-5}
14	0.11	2.3×10^{-2}	1.3×10^{-2}	1.2×10^{-2}	8.6×10^{-5}	2.3×10^{-4}	-3.0×10^{-5}
16	0.12	5.0×10^{-2}	1.2×10^{-2}	–	7.5×10^{-5}	1.8×10^{-4}	-8.6×10^{-6}
17	0.13	-8.9×10^{-2}	–	1.2×10^{-2}	3.1×10^{-5}	3.0×10^{-5}	-8.3×10^{-6}
18	0.13	6.6×10^{-2}	–	1.1×10^{-2}	9.1×10^{-5}	2.6×10^{-4}	-9.6×10^{-6}
19	0.13	5.2×10^{-2}	–	1.1×10^{-2}	8.7×10^{-5}	2.4×10^{-4}	-1.0×10^{-5}
20	0.12	-3.6×10^{-1}	1.9×10^{-2}	1.8×10^{-2}	1.0×10^{-4}	3.3×10^{-4}	-9.2×10^{-5}
23	0.12	-6.2×10^{-2}	–	1.3×10^{-2}	5.9×10^{-5}	1.1×10^{-4}	-1.6×10^{-5}
24	0.11	-8.1×10^{-2}	–	6.6×10^{-2}	5.6×10^{-5}	1.0×10^{-4}	-1.0×10^{-5}
26	0.10	-7.3×10^{-2}	–	1.5×10^{-2}	8.8×10^{-5}	2.5×10^{-4}	-2.7×10^{-5}
27	0.10	1.1×10^{-2}	–	2.8×10^{-2}	5.5×10^{-5}	9.5×10^{-5}	-2.4×10^{-5}
28	0.09	-2.0×10^{-1}	–	–	5.7×10^{-5}	1.0×10^{-4}	-1.1×10^{-5}
29	0.09	-2.3×10^{-1}	–	–	3.8×10^{-5}	4.6×10^{-5}	-8.8×10^{-6}
30	0.10	-1.7×10^{-1}	–	5.1×10^{-2}	5.4×10^{-5}	9.0×10^{-5}	-3.4×10^{-5}
32	0.00	-2.1×10^{-1}	–	4.9×10^{-2}	9.8×10^{-5}	3.0×10^{-4}	-1.0×10^{-5}
35	0.09	3.5×10^{-1}	–	3.3×10^{-2}	9.2×10^{-5}	2.6×10^{-4}	-1.5×10^{-5}
36	0.10	3.6×10^{-1}	–	3.3×10^{-2}	9.2×10^{-5}	2.6×10^{-4}	-1.4×10^{-5}
39	0.09	-4.1×10^{-1}	–	2.0×10^{-2}	8.7×10^{-5}	2.4×10^{-4}	-6.2×10^{-5}
42	0.10	3.8×10^{-2}	–	1.8×10^{-2}	5.9×10^{-5}	1.1×10^{-4}	-1.5×10^{-5}
43	0.10	2.4×10^{-1}	1.9×10^{-2}	2.4×10^{-2}	5.4×10^{-5}	9.3×10^{-5}	-2.3×10^{-5}
46	0.10	2.3×10^{-1}	–	2.9×10^{-2}	1.2×10^{-4}	2.8×10^{-4}	-2.1×10^{-5}
48	0.10	3.4×10^{-1}	–	3.1×10^{-2}	1.2×10^{-4}	4.8×10^{-4}	-1.9×10^{-5}
49	0.09	3.9×10^{-1}	3.8×10^{-2}	–	4.8×10^{-5}	7.2×10^{-5}	-7.8×10^{-6}
50	0.11	3.8×10^{-1}	5.4×10^{-2}	–	6.0×10^{-5}	1.1×10^{-4}	-2.4×10^{-5}
51	0.11	1.8×10^{-1}	–	2.5×10^{-2}	4.7×10^{-5}	6.9×10^{-5}	-9.4×10^{-6}
52	0.10	-4.2×10^{-2}	–	1.3×10^{-2}	8.1×10^{-5}	2.1×10^{-4}	-2.0×10^{-5}
54	0.11	2.4×10^{-1}	–	5.0×10^{-2}	9.9×10^{-5}	3.1×10^{-4}	-5.4×10^{-5}

as the average jet top height are measured using the color inverted images (see Section "Geometric constants for jet height scalings").

We measure the instantaneous height and radius of sediment waves at each instance in time in successive color-inverted and frame-differenced images to constrain the average sediment wave descent speed u_{SW}, distance between successive wave fronts (approximate wavelength) λ_{SW}, and maximum radius r_{SW}^{max}. We track these properties as sediment waves descend from their initial appearance in the overshoot region to the "sediment wave dispersal height" (cf. Bush et al. 2003) at which wave speeds are sufficiently small that particles settle from the mixture (BP and PC) or where imaging is occluded by gravity currents at the tank base (PC and TC). We define a characteristic frequency for sediment waves as the inverse of an advective time scale

$$f_{SW} = \frac{u_{SW}}{\lambda_{SW}}. \tag{2}$$

We will distinguish "large" and "small" sediment waves on the basis of their radial symmetry and apparent volume. Whereas relatively large-volume sediment waves are axisymmetric small-volume sediment waves typically have half the volume of large sediment waves and complex, non-axisymmetric shapes.

Spectral analysis of jet height oscillations

We will show that distinctive spectral properties (spectral slope and frequency properties) of steady-state jet height (see "Jet" label in Fig. 5b for instantaneous jet height measurement and "h_{avg}" label in Fig. 20 for average jet height) oscillations in BP, PC and TC regimes provide insight into the underlying multiphase dynamics governing the excitation of sediment waves in both the lower jet and overshoot fountain regions, as well as entrainment and mixing into the column. Accordingly, to characterize

Table 2 Dimensionless parameters and jet regime

Exp #	$-Ri_0$	ϕ_0	$St_{fp,0}$	$St_{cp,0}$	$\Sigma_{fp,0}$	$\Sigma_{cp,0}$	α_e	Regime
13	1.7×10^{-3}	4.2×10^{-2}	1.8×10^{-1}	1.4	6.7×10^{-3}	5.2×10^{-2}	–	PC
14	1.5×10^{-4}	2.5×10^{-2}	5.5×10^{-1}	4.0	2.3×10^{-3}	1.4×10^{-2}	1.31×10^{-1}	PC
16	6.6×10^{-5}	1.2×10^{-2}	4.8×10^{-1}	–	2.7×10^{-3}	–	8.5×10^{-2}	BP
17	9.2×10^{-4}	1.2×10^{-2}	–	1.4	–	3.8×10^{-2}	–	PC
18	4.1×10^{-5}	1.1×10^{-2}	–	4.3	–	1.3×10^{-2}	9.0×10^{-2}	BP
19	5.0×10^{-5}	1.1×10^{-2}	–	4.1	–	1.4×10^{-2}	–	BP
20	2.7×10^{-4}	3.7×10^{-2}	6.3×10^{-1}	4.6	–	1.1×10^{-2}	8.4×10^{-2}	PC
23	2.4×10^{-4}	1.3×10^{-2}	–	2.8	–	2.0×10^{-2}	8.0×10^{-2}	PC
24	1.8×10^{-4}	6.6×10^{-2}	–	2.6	–	2.1×10^{-2}	–	BP
26	1.2×10^{-4}	1.5×10^{-2}	–	4.1	–	1.3×10^{-2}	–	BP
27	4.5×10^{-4}	2.8×10^{-2}	–	2.6	–	2.2×10^{-2}	5.1×10^{-2}	TC
28	1.9×10^{-4}	–	–	–	–	–	7.4×10^{-2}	BP
29	5.0×10^{-4}	–	–	–	–	–	5.5×10^{-2}	TC
30	7.0×10^{-4}	5.1×10^{-2}	–	2.5	–	2.3×10^{-2}	5.2×10^{-2}	TC
32	3.4×10^{-4}	4.9×10^{-2}	–	4.7	–	1.2×10^{-2}	–	TC
35	6.3×10^{-5}	3.2×10^{-2}	–	4.5	–	1.4×10^{-2}	1.18×10^{-1}	PC
36	5.9×10^{-5}	3.2×10^{-2}	–	4.5	–	1.3×10^{-2}	1.08×10^{-1}	PC
39	3.0×10^{-4}	2.0×10^{-2}	–	3.9	–	1.2×10^{-2}	8.2×10^{-2}	PC
42	2.3×10^{-4}	1.8×10^{-2}	–	2.8	–	2.0×10^{-2}	7.7×10^{-2}	PC
43	4.6×10^{-4}	4.3×10^{-2}	3.6×10^{-1}	2.6	3.8×10^{-3}	2.3×10^{-2}	6.8×10^{-2}	TC
46	8.2×10^{-5}	2.9×10^{-2}	–	4.5	–	1.3×10^{-2}	7.8×10^{-2}	PC
48	3.2×10^{-5}	3.1×10^{-2}	–	6.0	–	1.0×10^{-2}	1.01×10^{-1}	BP
49	2.3×10^{-4}	3.8×10^{-2}	3.2×10^{-1}	–	4.3×10^{-3}	–	5.8×10^{-2}	PC
50	3.5×10^{-4}	5.4×10^{-2}	4.0×10^{-1}	–	3.4×10^{-3}	–	4.1×10^{-2}	PC
51	3.0×10^{-4}	2.5×10^{-2}	–	2.2	–	2.6×10^{-2}	6.6×10^{-2}	PC
52	1.2×10^{-4}	1.3×10^{-2}	–	3.8	–	1.5×10^{-2}	9.0×10^{-2}	BP
54	1.8×10^{-4}	5.0×10^{-2}	–	4.8	–	1.2×10^{-2}	8.7×10^{-2}	PC

and understand the periodic parts of this behavior we obtain spectral estimates from demeaned, detrended and tapered time series data using a standard Thompson multitaper algorithm (cf. Thomson 1982). We also construct representative power spectra for BP, PC and TC regimes by averaging the power spectra of all experiments within each regime.
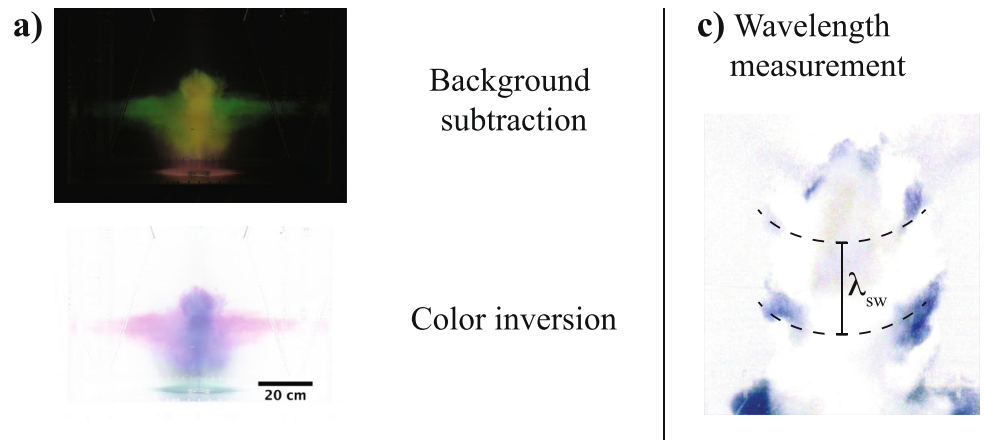
Scaling natural volcanic jets to the laboratory setting

Consistent with published studies, we present scaling considerations that use externally controlled source parameters and environmental and particle physical properties to define a set of dimensionless parameters that enable us to map laboratory analogues across a wide range of natural conditions (Morton et al. 1956; Woods 2010; Carazzo and Jellinek 2012). We focus our investigation on ranges of source parameters similar to Carazzo and Jellinek (2012, see Figures 3a & 3c in their study; Tables 1, 2 & 3), and Jessop et al. (2016), which overlap with the ranges expected for Plinian eruptions. In addition, we will introduce useful scales for jet height and jet height oscillation frequency that will enter into our characterizations of jet column gravitational stability and sedimentation regime and will provide insight into key underlying processes such as turbulent entrainment, related environmental conditions, and expected rise height (Morton et al. 1956; Turner 1966; Burgisser et al. 2005; Carazzo and Jellinek 2012).

It is important to note here the challenges of comparing scaled laboratory jets to volcanic jets. The eruption source parameters for volcanic jets are notoriously difficult to constrain. Although the source mass flux exiting a volcanic vent can be constrained, albeit with large uncertainties (Aubry et al., 2021), source mass flux alone is insufficient to capture the full dynamics governing eruption column

Fig. 6 Image post processing method. (a) A background image is subtracted from all images, which are then color inverted so that particles appear blue and fluid pink. (b) Images are frame-differenced to highlight motion between frames. Sediment waves (SW) marked by black arrows. (c) Sediment waves are identified in frame-differenced images and vertical wavelengths between them are measured
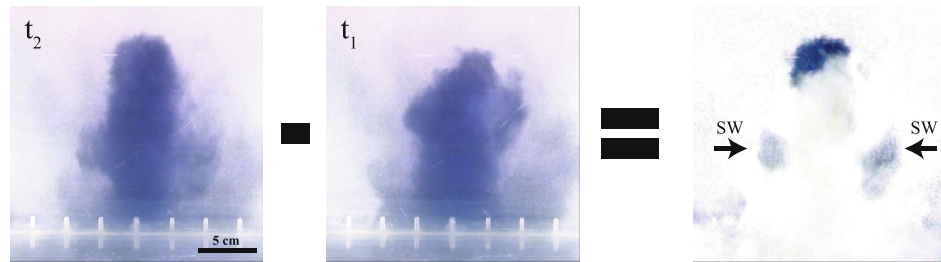
collapse (Kaminski and Jaupart 2001; Woods 2010; Michaud-Dubuy et al. 2018). In addition to source mass flux, independent estimates of vent diameter and exit velocity are required to capture volcanic jet strength (Eq. 5 in "Jet mixture properties and dynamics"; Woods 1995; Carazzo et al. 2008; Koyaguchi and Suzuki 2018) and, in turn, the tendency of volcanic jets to occur in the BP, PC or TC regimes. Yet, estimates of vent diameter and exit velocity are rare (Aubry et al. 2017b), and how these change during an eruption rarer still. For these reasons, the ranges of eruption source parameters are relatively large compared to the range investigated in this study. Even for well-studied eruptions, such as the 1980 eruption of Mt. St. Helens, uncertainties in vent diameter and exit velocity can lead to uncertainties in jet strength (Eq. 5) over two orders of magnitude (Carey and Haraldur 1985; Andrews and Gardner 2009; Jessop et al. 2016). Nonetheless, our experimental investigation provides a method to quantitatively constrain volcanic jet source parameters on the basis of observations of jet column regime, measurements of jet height oscillations and observations of deposit architecture, all of which are currently available for volcanic jets (Carey et al. 1990; Koyaguchi and Masami 1993; Holasek et al. 1996; Kaminski and Jaupart 2001; Rosi et al. 2001; Di Muro et al. 2008; Tani et al. 2008; Van Eaton et al. 2016; Pope et al. 2018; Hooft et al. 2019).

Jet mixture properties and dynamics

The volume fraction of the solid particle phase contributes to the bulk density of well-mixed multiphase jets (Jessop et al. 2016). Consequently the particle volume fraction ϕ, which can be constrained for both natural eruptions and specified in laboratory experiments, is typically one control parameter used to characterize their dynamics (Woods 2010; Carazzo and Jellinek 2012; Jessop et al. 2016). For quasi-steady vent source parameters, the likelihood that multiphase jets will rise in BP, PC or TC regimes depends on their turbulent entrainment and mixing properties. The self-similar rise of turbulent, axisymmetric, Boussinesq jets in the lab and in nature consequently depend on the volume, momentum and buoyancy fluxes carried by these flows (Morton et al. 1956; Woods 2010)

$$Q(z) \quad = \pi r(z)^2 u(z) \tag{3a}$$

$$M(z) \quad = \pi r(z)^2 u(z)^2 \tag{3b}$$

$$B(z) = \pi r(z)^2 u(z) g'(z). \tag{3c}$$

where $r(z)$ is the jet radius at any height. For steady jets, time-averaged values of these properties are conveniently specified at $z = 0$ and we will use the subscript '0' to indicate these "source parameters". Here, the effective gravitational acceleration for the particle-fluid mixture $g'(z) = g \Delta \rho(z)/\rho_a(z)$, with g the full gravitational

Table 3 Parameter ranges for experiments versus natural eruption. Re_0 is the source Reynolds number of the flows calculated at the tank nozzle for experiments and the volcanic vent for eruptions

Parameter [units]	Experiments	Natural eruptions
d_p [m]	$10^{-5} - 10^{-4}$	$10^{-6} - 10^{-2}$
f_{ftn} [s^{-1}]	$10^{-2} - 10^{-1}$	$10^{-4} - 1$
r_0 [m]	3.175×10^{-3}	$10 - 10^2$
u_0 [m/s]	$10^{-3} - 10^{-2}$	$10^{-1} - 10^2$
u_p [m/s]	$0.1 - 1$	$10^1 - 10^2$
H_{ftn} [m]	0.1	$10^3 - 10^4$
H_{pl} [m]	0.1	$10^3 - 10^4$
H_{OS} [m]	$10^{-2} - 10^{-1}$	$10^3 - 10^4$
N [s^{-1}]	10^{-1}	10^{-2}
μ [kg m^{-1} s^{-1}]	10^{-3}	10^{-5}
ρ_a [kg m^{-3}]	$998 - 1040$	$10^{-3} - 1$
ρ_f [kg m^{-3}]	$998 - 1050$	$0.1 - 1$
ρ_p [kg m^{-3}]	$2525 - 2693$	$750 - 2500$
ϕ_0	$10^{-3} - 10^{-2}$	$10^{-4} - 10^{-1}$
Re_0	$3000 - 12000$	$10^7 - 10^9$
Re_p	$1.3 - 6.5$	$10^{-4} - 10^6$
Ri_0	$10^{-5} - 10^{-3}$	$10^{-3} - 10$
St_0	$0.2 - 6.0$	$10^{-2} - 10^2$
Σ_0	$10^{-3} - 10^{-2}$	$10^{-3} - 1$

acceleration and $\Delta\rho(z) = (\rho_a(z) - \rho(z))$. The density difference at any height depends on the strength of the imposed stratification, which is given by the Brunt-Väisälä frequency, N

$$N = \sqrt{-\frac{g}{\rho_0}\frac{d\rho(z)}{dz}}. \qquad (4)$$

Before conducting an experiment, we measure $d\rho(z)/dz$ at 5-cm depth intervals in the ambient tank layer to ensure a linear density stratification over the depth of the water column.

The extent to which large overturning billows forming the edges of our analog jets can deform, entrain and mix ambient fluid depends on the vertical mean rise speed of the jet and on the stabilizing density differences across a characteristic eddy scale, L that depends on height. A well-established metric for this process is a local Richardson number

$$Ri(z) = \frac{g'(z)L(z)}{U(z)^2}, \qquad (5)$$

which through a ratio of restoring gravitational to driving turbulent accelerations indicates the mechanical work that can be extracted from the velocity field for entrainment and mixing (Linden 1979; Holford and Linden 1999; Kaminski et al. 2005; Jessop and Jellinek 2014; Lherm and Jellinek 2019). For a multiphase jet, $Ri(z)$ can be

calculated with the mean jet mixture buoyancy and velocity at a given height with the aid of a 1D integral model (Appendix B; Kaminski et al. 2005; Carazzo et al. 2008). The "source Richardson number" Ri_0 can be defined with Eq. 5 by taking the jet mixture buoyancy, velocity and radius at the source. Whereas $Ri(z)$ tracks local entrainment as a function of height in the jet, Ri_0 provides a useful global measure of jet strength at the source and the proclivity for buoyancy reversal and gravitational collapse, Fischer (1979), Woods (2010), Carazzo et al. (2008), and Carazzo and Jellinek (2012). Locally, where $|Ri(z)| < O(0.1)$ extensive turbulent entrainment and mixing is expected and approximations including the entrainment hypothesis discussed above are justified (Turner 1986). In addition, buoyancy-driven (plume) dynamics dominate where $Ri_0 > 0$, and momentum-driven (fountain) dynamics where $Ri_0 < 0$.

The mean rise height and its fluctuation will provide important additional diagnostics for the mixture dynamics that give rise to BP, PC and TC behavior. The rise height of a jet injected vertically into a stratified environment is readily predicted on dimensional grounds (Morton et al. 1956; Turner 1986; Linden 2000; Woods 2010). For buoyant plumes ($B_0 > 0$)

$$H_{pl} = C_{pl} \times \alpha^{-1/2}|B_0|^{1/4}N^{-3/4}, \qquad (6)$$

where from laboratory measurements for particle-free flows (Turner 1986) $C_{pl} \approx 2.8$ for the maximum height of rise and from measurments and numerical calculations $C_{pl} \approx 2.1$ for the LNB height. We test the accuracy of Eq. 6 using $C_{pl} = 2.8$ for predicting maximum jet rise heights by comparing these predicted heights with measured maximum rise heights of our multiphase jets in the BP and PC regimes ("Geometric constants for jet height scalings").

For momentum-driven fountains, $B_0 < 0$ and $M_0 > 0$ and the rise height (Morton 1959; Turner 1966; Bloomfield and Kerr 1998)

$$H_{ftn} = C_{ftn}(\sigma)M_0^{3/4}|B_0|^{-1/2}, \qquad (7)$$

where $C_{ftn} \approx 1.9$ is again for particle-free flows and

$$\sigma = \frac{M_0^2 N^2}{|B_0|^2} \qquad (8)$$

is a measure of the initial buoyancy force acting on the mixture at the source and the buoyancy force acting on the mixture as it rises through the ambient stratification. Bloomfield and Kerr (1999) find

$$C_{ftn}(\sigma) = (1.9^{-4} + 3.0^{-4}\sigma)^{-1/4} \qquad (9)$$

works well for all values of σ. In the limit $\sigma \to \infty$ jet height is controlled by M_0 and N, whereas for $\sigma \to 0$ jet height is controlled by M_0 and B_0, recovering the common fountain rise height scaling for particle-free flows. We test

the accuracy of Eq. 7, using constant values for C_{ftn} and values that depend on source parameters (Eqs. 8 and 9), for predicting maximum jet rise heights and comparing these with measured maximum rise heights of our multiphase jets in the BP, PC and TC regimes ("Geometric constants for jet height scalings").

Where jets rise as fountains with $B < 0$ at their maximum heights ($B(H_{ftn,max}) < 0$), oscillations driven by the intermittent buildup and downward collapse of volumes of relatively dense fluid occur with a frequency set by the ratio of the jet source buoyancy and momentum fluxes (Burridge and Hunt 2013)

$$f_{ftn} = F_{ftn} \frac{|B_0|}{M_0} \tag{10}$$

where $F_{ftn} \approx 0.7$ (see Figure 11 in their study). However, if ambient fluid entrainment causes a buoyancy reversal with $B(H_{ftn,max}) > 0$ & $B(H_{pl,max}) < 0$ such that the mixture overshoots the LNB to form an "overshoot fountain" (Fig. 4; Turner 1966; Baines et al. 1990), the mean rise height of this "upper fountain" will be set by

$$H_{OS} = C_{ftn}(\sigma) M_{LNB}^{3/4} |B_{LNB}|^{-1/2}, \tag{11}$$

and will oscillate about this mean height with a frequency

$$f_{OS} = \frac{1}{2} \frac{|B_{LNB}|}{M_{LNB}}. \tag{12}$$

Here, B_{LNB} and M_{LNB} are the buoyancy and momentum fluxes of the jet mixture at the observed LNB of the interstitial jet fluid (see Appendix B) and can be used to find σ for Eqs. 8 & 9.

Particle-fluid stress coupling

Recent studies highlight that particle inertial effects can have a strong influence on the structure of eddies forming jet edges and, thus, on the entrainment parameter in Eq. 1 (Jessop and Jellinek 2014; Cerminara et al. 2016). Consequently, the behavior of jets is incompletely characterized in a $-Ri_0 \leftrightarrow \phi_0$ parameter space contructed on the basis of average jet mixture properties. In addition, particle gathering within turbulent billows (Balachandar and Eaton 2010; Crowe et al. 2011) and particle loss through various sedimentation mechanisms can modulate inertial effects and also give rise to local buoyancy effects within multiphase jets that remain poorly understood. Nevertheless, to account for particle-scale inertial and buoyancy effects we introduce two additional dimensionless parameters.

Depending on the particle volume fraction ϕ, the extent to which particle inertial effects modulate jet behavior is captured by the Stokes number St formed by the ratio of the particle response time τ_p to the characteristic fluid flow time τ_f Elghobashi (1994) and Burgisser et al. (2005)

$$St = \frac{\tau_p}{\tau_f} = \frac{\rho_p d_p^2}{18 f_p \mu_f} \frac{U}{L}, \tag{13}$$

where μ_f is the dynamic viscosity of the fluid phase and f_p is a drag factor that is a function of the particle Reynolds number Re_p for the conditions in our experiments (see Eqs. 20 and 21 in Appendix A; Burgisser et al. 2005). We define St_0 at the source with $\mu_f = \mu_{f,0}$, $U = u_0$ and assuming the scaling $L \sim r_0$. With this choice of scales at the source, St_0 describes the coupling of particles to the largest eddies developing just above the source in the jet. Where St $\gg 1$ particles are "decoupled" from the flow and they follow ballistic trajectories that can enhance turbulent mixing. By contrast, where St $\ll 1$ particles are "fully coupled" to the flow and inhibit turbulent momentum and energy exchange as well as entrainment and mixing (Mallouppas et al. 2017; Lherm and Jellinek 2019). In natural volcanic jets, ash- and lapilli-sized fragments with St $\sim 0.1 - 1$ comprise the major volume of erupted material and are the predominant component in dilute suspensions forming jet edges. Recent work suggests that whereas lapilli-size particles carried by entraining eddies forming jet edges can contribute angular momentum that increases entrainment, causing α to rise, entrained ash can be highly dissipative, causing α to decline from particle-free values (Lherm and Jellinek 2019). Accordingly, our experiments will use mono- and bi-disperse suspensions of "coarse particles" ($1.2 \leq St_0 \leq 4.9$; Table 1) and "fine particles" ($0.2 \leq St_0 \leq 1.4$; Table 1) and we will refer to these jets as "coarse particle jets" and "fine particle jets".

Whether significant particle inertial effects occur depends partly on the residence times of dense particles compared to the turnover times of eddies in which they are entrained. The significance of particle loss by various sedimentation mechanisms depends on the Sedimentation number (Burgisser et al. 2005; Carazzo and Jellinek 2012)

$$\Sigma = \frac{\tau_f}{\tau_s}, \tag{14}$$

where $\tau_s = U_s/L$ is the particle settling time with U_s the particle terminal settling velocity. Particles settle out of the flow where $\Sigma \gg 1$, remain in suspension where $\Sigma \ll 1$ and can create local regions of high ϕ where $\Sigma \sim 1$. We define Σ_0 at the source with $L = r_0$ and $U = u_0$ (Table 1). To characterize the extent to which particle loss contributes to
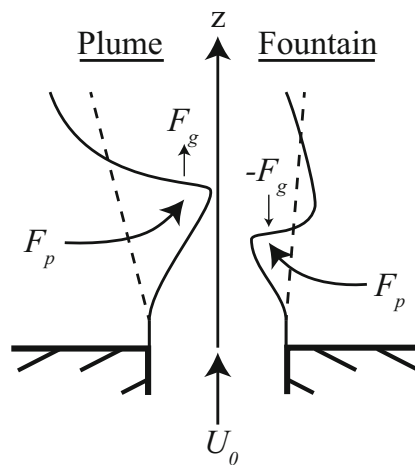
Fig. 7 Effect of fluid buoyancy on entrainment into a buoyant plume (**left**) and a fountain (**right**). Solid lines indicate instantaneous boundary and dashed lines mark time-averaged boundaries. **Left:** the force resulting from the dynamic pressure of the jet flow, F_p, drives entrainment of ambient fluid and is enhanced by the positive buoyancy force, F_g, acting on the interstitial plume fluid. **Right:** entrainment of ambient fluid driven by F_p is inhibited by the negative buoyancy force acting on the interstitial plume fluid

the dispersal of sediment waves within the ambient layer, or their descent to, and spread at the floor, in addition to Σ it will also be useful to introduce an internally determined sediment wave Strouhal number

$$\text{Str} = \frac{f_{sw}}{N}. \tag{15}$$

Where $\text{Str}_{SW} > 1$, sediment wave mixtures descend to the tank base before dispersing whereas for $\text{Str}_{SW} \leq 1$ sediment waves may disperse above the tank base.

Interstitial fluid buoyancy

The local buoyancy of a fluid jet depends on the sign of the effective gravitational acceleration $g'_f(z) = g(\rho_a(z) - \rho_f(z))/\rho_a(z)$ and influences the efficiency of entrainment (Kaminski et al. 2005; Carazzo et al. 2008). Entrainment into fountains is generally less than into plumes (Turner 1979; Kaminski et al. 2005; Carazzo et al. 2008). Fig. 7 shows the force resulting from the dynamic pressure gradient across the jet boundary, which drives entrainment of ambient fluid into plumes and fountains. Generally, where jet fluid is buoyant, resulting vertical accelerations enhance entrainment and plume rise. By contrast, where jet fluid is relatively dense, retarding buoyancy forces inhibit entrainment into fountains and modulate fountain rise.

However, for jets that are concentrated mixtures including dense $0.1 < \text{St} < 1$ and $\Sigma \leq 1$ particles and buoyant interstitial fluid, because of the complex local dynamics related to particle gathering (Jessop and Jellinek 2014; Lherm and Jellinek 2019) and sedimentation it is unclear whether the average negative buoyancy of the mixture or the positive buoyancy of the interstitial fluid governs the efficiency of entrainment of ambient fluid.

The buoyancy of the interstitial gas in natural eruption columns can increase significantly through the transfer of heat from erupted $\epsilon_0 < 1$ ash- and lapilli-sized particles to entrained cold atmosphere Woods and Wohletz (1991, 1995). Thermal equilibration occurs over a time scale d_p^2/κ and is generally much smaller than the time scale for jets to exhaust their initial momentum flux u_0/g'_0 (Valentine and Gregg 2008; Woodhouse et al. 2013). Thus, depending on the particle loading, through this process initially dense particle-fluid mixtures can evolve to be buoyant plumes through a well-known buoyancy reversal, a process that has been explored in isothermal laboratory experiments (Woods and Caulfield 1992; Kaminski et al. 2005; Carazzo and Jellinek 2012). Additional unexplored complications to this well-studied process can arise in multiphase jets where the thermal response times of entrained particles is similar to their inertial responses times. How this coupling affects the process of buoyancy reversal or the extent and likelihood that interstitial fluid will rise and detrain from the mixture is unclear and beyond the scope of this work.

Although thermal buoyancy generation plays a key role in determining whether an erupted mixture undergoes a partial or complete buoyancy reversal (cf. BP versus late collapse in Carazzo and Jellinek 2012), this effect is secondary to the contribution of the particle volume fraction to the mixture bulk density and the initial momentum flux driving the development and efficiency of entrainment below the momentum exhaustion height Woods (1988, 1995, 2010, 2012). Our isothermal experiments consequently address the source parameters and specifically the novel multiphase flow dynamics that govern entrainment and column collapse. Our experiments simulate, in part, the net effect of thermal buoyancy generation by using interstitial fluid that is buoyant at the source in several of our experiments. Our Boussinesq experiments do not capture more complex effects related to mixture compressibility on the flow dynamics above the source (Valentine and Wohletz 1989; Cerminara et al. 2016; Koyaguchi and Suzuki 2018), to latent heat release from water vapor condensation, which is unclear (Glaze et al. 1997; Aubry and Jellinek 2018), nor the effects of wind stress on entrainment (Aubry et al. 2017b).

Notation	Definition	Units	Subscripts	
cm	centimeters	cm	0	values at the source of the jet
d	diameter	m	∞	infinity
f	frequency	s^1	a	values for ambient fluid
g	gravitational acceleration of Earth	$m\ s^1$	BV	values for Brunt-Väisälä frequency
g'	effective gravity	$m\ s^2$	cp	values for coarse particles
h	measured height	m	dep	values for deposits
ka	thousands of years ago	yr	e	values for entrainment
km	kilometers	km	f	value for fluid
kg	kilograms	kg	fp	values for fine particles
m	meters	m	ftn	values for fountains
min	minutes	min	j	values for jets
mm	millimeters	mm	LNB	values at level of neutral buoyancy
μm	micrometers	μm	$LrgSW$	values for large sediment waves
r	radius	m	max	maximum values
s	seconds	s	min	minimum values
t	time	s	p	values for particles
u	bulk velocity	$m\ s^{-1}$	Phx	values for phoenix clouds
z	height	m	pl	values for plumes
B	buoyancy flux	$m^4\ s^{-3}$	s	values for settling particles
C	height constant	–	OS	values for overshoot region
F	frequency constant	–	SW	values for sediment waves
H	hertz	s^{-1}	$SmlSW$	values for small sediment waves
H	characteristic height	m	w	values for water
L	litres	L		
L	characteristic length scale	m		
LNB	Level of Neutral Buoyancy	m		
M	momentum flux	$m^4\ s^{-2}$		
ma	millions of years ago	yr		
N	Brunt-Väisälä frequency	s^{-1}		
P	spectral power	–		
Q	volume flux	$m^3\ s^{-1}$		
Ri	Richardson number	–		
St	Stokes number	–		
Str	Strouhal number	–		
U	characteristic velocity	$m\ s^{-1}$		
Ұ	volume	m^{-3}		
α	entrainment parameter	–		
λ	wavelength	m		
μ	dynamic viscosity	$kg\ m^{-1}\ s^{-1}$		
ν	kinematic viscosity	$m^{-2}\ s^{-1}$		
ϕ	particle volume fraction	–		
ρ	bulk density	$kg\ m^{-3}$		
σ	fountain scaling parameter	–		
τ	characteristic time	s		
ζ	Collapse number	–		
Λ	Jet Stability number	–		
Σ	Sedimentation number	–		
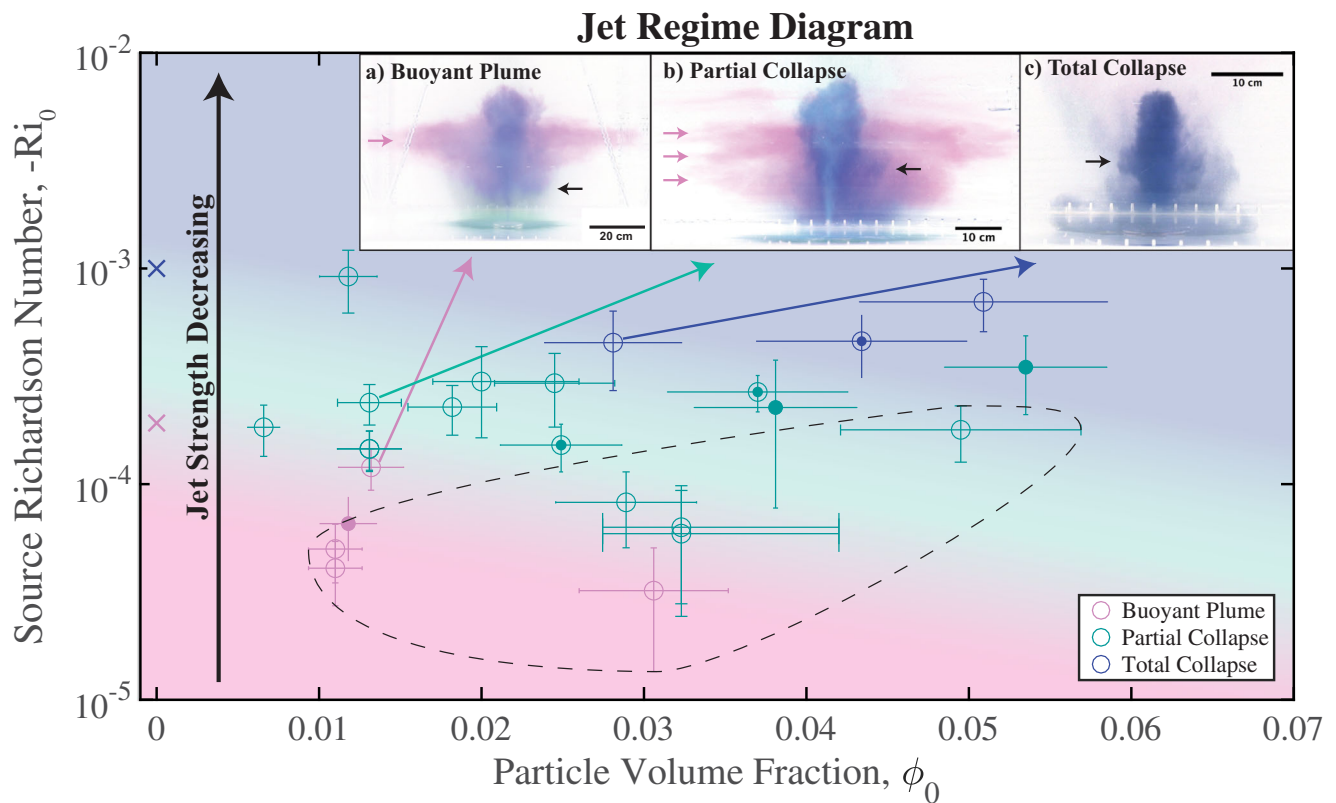
Fig. 8 Regime diagram showing the $-Ri_0 \leftrightarrow \phi_0$ parameter space for our experiments (Eq. 5; Table 2). Jets in the BP, PC and TC regimes with coarse particles are represented by pink, green and blue circles, respectively. Dots mark jets with mixtures of fine particles and circles with an inner dot mark jets with fine and coarse particles. Particle-free jets marked with an X. Gradient of background color shows qualitatively the continuum of jet behavior between the BP and TC end-member regimes that defines the transitional PC regime. Dotted line encircles jets with buoyant interstitial fluid. **(Insets)** Pink, green and blue arrows point to color inverted images of experiment represented by the data point they extend from. (a) Color inverted image of a jet in the BP regime. Pink and blue colors indicate jet fluid and coarse particles. (b) Image showing a jet in the PC regime with a multiply layered cloud. (c) Image showing a jet in the TC regime with phoenix clouds beginning to ascend from ground-hugging gravity currents. Black arrows point to discrete collapses of jet mixture falling around the jets and pink arrows point to spreading cloud layers

Qualitative observations: sediment waves, cloud intrusions and deposit architecture among regimes

We first characterize the main controls on the dynamics of jet stability, cloud structure and particle sedimentation in a broad $-Ri_0 - \phi_0$ parameter space. The majority of our experiments are either on monodisperse coarse particle jets ($1.2 \leq St_0 \leq 4.9$ & $10^{-2} \leq \Sigma_0 < 10^{-1}$; Table 2) or fine particle jets ($0.2 \leq St_0 \leq 1.4$ & $10^{-3} \leq \Sigma_0 < 10^{-2}$). To understand aspects of the sensitivity of our results to particle size distribution, which will be complex in natural volcanic jets, we carry out an additional small number of experiments on jets with prescribed mixtures of coarse and fine particles. Our aim here is to identify and describe key underlying processes acting within the jet, at the jet edge, within the overshoot region and at the tank base. From these data we summarize the principal observations of coupled jet dynamics and particle settling processes, that govern processes including entrainment of ambient fluid and time-dependent changes in jet top height, as well as expressions of these dynamics in deposit architectures. We analyze these processes quantitatively in "Quantitative results: links between source parameters and sediment wave dynamics".

Ri_0-ϕ_0 regime diagram: overall classification

Strong jets in the BP regime injected under low $-Ri_0$ conditions ($-Ri_0 < 2.2 \times 10^{-4}$) and with $\phi_0 < 3.5 \times 10^{-2}$ produce well-known umbrella clouds with a distinctive overshoot region, consistent with previous studies (BP experiments in Table 2; Fig. 8a; Sparks 1986; Woods 2010; Carazzo and Jellinek 2012). In this end-member regime, descending fluid from the overshoot region spreads to form an umbrella cloud that oscillates across the LNB into and out of the undershoot region (Figs. 5 & 9). By contrast, weak jets with $-Ri_0 > 2.7 \times 10^{-4}$ and $\phi_0 > 2.4 \times 10^{-2}$ in the TC regime produce collapsing fountains (TC experiments

in Table 2; Fig. 8c; Carey et al. 1988). In this end-member regime, the collapsing particle-fluid mixture spreads as intermittent gravity currents along the tank base. Entrained buoyant interstitial fluid ascends from the gravity currents as phoenix clouds (Carazzo and Jellinek 2012), which spread into a single "phoenix cloud layer" below the maximum height of the jet.

An extensive transitional PC regime fills the space between the BP and TC end-member regimes with $2.4 \times 10^{-5} < -\mathrm{Ri}_0 < 1.2 \times 10^{-3}$ and $6.0 \times 10^{-3} < \phi_0 < 5.7 \times 10^{-2}$ (PC experiments in Table 2; Fig. 8b; Neri and Dobran 1994; Di Muro et al. 2004; Di Muro et al. 2008). In this regime, depending on the proximity of $-\mathrm{Ri}_0 \leftrightarrow \phi_0$ conditions to the BP or TC regimes, a variable fraction (10−90%) of the injected mixture volume is visually observed to form an umbrella cloud. Simultaneously, any remaining injected volume collapses and spreads as particle-laden gravity currents along the tank base. Ascending phoenix clouds of buoyant interstitial fluid rise from from spreading gravity currents rise to form phoenix cloud layers below the umbrella cloud (Supplemental Video 3). In general, as $-\mathrm{Ri}_0$ and ϕ_0 are increased across this regime, more of the injected mixture collapses and spreads as gravity currents (Fig. 12b).

Two fine particle jet experiments with $7.7 \times 10^{-5} < -\mathrm{Ri}_0 < 4.9 \times 10^{-4}$ and $3.7 \times 10^{-2} < \phi_0 < 5.6 \times 10^{-2}$ begin in typical BP regimes but evolve in a way that is distinct from the coarse particle jet experiments (# 49 and 50 in Table 2; Fig. 8). Although the mixture descending from the overshoot region spreads at the LNB in the usual way, oscillations of the umbrella cloud centerline into the undershoot region next to the jet are relatively large (see Supplemental Video 1). Late in the experiment, jet mixture descends into the undershoot region and down along the jet edge to the tank base. This behavior is described as "late collapse" in Carazzo and Jellinek (2012) and we classify these jets into the more general PC regime. This late collapse property is not a general feature of BP jets: Another experimental jet with only fine particles occurs in the BP regime ($-\mathrm{Ri}_0 = 6.6 \times 10^{-5}$ and $\phi_0 < 1.2 \times 10^{-2}$).

Three experimental jets (#14, 20 and 43 in Table 2 and circle markers filled with a dot in Fig. 8) were laden with fine and coarse particles (bi-disperse). During the first 5 seconds of experiment #43, with $-\mathrm{Ri}_0 = 4.6 \times 10^{-4}$ and $\phi_0 = 4.3 \times 10^{-2}$, the entire injected mixture collapses and spreads out axisymmetrically as gravity currents along the tank base (Fig. 13a and Supplemental Video 2). Rising mixtures of fluid and fine particles obscure the view of the jet column for the remainder of the experiment. We classify this jet in the TC regime on the basis of the initial total collapse observation of the jet column (blue circle filled with dot in Fig. 8). During experiments 14 and 20, with $1.1 \times 10^{-4} < -\mathrm{Ri}_0 < 3.2 \times 10^{-4}$ and $2.1 \times 10^{-2} < \phi_0 <$
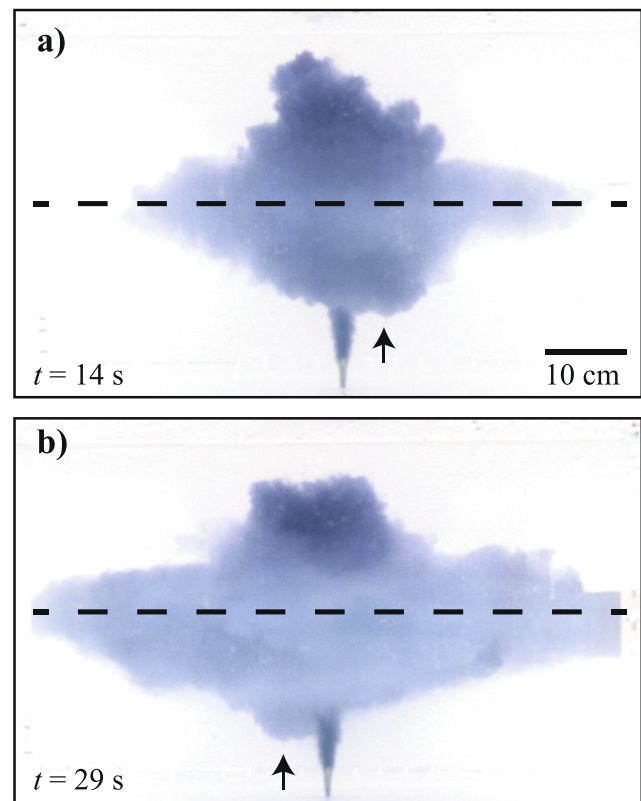
Fig. 9 Color inverted images of experiment #16 with fine particles occurring in the BP regime at two different instances. Black arrows point to mixtures spreading into the umbrella cloud while oscillating into the undershoot region next to the jet edge

4.3×10^{-2}, injected mixture spreads simultaneously into an umbrella cloud and gravity currents along the tank base. Therefore, we classify these jets in the PC regime (green circles filled with dot in Fig. 8).

Two particle-free experiments are conducted with $2.1 \times 10^{-4} < -\mathrm{Ri}_0 < 5 \times 10^{-4}$ (Table 2; Fig. 8). In experiment 28, all of the jet fluid spreads to form an umbrella cloud and we classify this jet in the BP regime. In experiment 29, the majority of the jet fluid collapses to the tank base before rising and spreading into phoenix cloud layers. Therefore, we classify this jet in the TC regime (Fig. 8).

Periodic sediment waves and the delivery of material to umbrella clouds and gravity currents

In all coarse particle jets we observe particle-rich "sediment waves" (that are "large" or "small" and we define these classifications below) falling periodically from the LNB and overshoot regions (see arrows in Fig. 8a–c and blue features in Figs. 11 and 12a and in Supplemental Videos 3 & 4). The formation and descent of both classes of sediment wave excite distinctive oscillations at the tops of the jet columns to which we will return in "Spectral analysis of jet height

Front View   **Top View**
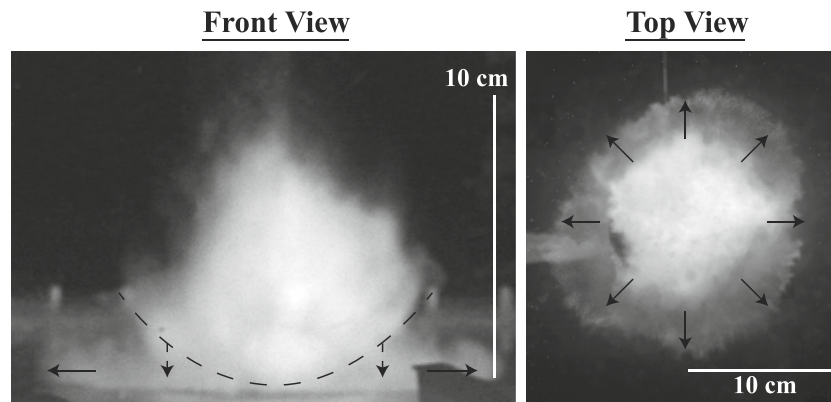
Fig. 10 Front and top views of a ground-hugging gravity current spreading axisymmetrically from the base of a jet in the TC regime while an annular sediment wave descends around the jet. Solid and dotted black arrows show flow direction of ground-hugging gravity current and descending sediment wave, respectively. Although this jet was injected through an annular nozzle, this large annular sediment wave is representative of those observed to descend around TC jets injected through cylindrical nozzles. In bottom right of front view, tape on the front of the tank partially obscures view of ground-hugging gravity current front

oscillations". In general, approximately annular, "large" sediment waves descend from the jet overshoot regions of coarse particle jets in the PC and TC regimes (black arrows in Fig. 8b-c and marked "Lrg SW" in Fig. 11b–c). Relatively low frequency and large amplitude oscillations in jet height are observed to be concurrent with large sediment waves descending from the jet top (see Fig. 20 in "Jet source parameters, sediment wave velocity and sediment wave longevity"). These axisymmetric flows sink to the tank base, where they spread as particle-driven gravity currents. Sedimentation from these flows releases trapped buoyant interstitial fluid, which rises as Phoenix clouds to form layers beneath the LNB.

In addition to these impressive features, quasi-periodic lower volume "small" sediment waves (black arrow in Fig. 8a and marked "Sml SW" in Fig. 11) descend from the LNB and overshoot regions of coarse particle jets in all three regimes and, compared to large sediment waves, excite relatively higher frequency and lower amplitude jet height oscillations, in turn. In contrast to large sediment waves, these features are generally asymmetric and descend down one side of the jet to the tank base, where they spread as gravity currents. A defining characteristic of descending small sediment waves is that they descend sufficiently slowly that coarse particles can decouple from the flow before reaching the tank base, where they settle individually, causing the waves to disperse (Figs. 8a and 11a). For jets in the BP regime, the lowest height at which sediment waves disperse marks a boundary below which individual particle settling is the only mechanism by which particles are carried to the tank base (Figs. 8a and 11a).

Coarse particle jets in the BP and TC regimes are also distinguished on the basis of where the majority of the erupted buoyancy flux is delivered. In the BP regime the majority of the injected mixture is delivered into a spreading

umbrella cloud whereas only a very small fraction of the injected volume is partitioned into predominantly small sediment waves that disperse entirely before reaching the tank base (Figs. 8a and 12a).

In the TC regime, by contrast, > 90% of the injected mixture volume collapses to the tank base via predominantly large sediment waves (Fig. 8c; blue features around jet in TC regime in Fig. 12a). Figure 11c shows a sequence of images tracking a large sediment wave that descends next to the jet edge. The sediment wave deposits a large fraction of its sediment load on reaching the tank base and then continues to flow radially outward as a gravity current until the remaining sediment load is deposited. Subsequent sediment waves periodically generate axisymmetric gravity currents. Small sediment waves are observed to fall in between large sediment waves (Fig. 11c).

A key characteristic of jets in the intermediate PC regime is that the injected mixture is simultaneously and variably partitioned into the spreading umbrella cloud and sediment waves descending next to the jet edge, depending on $-Ri_0$ and ϕ_0 (Figs. 8 and 11b; Supplemental Video 3). For a constant ϕ_0, as $-Ri_0$ increases, a greater fraction of sediment load is removed by increasingly large sediment waves (Fig. 12a). A unique feature of both large and small sediment waves in the PC regime is that they can undergo "partial dispersal" where parts of descending sediment waves farthest from the jet edge can spread into phoenix cloud layers before reaching the tank base (shown by pink arrows for sediment waves marked 1 & 2 in Fig. 11b) while the parts of sediment waves closer to the jet edge reach the tank base to spread into gravity currents (shown by blue arrows for sediment waves marked 1 & 2 in Fig. 11b). The partial dispersal of a single sediment wave can generate spreading phoenix cloud layers at intermittent heights underlain by gravity currents spreading along the
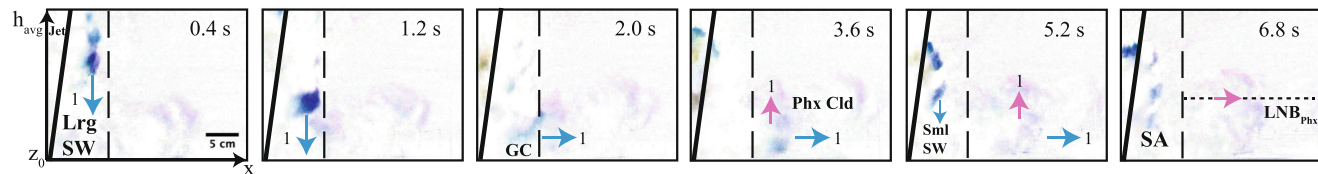
Sediment Wave to Phoenix Cloud Sequence

a) Buoyant Plume Regime
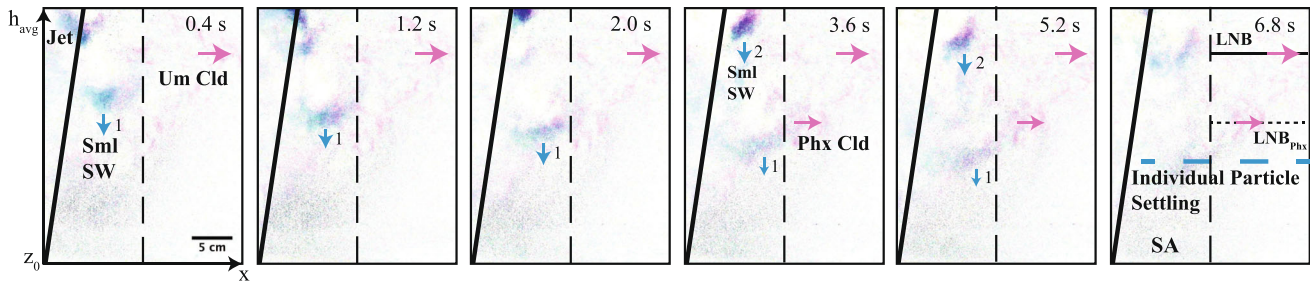
b) Partial Collapse Regime
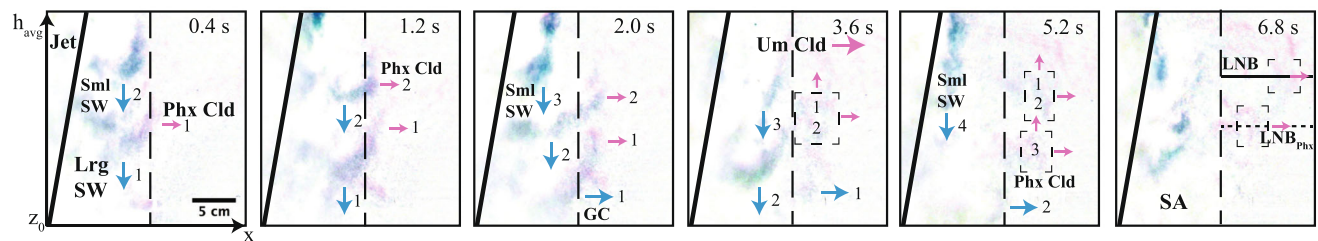
c) Total Collapse Regime

Fig. 11 Color inverted and frame-differenced images showing temporal evolution of sediment waves (SW) and phoenix clouds (Ph) in each regime. Sediment waves, as well as the gravity currents and phoenix clouds they produce, are numbered to track them through the sequence of images. Blue arrows indicate paths of sediment waves and subsequent gravity currents (GC). Large and small pink arrows indicate the paths of the spreading umbrella clouds (Um) and phoenix clouds. In the last column the horizontal black line marks the LNB at which the umbrella cloud spreads and the horizontal dashed line marks the LNB at which phoenix clouds spread (LNB$_{Phx}$). Vertical dashed lines mark the outer radius of the enhanced settling annulus (SA, see "Periodic sediment waves, the "enhanced settling annulus" and deposit architecture"). (a) Large sediment wave leading to individual particle settling and a phoenix cloud for jet in the BP regime. The horizontal dashed line marks the height at which the particle settling regime changes to individual particle settling. (b) Sediment wave leading to a gravity current and two phoenix clouds for a jet in the PC regime. Dashed boxes track phoenix cloud fronts that originate from marked sediment wave. Note the interactions between phoenix clouds from separate sediment waves. (c) Sediment wave leading to a gravity current and phoenix cloud for a jet in the TC regime

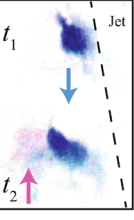tank base. Similar to the TC regime, small sediment waves fall between large sediment waves.
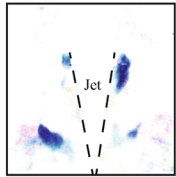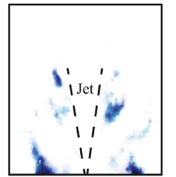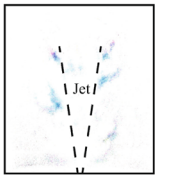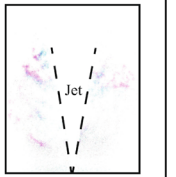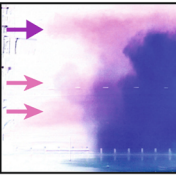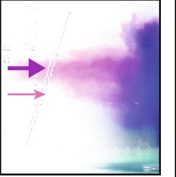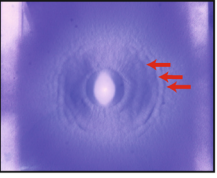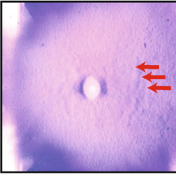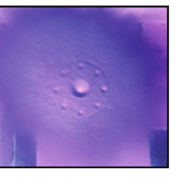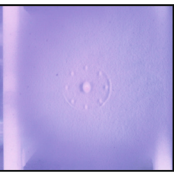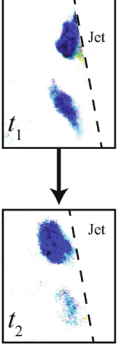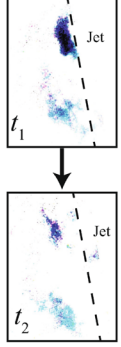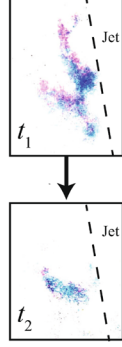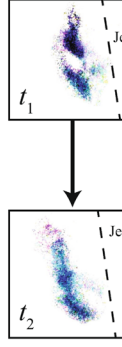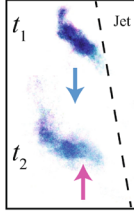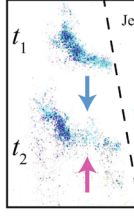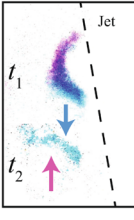
Finally, although the majority of our experiments are on coarse particle jets, we find that fine particle jets in the same $-Ri_0 \leftrightarrow \phi$ parameter space show additional behaviors not evident in coarse particle jet experiments. In particular, quasi-periodic partial collapses of the mixture on alternate sides of the jet excite additional oscillations at the top of the jet column and feed non-axisymmetric gravity currents including the late collapse discussed above (cf. Carazzo and Jellinek 2012). Detailed visual observations of these flows are, however, challenging because the jet column and jet mixture collapsing from the overshoot region is occluded by the particle-rich spreading umbrella cloud and individually settling particles below it. We return to the effects of these

processes on jet top height oscillations in "Spectral analysis of jet height oscillations".

Phoenix clouds

In all three regimes, buoyant interstitial jet fluid is carried below its LNB by descending sediment waves and, thereafter, rises as "phoenix clouds" (Fig. 11; cf. Dobran and Neri 1993; Carazzo and Jellinek 2012). Phoenix clouds spread to form internal cloud layers where the LNB of the buoyant interstitial fluid is between the jet top height (TC regime) or umbrella cloud LNB (BP regime) and the tank base. In general, phoenix clouds originate from two sources: (1) through the dispersal of particularly small sediment waves above the tank base in BP and PC regimes and (2) as a result of

Continuum of Observed Behaviour Across Regimes

Fig. 12 Table presenting the difference in jet processes for each jet regime. Each row represents a feature and each column has a representative image from each regime. (a) Color inverted and frame-differenced mages with the jet subtracted to highlight sediment waves. Sediment wave size and velocity are described below each image among jet regimes. (b) Color inverted images of spreading clouds from each regime. Pink and purple arrows indicate phoenix cloud and umbrella cloud layers respectively. (c) Color inverted images of resultant deposits formed in each regime. Concentric ring features are marked with red arrows. Description of deposit shape and presence of rings provided below each image. Six small circles around the nozzle in right two images are depressions in the deposit above the nozzle bolt holes. (d) Color inverted, frame-differenced and zoomed images focusing on pairs of sediment waves. First image (t_1) shows sediment wave pair at a high position next to the jet and the second image (t_2) shows same pair at a lower position. Numbers at top left of each box describe frequency of interactions. (e) Stack of two color inverted, frame-differenced and zoomed images showing individual sediment waves at two distinct times (t_1: top blue feature; t_2: bottom blue feature) with a blue arrow indicating motion. A pink arrow indicates motion of a phoenix cloud from a previous sediment wave. Numbers indicate importance of interactions for the deformation of sediment waves

particle sedimentation from gravity currents flowing along the tank base in PC and TC regimes. In the context of volcanic eruptions, our definition of phoenix clouds includes co-ignimbrite plumes rising from PDCs (Dobran and Neri 1993) and clouds spreading due to detrainment of plume fluid from the eruption column below the umbrella cloud LNB (Mittal and Delbridge 2019).

In more detail, in typical BP and PC jet regimes close to the BP-PC regime boundary, as sediment waves descend, their radius increases as they flatten through entrainment and mixing while their fall speeds decline accordingly. As these features approach an evident LNB, they spread to form internal layers. Where particles detrain, entrained interstitial fluid also rises, mixes with ambient layers that are more dense than layers at the umbrella LNB, spreads laterally and can form additional internal layers (Fig. 11a–b). This process occurs even in the very strongest (smallest $-Ri_0$) jets in the BP regime, although phoenix cloud layers are difficult to distinguish from the main umbrella cloud (Fig. 12d). This behavior is in marked contrast to TC and PC regimes close to the PC-TC regime boundary where sediment waves descend to the tank base to release buoyant interstial fluid in a spatially varying buoyancy flux that reflects time-dependent sedimentation from spreading gravity currents (Fig. 11b-c).

The way in which phoenix clouds and associated internal cloud layers are produced in the PC jet regime varies across a very extensive $-Ri_0 \leftrightarrow \phi$ parameter space. In particular, phoenix clouds and cloud layers can emerge simultaneously as a result of buoyancy fluxes delivered through the partial dispersal of descending sediment waves and through sedimentation from particle-driven gravity currents at the tank base. For example, in Fig. 11b the descent and flattening of a large sediment wave (marked "1") is associated with the lateral spreading of interstitial fluid away from the particle-fluid mixture that defines the wave to form a phoenix cloud layer (pink feature marked "Phx Cld" at $t = 0.4$ s in Fig. 11b). However, when the sediment wave reaches the tank base and spreads as a gravity current, the remaining buoyant interstitial fluid ascends as a phoenix cloud that mixes with relatively dense ambient layers to form a phoenix cloud layer (pink feature marked "Phx Cld" at $t = 5.2$ s in Fig. 11b) below the previous phoenix cloud layer. Thus, a single sediment wave can produce two classes of phoenix clouds spreading into distinct phoenix cloud layers.

Periodic sediment waves, the "enhanced settling annulus" and deposit architecture

In all regimes, sediment waves descending next to the jet deposit the majority of their particle load within the "enhanced settling annulus" (region marked as SA in last

column of Fig. 11). In PC and TC regimes, the majority of sedimentation occurs where large sediment waves impact the tank base, with the remaining entrained solid fraction transported and deposited beyond the enhanced settling annulus by gravity currents. In these regimes, the maximum distance that gravity currents carry particles marks the outer edge of the "proximal" deposit. In the BP regime, most sedimentation is confined within the enhanced settling annulus and is time-dependent occurring by individual settling of particles detrained from dispersed sediment waves.

In all regimes, jets emplace deposits with a thickness that decreases, on average, monotonically from the source. Coarse particle jets in the TC regime and in the PC regime near the TC boundary (Fig. 8) are marked by step-wise changes in deposit thickness (see red arrows in Fig. 12c). These "terraced" deposits, are overall, axisymmetric and spaced quasi-periodically in radius from the nozzle. However some terraces merge or diverge at various positions around the deposit. Terraces can also show relatively small variations in radius expressed as scallop features at their terminii (black arrows in Fig. 13b). In an experiment on a bidisperse jet in the TC regime, fine particles settle over two days after the experiment to mantle the underlying terraced deposit with a uniformly thick fine particle layer (Fig. 13b–c). Therefore, terraced deposits are a robust characteristic of jets in the TC regime. Overall, deposits become less steep and more broad as jet source parameters vary from the TC to BP regimes (Fig. 12c).

Interactions between sediment waves and phoenix clouds

During coarse particle jet experiments that occur in the BP-PC-TC column regimes, we observe several types of interactions among sediment waves and phoenix clouds that are diagnostic of eruption regime: (1) successive descending annular sediment waves interacting with each other and with smaller non-axisymmetric sediment waves, (2) descending sediment waves interacting with ascending phoenix clouds and (3) ascending phoenix clouds interacting with spreading phoenix cloud layers. We summarize these interactions in Fig. 12d, which shows two sequential color inverted and frame-differenced images of a pair of sediment waves from four experiments.

For jets in the TC regime and jets in the PC regime near the TC boundary in Fig. 8, sediment waves do not interact as they fall. For jets in the PC regime near the BP boundary in Fig. 8, pairs of sediment waves can interact as they fall: the higher sediment wave merges into the lower sediment wave before the pair reach the tank base (Fig. 12d). This process can cause sediment waves to grow in volume and descend more quickly to the tank base to produce relatively more voluminous gravity currents. Sediment wave interaction can

also occur for jets in the BP regime, causing sediment waves to grow and descend relatively lower and disperse closer to the tank base than non-interacting sediment waves. This process is rare for jets in the PC regime near the BP boundary in Fig. 8 and more common for jets in the BP regime.

Figure 12e shows a stack of two (sequential) color inverted and frame-differenced images exhibiting interactions between ascending phoenix clouds and descending sediment waves from each regime. For jets in the TC regime, phoenix clouds ascend (pink arrow) above gravity currents flowing along the tank base outside of the enhanced settling annulus and do not interact with descending sediment waves (blue arrow). For jets in the PC regime near the TC boundary, some phoenix clouds ascend within the enhanced settling annulus and subsequently interact with descending sediment waves (Fig. 12c), which can lead to unsteady buoyancy fluxes to growing phoenix cloud layers, to particle detrainment and settling, and to dispersal of the descending wave. For jets in the PC regime near the BP boundary, these interactions are more common and deformation of descending sediment waves is more pronounced; the corresponding image in Fig. 12c shows more extensive deformation of a descending sediment wave than for the sediment wave in the previous example. For jets in the BP regime, phoenix clouds ascending from dispersed sediment waves interact with subsequent sediment waves; the corresponding image in Fig. 12c shows the most extensive deformation of a descending sediment wave by an ascending phoenix cloud as opposed to the previous examples in the PC and TC regimes. These interactions are most frequent and extensive in the BP regime.

As phoenix clouds ascend and spread into phoenix cloud layers, they can interact as shown in Fig. 11b. At $t = 1.2$ s, buoyant interstitial fluid spreads from the second small sediment wave (marked "2") to produce another phoenix cloud. At $t = 3.6$ s this phoenix cloud merges with the phoenix cloud that spread directly from the previous large sediment wave (marked "1"), demonstrating that phoenix clouds spreading from separate sediment waves can interact.

Principal qualitative results: a summary

1. As $-Ri_0$ and ϕ_0 increase from 1.4×10^{-5} and 6×10^{-3} to 1.2×10^{-3} and 6.0×10^{-2} among experiments that span the BP, PC and TC regimes in Fig. 8, we observe gradual changes in overall sediment wave behavior, column height fluctuations, umbrella and phoenix cloud structures and deposit architecture (Fig. 12).

2. In all regimes, jet mixture periodically collapses from the overshoot or LNB region of the jet column as large and small sediment waves.

3. The maximum radius that sediment waves extend from the jet axis marks the boundary of the enhanced settling annulus, beyond which only continuous individual particle settling is observed for coarse particle jets.

4. In the BP regime,

   (a) Asymmetric small sediment waves disperse before reaching the tank base. Detrained particles settle individually thereafter.

   (b) Buoyant interstitial fluid carried by descending sediment waves can spread to form cloud layers below the umbrella cloud.
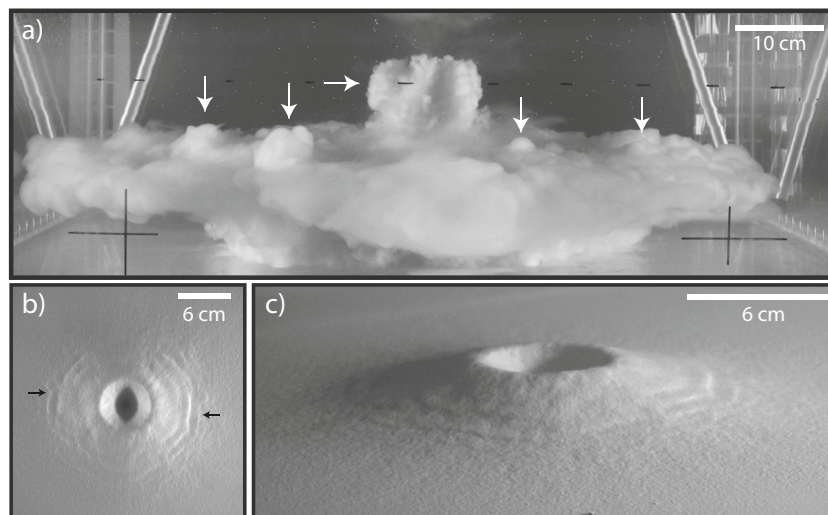
Fig. 13 (a) Bidisperse experimental jet in the TC regime (Supplemental Video 2). The top of the jet grows and collapses (horizontal arrow) periodically. Gravity currents spread out axisymmetrically from the jet source with phoenix clouds ascending above the gravity currents to create a veil around the jet column. Phoenix clouds spread into a single phoenix cloud layer at a height below the average height of the jet column. Overshooting phoenix cloud tops are marked with vertical arrows (cf. Figure 2 in Herzog and Graf 2010). (b) Top view of terraced deposit emplaced by bidisperse jet in the TC regime. (c) Oblique view of terraced deposit in (b)

    (c) Deposit thickness decreases monotonically and smoothly away from the vent over the whole tank base.

5. In the TC regime,

    (a) Annular large sediment waves descend around the jet column and carry buoyant interstitial fluid to the tank base.

    (b) Sediment waves spread as particle-driven gravity currents along the tank base.

    (c) Particle sedimentation from gravity currents releases buoyant interstitial fluid that ascends as phoenix clouds that spread as phoenix cloud layers.

    (d) Terraced deposits are a characteristic feature of the TC regime.

6. In the PC regime,

    (a) The injected mixture is partitioned into a spreading umbrella cloud and descending sediment waves simultaneously.

    (b) Sediment waves descend around the jet column and can carry buoyant interstitial fluid to multiple heights between the LNB and tank base.

    (c) When sediment waves reach the tank base, they spread as gravity currents.

    (d) Phoenix clouds ascend above gravity currents.

    (e) Buoyant interstitial fluid can spread from the outer part of sediment waves or from dispersed sediment waves to form internal phoenix cloud layers.

    (f) Multiply layered clouds are another characteristic feature of this regime.

    (g) As $-\mathrm{Ri}_0$ and ϕ_0 increase from 2.4×10^{-5} and 6.0×10^{-3}, terraces in the proximal deposit within the enhanced settling annulus become more pronounced.

7. Descending sediment waves in the BP and PC regime can merge, causing sediment waves to descend farther and faster than they would without this interaction.

8. Ascending phoenix clouds in the BP and PC regime can interact with descending sediment waves and cause them to disperse. Phoenix cloud interaction with sediment waves in the TC regime is less important as it is limited to the outer part of sediment waves

## Quantitative results: links between source parameters and sediment wave dynamics

The mechanical links among jet source parameters, jet structure, column height oscillations, sediment wave dynamics and deposit architectures are critical for reconstructing eruption dynamics and evolution on the basis of remote

sensing observations and analyses of deposits in the field. Accordingly, in this section we use the summary in "Principal qualitative results: a summary" to guide a more rigorous analysis aimed at probing some of the main underlying processes at work to control these links in our $-\mathrm{Ri}_0 \leftrightarrow \phi \leftrightarrow \mathrm{St}$ parameter space. As we discussed in the "Introduction", a critical control on jet regime for given source and environmental conditions is the rate at which ambient fluid is entrained into particle-laden jets (cf. Eq. 1). Thus, our first step will be to use a conventional one-dimensional integral model to determine an effective entrainment parameter for each experiment (cf. Morton et al. 1956; Turner 1966; Jessop and Jellinek 2014). We next apply these and other results to broadly compare jet heights predicted from scaling considerations to measured average jet top and umbrella cloud LNB heights. We then focus on a characteristic jet in the TC regime alone and compare time series of periodic jet top height oscillations, of annular large sediment waves, and of the structure of terraced deposits. In a subsequent section we more broadly characterize the spectral properties of periodic jet height oscillations in each regime. In particular, we show that predominant oscillation modes for each regime are consistent with theoretical expectations on the basis of the source parameters and that these modes are generally similar to observed frequencies for sediment waves. From the distinct characters of average power spectra for each regime, we also constrain key differences in the way turbulent kinetic energy is dissipated in BP, PC and TC regimes. Last, we conclude this section with a characterization and comparison of a number of aspects of sediment wave dynamics across the three regimes: descent velocity, wavelength between pairs and their radius. From these results we infer properties including the average sedimentation number of particles in descending sediment waves and consequently constrain novel effects related to both particle and interstitial fluid buoyancy.

Effective entrainment parameter

The regime and rise height of a multiphase jet is sensitive to the rate of entrainment of ambient fluid (see Eqs. 1 and 22a-22c; Morton et al. 1956; Kaminski et al. 2005; Woods 2010). To estimate an effective value of the entrainment parameter, α_e for each experiment, we use a 1D integral plume model (Appendix B) to find effective entrainment parameter values that reproduce the observed maximum height of the jet as it first enters the tank, which occurs within the first ≤ 10 s (transient phase) of an experiment. Figure 14 shows the mean value of α_e determined for particle-free, monodisperse and bidisperse jets in this study. The particle-free jet in the TC regime (experiment #29 in Table 2) has $\alpha_e = 0.055$ and is in agreement within uncertainties with the value $\alpha_{ftn} = 0.057$ found for particle-free fountains in (Kaminski et al.

Source Richardson Number vs. Effective Entrainment Parameter
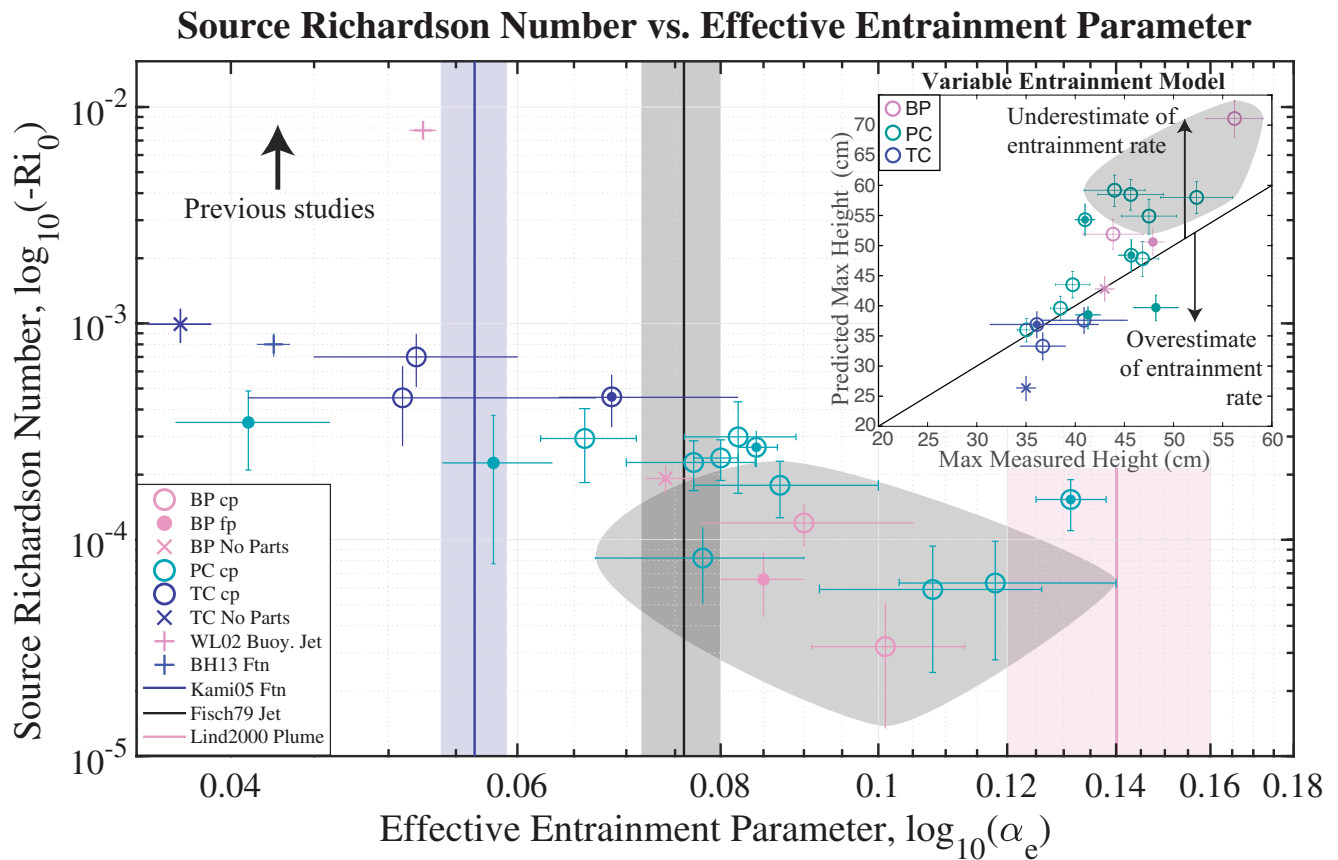
Fig. 14 Source Richardson number plotted against the effective entrainment parameter for all experiments in this study (Table 2). Coarse particle (cp) experiments (open circles), fine particle (fp) dots), bidisperse (filled circles) and particle-free (X). Blue and black solid lines, with shaded uncertainties, give the effective entrainment parameters for momentum-driven fountains from the experimental results and analytical model of Kaminski et al. (2005) and from experiments and an empirical model in Fischer (1979). The pink line is the effective entrainment parameter for buoyant plumes along with shaded experimental uncertainties from Linden (2000). All constant α values are for particle-free flows. Blue cross marker from Wang and Law (2002) and pink cross marker from Burridge and Hunt (2013). The majority of previous studies investigate entrainment into jets and plumes with $-Ri_0 > 10^{-2}$ (black arrow), outside of the $-Ri_0$ range investigated in this study. Gray shading encompasses coarse particle jets ($0.48 < St_0 < 6.00$) & $2.7 \times 10^{-3} < \Sigma_0 < 2.6 \times 10^{-2}$) with buoyant interstitial fluid. **Inset:** measured versus predicted maximum jet height from the model of Kaminski et al. (2005)

2005). For the particle-free jet in the BP regime (experiment #28 in Table 2) $\alpha_e = 0.074$ and agrees within uncertainties with the value $\alpha_{jet} = 0.076$ reported for particle-free non-buoyant jets in (Fischer 1979).

For coarse particle jets, as $-Ri_0$ is decreased from 8.9×10^{-4} to 1.4×10^{-5}, α_e increases from 0.051 to 0.118. Coarse particle jets in the TC regime have $0.051 < \alpha_e < 0.052$, also consistent with the value for particle-free fountains from (Kaminski et al. 2005). Coarse particle jets in the BP and PC regimes have $0.066 < \alpha_e < 0.131$, which lie between the values for particle-free jets and plumes. Fine particle jets in the PC regime have $0.041 < \alpha_e < 0.058$ and only experiment #49 (Table 2) agrees with the particle-free jet value. The fine particle jet in the BP regime has $\alpha_e = 0.085$, which lies between the values for particle-free jets and plumes. For coarse particle jets in the BP and PC regimes that have buoyant interstitial fluid (gray shading in

Fig. 14) $0.078 < \alpha_e < 0.118$ and approaches $\alpha_{plume} \approx 0.14$ (Linden 2000) as $-Ri_0$ decreases.

To investigate the effect of particles on the local rate of entrainment we use the variable entrainment model (Eq. 24 with Eqs. 22a-22c; see Appendix B) to compare modeled and measured maximum jet heights (inset in Fig. 14). For coarse particle jets in the BP and PC regimes with buoyant interstitial fluid (experiments #35, 36, 46, 48 & 54; Table 2), a coarse particle jet in the BP regime (#52), a coarse particle jet in the PC regime (#42), a jet with both particles in the PC regime (#14), and the fine particle jet in the BP regime (#16), the variable entrainment model overestimates the the maximum jet height, and therefore, underestimates the rate of entrainment. For a coarse particle jet in the TC regime (#30), both fine particle jets in the PC regime (#49 & 50), and the particle-free jet in the TC regime (#29), the variable entrainment modeled maximum jet height underestimates

Fig. 15 **Top:** Predicted jet height from fountain height scaling (Eq. 7) plotted against measured average jet heights during the steady-state period of experiments. Coarse particle experiments marked with open circles, fine particle experiments with dots, bidisperse experiments with circles filled with dots and particle-free with X markers. Grey shading indicates coarse particle jets with buoyant interstitial fluid (Table 1). Black line shows best fit of Eq. 7 with $C_{ftn} = 1.30$ for jets with dense interstitial fluid, whereas $C_{ftn} = 0.68$ for jets with buoyant interstitial fluid (**Top inset**) in Eq. 7). **Bottom:** Predicted jet height from fountain height scaling (Eq. 7) using $C_{ftn} = C_{ftn}(\sigma)$ (Bloomfield and Kerr 1999) plotted against measured average jet heights during the steady-state period of experiments. **Bottom inset:** Predicted LNB height from plume height scaling (Eq. 6) plotted against measured LNB heights of umbrella clouds for jets in the BP and PC regimes. Black line shows best fit of Eq. 6 with C_{pl} for coarse particle jets with buoyant interstitial fluid (gray shading)

Fountain Height Scaling vs. Measured Average Steady-State Height

Fountain Height Scaling vs. Measured Average Steady-State Height
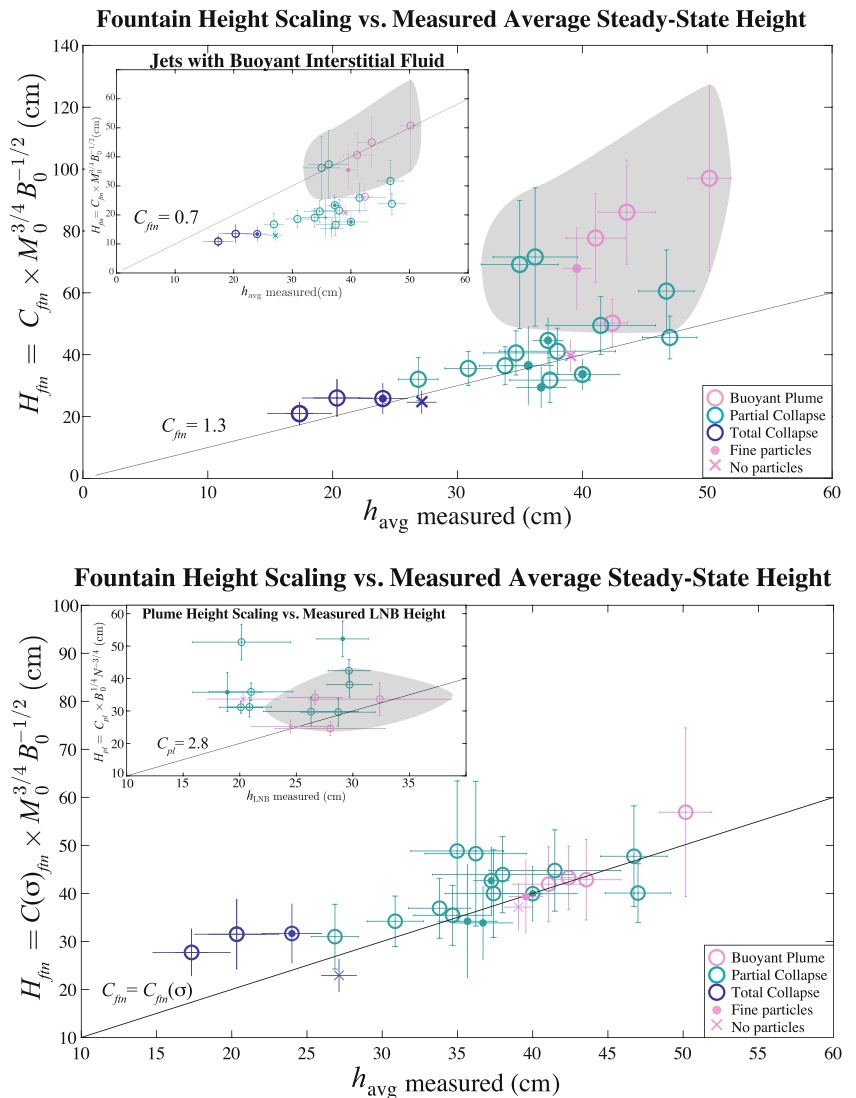
the measured maximum jet height, therefore, overestimating the rate of entrainment. For all other jets (experiments #20, 23, 27, 28, 39, 43 & 51) the variable entrainment modelled maximum jet heights agree within uncertainty with measured maximum jet heights (Fig. 14).

Geometric constants for jet height scalings

With measurements of jet source parameters for each experiment, we test whether Eqs. 6 and 7 are appropriate for predicting jet column top height and fluid LNB, respectively, for jets with particles in the BP and PC regime, as well as the best-fit value of C_{ftn} jet heights in all regimes (Fig. 15). For jets in all regimes with non-buoyant interstitial fluid at the source, Eq. 7 shows good agreement with measured average jet heights and $C_{ftn} = 1.3$ within measurement uncertainty. Jets with non-buoyant interstitial fluid at the source have $1 < \sigma < 70$ (Eq. 8), which leads

to $1.0 < C_{ftn} < 1.9$ using Eq. 9 and is in agreement with our value of $C_{ftn} = 1.3$ found using a linear regression fit of Eq. 7 to measured maximum jet heights. For jets with buoyant interstitial fluid at the source, $C_{ftn} = 0.7$ shows better agreement than $C_{ftn} = 1.3$ (inset Fig. 15). Jets with buoyant interstitial fluid at the source have $100 < \sigma < 500$ (Eq. 8), which leads to $0.7 < C_{ftn} < 0.9$ using Eq. 9 and is in good agreement with our value of $C_{ftn} = 0.7$ found using a linear regression fit of Eq. 7 to measured average jet heights (Bloomfield and Kerr 1999). Where predicted average jet heights are calculated using Eq. 7 with $C_{ftn} = C_{ftn}(\sigma)$ (Eqs. 8 and 9), they show good agreement with measured average jet heights for experiments in the BP and PC regimes (bottom graph in Fig. 15). However, equation 7 with $C_{ftn} = C_{ftn}(\sigma)$ overestimates average jet height for coarse particle and bidisperse experiments in the TC regime.

For jets with non-buoyant interstitial fluid at the source Eq. 6 overestimates the LNB heights for all other jets

Table 4 Jet top height oscillation frequencies

Regime	f_1	f_2	f_{ftn}	f_{OS}	$N[1/s]$	f_2/f_1	Energy Dissipation
BP	0.50 ± 0.32	2.60 ± 0.28	0.65 ± 0.16	2.53 ± 0.46	0.10 ± 0.01	5.20 ± 3.37	Molecular mixing
PC	0.74 ± 0.40	2.53 ± 0.27	0.85 ± 0.20	2.46 ± 0.69	0.10 ± 0.01	3.42 ± 1.88	Heating
TC	1.36 ± 0.24	2.35 ± 0.21	2.66 ± 0.78	–	0.10 ± 0.01	1.73 ± 0.34	Unknown

For each regime, dominant dimensionless frequencies f_1 and f_2 identified in representative power spectra, predicted jet f_{ftn} and overshoot f_{OS} frequencies, ratio of dominant frequencies f_2 over f_1, and best fit energy dissipation scales (Heating $\equiv$ Kolmogorov & Molecular mixing $\equiv$ Ozmidov). Characteristic frequencies for each regime are normalized to the BV-frequency N for that regime. All values reported in this table are also shown on Fig. 17

in the BP and PC regimes (bottom inset in Fig. 15). In contrast, Eq. 6 with $C_{pl} = 2.7$ shows good agreement when plotted against measured LNB heights for jets with buoyant interstitial fluid in the PC and BP regimes.
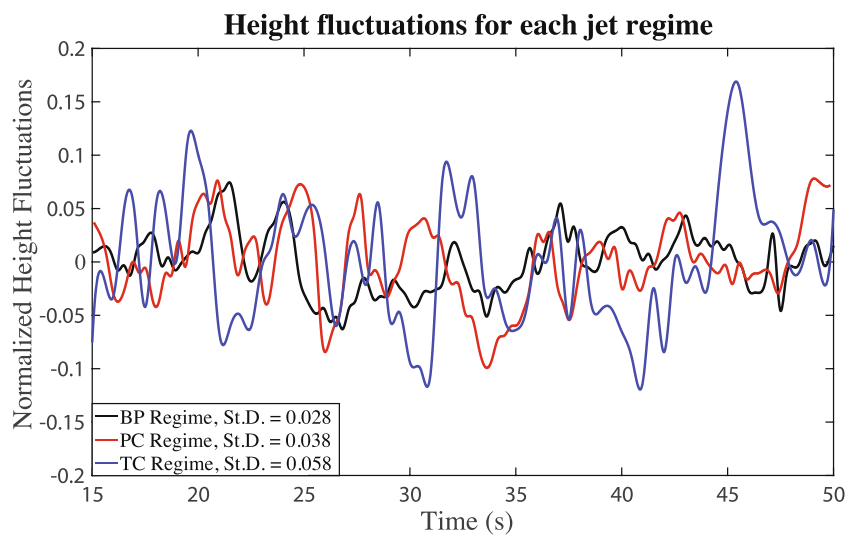
Spectral analysis of jet height oscillations

Figure 16 shows typical statistically stationary jet column top height fluctuations about the average jet height for the BP, PC and TC regime. Jet top height fluctuations have the smallest amplitude for particle-free, coarse- and fine-particle jets in the BP regime. As $-Ri_0$ and ϕ_0 are increased and jets occur in the PC to TC regimes (Fig. 8), the magnitudes of jet top height fluctuations and standard deviations of the height time series are two times larger for jets in the TC regime than for jets in the BP regime.

The characters of particle-free, fine- and coarse-particle jet height fluctuations vary among the BP, PC and TC regimes. To capture periodic components in the temporal variability of jet top height oscillations, evident in Fig. 20, we estimate the representative power spectra for each jet regime (see Section "Spectral analysis of jet height oscillations" for method). In the BP regime, the predicted

fountain frequency, f_{ftn}, (cf. Eq. 10) and N both overlap, within measurement uncertainty, with a frequency of jet height oscillation with the greatest power, $f_1 = 0.50 \pm 0.32$ (Table 4 and Fig. 17). The predicted overshoot frequency, f_{OS}, and measured frequency of small sediment waves, f_{SmlSW}, (cf. Eqs. 12 & 2, respectively) both overlap with a second well-resolved frequency $f_2 = 2.60 \pm 0.28$, that has 50% of the maximum power of the spectrum. In the TC regime, by contrast, we resolve a peak at $f_1 = 1.36 \pm 0.24$, which overlaps with the BV-frequency N. The predicted fountain frequency f_{ftn} and the frequency of large sediment waves, f_{LrgSW}, both overlap with a second resolved peak at $f_2 = 2.35 \pm 0.21$ that has 90% of the maximum power of the spectrum.

In the PC regime the predicted fountain frequency, the BV-frequency N and the frequency of large sediment waves overlap with the dominant frequency of jet height oscillations $f_1 = 0.74 \pm 0.40$ that has the maximum power (Table 4 and Fig. 17). The predicted overshoot frequency overlaps with the measured frequency of small sediment waves. Both of these frequencies also overlap with a second dominant frequency of jet height oscillation, $f_2 = 2.53 \pm 0.27$, that has 25% of the maximum power of the spectrum.

Fig. 16 Steady-state height fluctuations for experiments representative of the BP (top), PC (middle) and TC (bottom) regimes. These time series are derived from jet top height time series that are detrended, demeaned and normalized to the mean jet top height. St. D. in the legend is the standard deviation for each time series

More generally, we can distinguish the end-member BP and TC regimes spectrally in terms of frequencies of height oscillations as well as through the distribution of power among the modes. Comparing the spectra of each regime, jet height oscillations in the BP and PC regimes show the most power at the fountain and BV-frequencies, which overlap within uncertainty. On the other hand, in the TC regime the fountain and BV-frequencies are distinct from one another with 10% more power delivered to the latter over the former (Table 4 and Fig. 17). The ratio of the two dominant frequencies f_2/f_1 decreases progressively from the BP→PC→TC regimes. In the BP and PC regimes, f_{SmlSW} overlaps with f_{OS} and f_2, whereas in the TC regime f_{SmlSW} does not appear to overlap with any significant frequency peaks in the power spectra.

We analyze the mechanism by which kinetic energy delivered by the jet height oscillations is transferred from the largest motions corresponding to the lowest sediment wave frequency to higher frequencies, where it is dissipated (right column in Fig. 17). To identify the existence of a continuous energy cascade and to determine whether the predominant irreversible energy sinks for mechanical energy are the production of heat by turbulent dissipation (Kolmogorov 1941) or through a change in the gravitational potential energy of the system by molecular mixing of density interfaces (Ozmidov 1965) we identify and compare the slope of the power spectrum to classical Kolmogorov and Ozmidov scalings shown in Fig. 17. The spectral slope for jets in the BP regime (right column of top panel in Fig. 17), taken from a corner at $\log_{10}(f/N) \approx 0.60$, is explained with the Ozmidov scaling. In the PC regime, from a corner at $\log_{10}(f/N) \approx 1.00$ to $\log_{10}(f/N) \approx 0.60$ (right column of middle panel in Fig. 17), the data are better explained by the Kolmogorov scaling. Thus, the predominant mechanisms for energy dissipation at relatively high frequencies compared to the BV-frequency in the BP and PC regimes are distinct. In the TC regime, by contrast, from a corner frequency at $\log_{10}(f/N) \approx 0.30$ (right column of bottom panel in Fig. 17) there is no clear spectral slope and therefore no evidence for a continuous exchange of energy among scales of motions emerging in these flows. Although we observe the excitation and breaking of waves, turbulent entrainment generated as a result of height oscillations and the descent of large sediment waves from the jet top (e.g. Figs 8c & 13 and Supplemental Video 2), these results are inconsistent with fully developed turbulence..

Jet source parameters, sediment wave velocity and sediment wave longevity

To understand the control of source parameters on the likelihood that sediment waves will disperse at some height

above the tank base or descend to the tank base as a coherent mixture that can spread as a gravity current (cf. Figs. 11a & c), as well as the sensitivity of this behavior to interstitial fluid buoyancy, we measure their descent speed and frequency as a function of the source Richardson number Ri_0. Using this speed and the wave size to determine an advective flow time, u_{SW}, and the terminal settling velocities of particles, u_s, we define a Sedimentation number for entrained particles as $\Sigma_{SW} = u_s/u_{SW}$ (see "Scaling natural volcanic jets to the laboratory setting"). If $\Sigma_{SW} < 1$, particles remain coupled to motions within sediment waves, whereas for Σ_{SW} particles detrain and settle individually, causing the wave to disperse as it falls– a characteristic qualitative feature of jets in the BP regime discussed above. Consistent with this observation, for a single large sediment wave in exp. #52, Σ_{SW} increases from 0.36 to 1.00 before reaching the tank base (Fig. 18a). By contrast, for jets in the TC regime, Σ_{SW} initially decreases as sediment waves accelerate downwards then Σ_{SW} increases as sediment waves approach the tank base and decelerate, but remains $\Sigma_{SW} < 1$.

In Fig. 19a, we present $-Ri_0$ versus Σ_{SW}^{min} and we indicate experiments with buoyant interstitial fluid with gray shading. Large sediment waves excited in the TC regime descend with the highest speed and, in turn, have the lowest minimum sedimentation number, $0.50 < \Sigma_{SW}^{min} < 0.60$. More slowly descending sediment waves in the PC regime span the range $0.68 < \Sigma_{SW}^{min} < 0.97$. The most slowly descending sediment waves in the BP regime have minimum sedimentation numbers that are, on average, $\Sigma_{SW}^{min} = 0.86$. As a last comment here, Σ_{SW}^{min} will increase as the fall speed of waves increases with increasing particle volume fraction that occurs from BP to PC to TC regimes. This observation reflects the differing particle buoyancy fluxes carried by sediment waves away from the overshoot regions in each regime and it is useful to estimate what are the relative particle loadings, which we constrain with the aid of a 1D integral plume model as is discussed in Appendix B (Fig. 19b).

The overall propensity for sediment waves to disperse before they reach the tank base depends on Σ_{SW}^{max}, which will decline as the fall speed of waves increases with increasing particle volume fraction (Fig. 19). As the particle volume fraction entering the overshoot region increases among experiments, Σ_{SW}^{max} decreases. There is no statistically significant separation between jets with negatively or positively buoyant interstitial fluid.

Whereas the presence of particles is a primary control on the buoyancy of jet and sediment wave mixtures, the contribution of the buoyancy of interstitial fluid ("Interstitial fluid buoyancy") in these mixtures to jet rise height, sediment wave dispersal height and, ultimately, jet regime, is unclear. In particular, provided it remains coupled to the
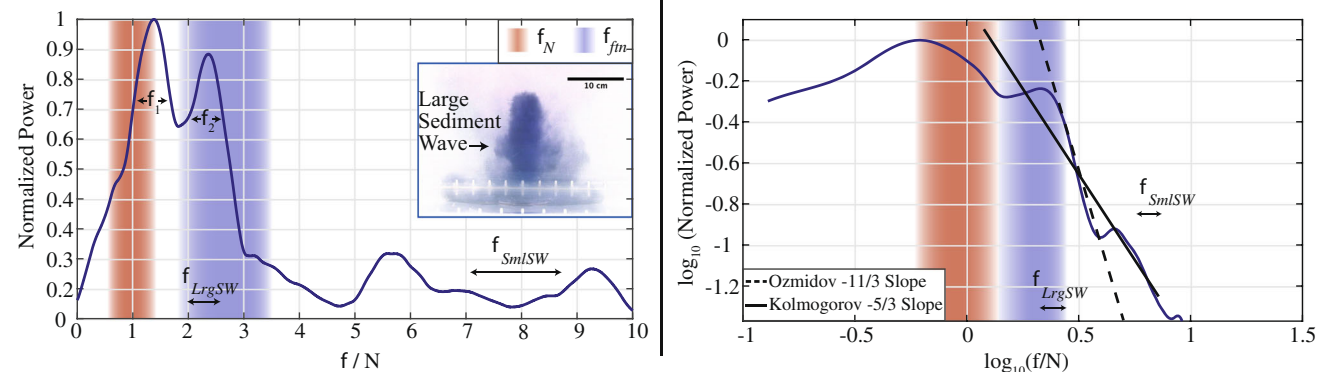
BP Regime Jet Height Oscillation Frequency Power Spectrum
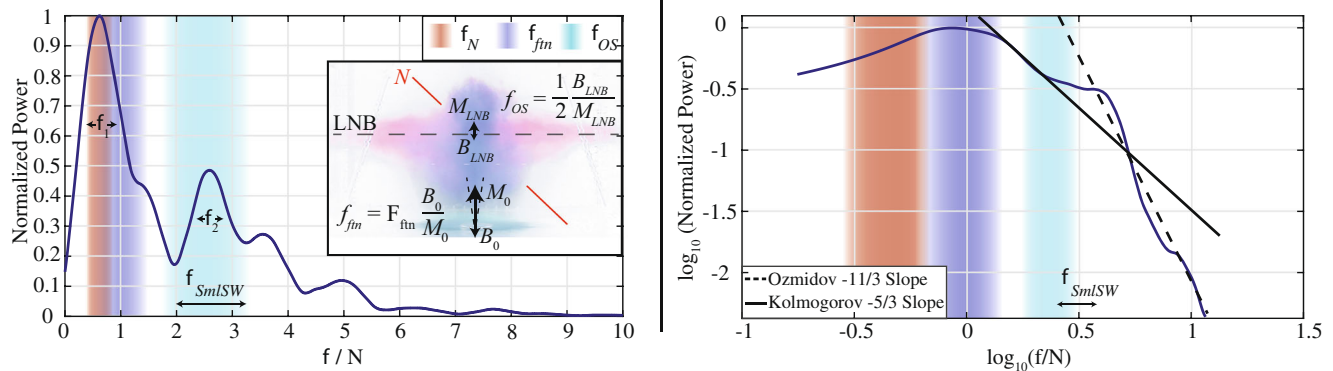
PC Regime Jet Height Oscillation Frequency Power Spectrum
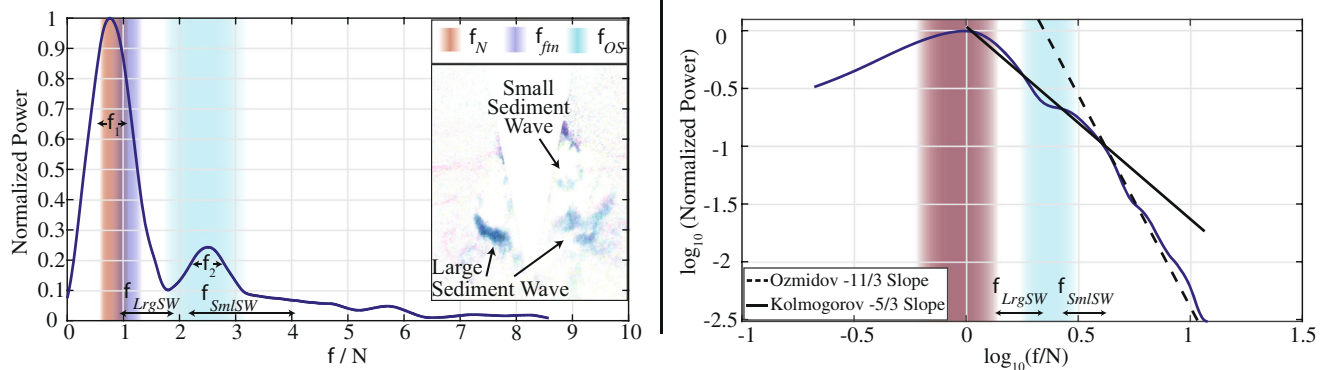
## TC Regime Jet Height Oscillation Frequency Power Spectrum

Fig. 17 Representative power spectra of steady-state jet top height time series for coarse particle jets in the BP, PC and TC regimes (panels) in linear (left column) and log space (right column). Power spectra from each experiment are normalized to the BV-frequency (i.e. N, Tables 1 & 4) and then stacked and averaged on the basis of regime to produce representative spectra (see "Spectral analysis of jet height oscillations"). Blue, green and red shading indicate f_{ftn}, f_{OS} and f_N, respectively, as ranges covering measurement and modeling error. Black horizontal bars show measured frequencies of large and small sediment waves, as ranges over measurement error. Solid (Kolmogorov) and dotted lines (Ozmidov) in right column show fitted energy dissipation scalings assuming irreversible losses are predominantly by frictional heating and molecular mixing across density interfaces, respectively (see text). To facilitate comparisons of spectral power distributions among the three regimes, power is normalized to the maximum power in the dominant (fundamental) mode in each example. **Top panel**: Power spectrum for experiment 52 and average power spectrum for experiments 48 and 52 (Table 1). **Middle panel**: Power spectrum for experiment 23 and average power spectrum for experiments 23, 35, 36, 39, 42, 46, and 51. **Bottom panel**: Power spectrum for experiment 30 and average power spectrum for experiments 27, 30 and 43

entrained particles within the mixture positively buoyant interstitial fluid augments the source momentum flux for

each jet and causes $-Ri_0$ to decrease as it drives the bulk density of the mixture more towards the ambient density

Sediment Wave Sedimentation Number During Descent

a) Buoyant Plume

b) Total Collapse
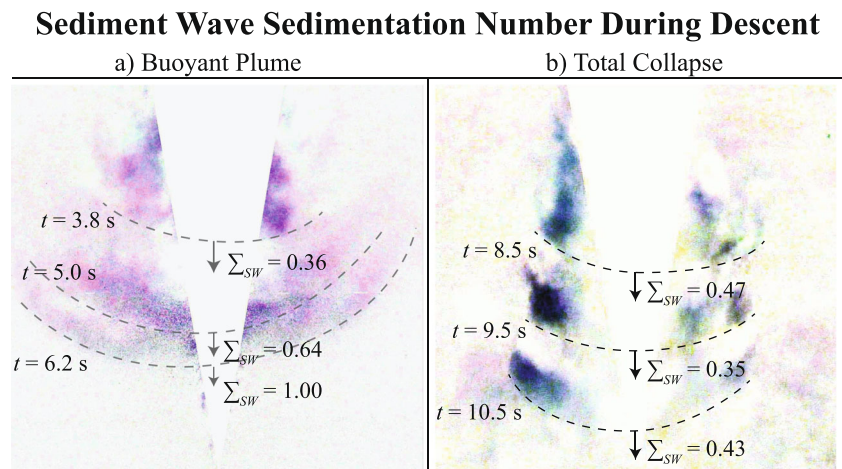
(gray regions in Figs. 14, 15 & 19). In this case, positively buoyant interstitial fluid will push jets to occur in the PC and BP regimes (Fig. 8). To gauge effects on sediment waves more insightfully, in Fig. 19c, we show $-Ri_0$ vs. the sediment wave frequency expressed through a Strouhal number Str (Eq. 15) for the same experiments presented in Fig. 19a & 19b. Jets with dense interstitial fluid in the TC regime have the highest frequencies compared to the buoyancy frequency N and are in the range $0.85 < Str_{SW} < 1.25$. By contrast, jets with dense interstitial fluid occur in the PC and BP regimes with relatively lower frequencies, $0.42 < Str_{SW} < 0.78$.

Overall, the buoyancy of interstitial fluid ("Interstitial fluid buoyancy") separates experiments in the $-Ri_0 \leftrightarrow \phi_0$, $-Ri_0 \leftrightarrow \alpha_e$, $-Ri_0 \leftrightarrow \Sigma_{SW}$ and $-Ri_0 \leftrightarrow Str_{SW}$ parameter spaces (Figs. 8, 14, 15, 19a & 19c), and leads to a factor two difference in the coefficient for the jet height scaling (Eqs. 7, 8 & 9 and Fig. 15). Importantly, positively buoyant interstitial jet fluid does not prevent sediment waves from descending to the tank base to spread as ground-hugging gravity currents. As a final remark here, we reiterate that these preliminary results are for conditions where buoyant interstitial fluid remains predominantly coupled to entrained particles during the time to rise to H_{ftn} (cf. Eq. 7). Potential more complicated effects related to extensive separation of buoyant interstitial fluid from the relatively dense particle phase in the jet mixture may enter for particle sedimentation number $\Sigma > 1$. Such complications will also enter into more complete analyses of thermal buoyancy effects in natural eruptions and are beyond the scope of this work.

TC jet height, large sediment waves and resultant deposit architecture

Sediment waves are observed visually to coincide with fluctuations in column height for fine- and coarse-particle jets and this behavior is most apparent for jets in the TC regime. We observe that a large amplitude and long period fluctuation in jet height is linked spatially to the occurrence of a large sediment wave and a terrace in the resultant deposit (Fig. 20).

Prior to reaching a statistically stationary average jet height, the initial jet rises to a global maximum within the first ~ 5 s of the experiment. After this initial jet rise in a quiescent ambient fluid, descending jet fluid above and along the jet edges lowers the average jet height as the jet transitions into the steady-state period.

During the steady-state period, evident after ~ 5 s, the time series show a dominant oscillation with a period of ~ 7 s and amplitude of ~ 3.5 cm. Inset color inverted images in Fig. 20, paired with their frame-differenced counterparts, show four distinct instances, the first of which occurs at the end of the transient period, where a large sediment wave falls around the jet as the height approaches a local minimum value in the time series. Inset images a) and b) in Fig. 20 show four abrupt changes in the thickness of the annular deposit (deposit terraces). The terraces are approximately axisymmetric with small wavelengths and small amplitude variability in radius with azimuth.

The expression of terracing in deposit architectures depends on the particle loading. Figure 21 compares two cases with different source particle volume fraction. Where terraces are present, the slope of the deposits is below the angle of repose for the saturated particle-fluid mixture in the experiment (or the mixtures would collapse). The terraces also extend radially at a regularly spaced wavelength from the rim of the conical deposit, $1.2 < \lambda_{dep} < 1.9$ cm, (exp. #27; Table 2). However, for experiments in the TC regime that inject a relatively high overall total mass of particles (e.g. exp. #30), terraces are only apparent near the outer boundary of the enhanced settling annulus (Fig. 21b). For both deposits in Fig. 21, the farthest terrace is within 1.5 times the average jet radius from the vent.

Fig. 19 For jets with coarse particles in the BP regime (experiments # 48 & 52; pink markers), PC (# 23, 35, 36, 39, 42, & 46; green markers) and TC (# 27 & 30; blue markers) regimes, we plot, in log space, (a) the source Richardson number against the minimum measured Sedimentation number, defined with the maximum sediment wave velocity for that experiment $\Sigma_{SW}^{min} = u_p/u_{SW}$, for particles carried by sediment waves during an experiment and (b) minimum sedimentation number versus particle volume fraction taken at the LNB. (c): Source Richardson number against the Strouhal number for small sediment waves. In all plots, gray shading highlights experiments with buoyant interstitial jet fluid

a) Source Richardson Number vs. Sedimentation Number at LNB

b) Particle Volume Fraction at LNB vs. Sediment Wave Sedimentation #

c) Source Richardson Number vs. Sediment Wave Strouhal Number
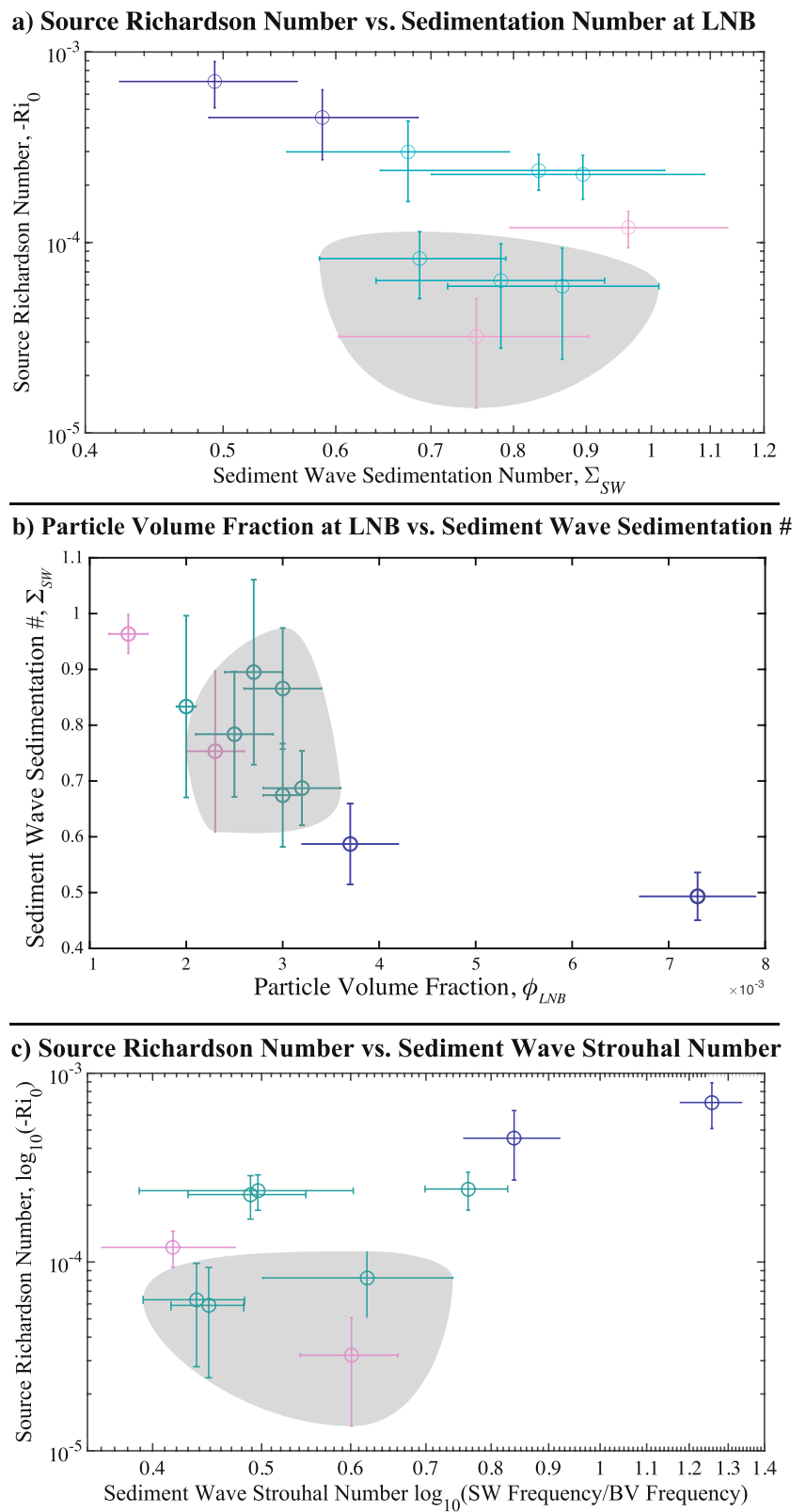
Principal quantitative results

Taken together, the entrainment parameter, height scaling, spectral, sediment wave dynamics and deposit geometry results support the following general characteristics of each steady-state jet regime:

1. Buoyant Plume (BP) regime

   (a) A variable entrainment model assuming a local $-Ri$ control (Eq. 24 in Appendix B; cf. Kaminski et al. 2005) underestimates the entrainment rate for monodisperse coarse particle jets with $3.8 \pm 1.8 < St_0 < 6.0 \pm 2.8$ (inset in Fig. 14).

   (b) The average jet height during steady-state is best predicted by Eq. 7 with $C_{ftn} = 0.7$ for jets with positively buoyant interstitial fluid and $C_{ftn} = 1.3$ for a jet with dense interstitial fluid (Fig. 15).

   (c) For steady-state coarse particle jets, the dominant frequency with the second largest power of periodic jet height oscillations, f_2 in top panel of Fig. 17, overlaps with the frequency of small sediment waves, f_{SmlSW} in top panel of Fig. 17, which is predicted by Eq. 12.

   (d) Jet height oscillations with the maximum power correspond to the fountain frequency and the response of the density stratification of the ambient fluid.

   (e) Jet height oscillations above f_2, f_{OS} and f_{SmlSW} decay in power with a well-defined power spectral slope that is comparable with a classical Ozmidov scaling, which indicate that the rise and spread of coarse particle jets and the descent of small sediment waves below the LNB in the BP regime involves extensive mixing across the ambient density stratification (Fig. 17).

   (f) For coarse particle jets, through lateral spreading and entrainment, the descent speed of sediment waves decreases rapidly to the terminal settling velocity of particles and sediment waves disperse before reaching the tank base (Figs. 18 & 19).

2. Total Collapse regime

   (a) A variable entrainment model of jet rise (Eq. 24 in Appendix B; cf. Kaminski et al. 2005) estimate for the rate of entrainment agrees well with a coarse particle jet and a jet with coarse and fine particles, although it does not capture the behavior of weaker (higher $-Ri_0$) coarse particle and particle free jets (inset in Fig. 14). For a constant entrainment model of jet rise an effective entrainment parameter value $\alpha_{ftn} = 0.057$ agrees well with all jets except for the jet with both coarse and fine particles, which has $0.063 < \alpha_{ftn} = 0.082$ (Fig. 14).

   (b) The average jet height is best predicted by Eq. 7 with $C_{ftn} = 1.3$.
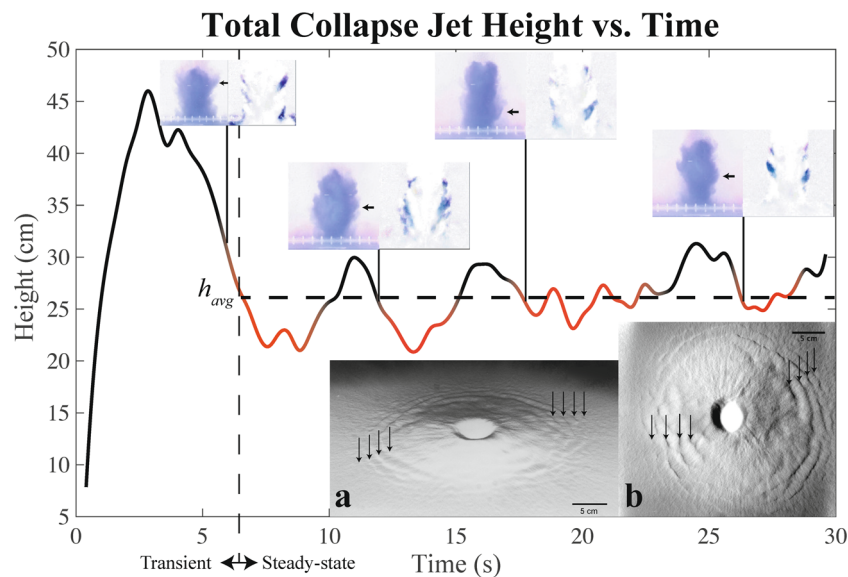
Fig. 20 Time series of jet column top height of experiment #32 jet in the TC regime. Following an initial ~ 5 s transient, the jet height evolves to a statistically stationary mean with a variability related to relatively long period sediment waves and shorter period oscillations related to the jet dynamics and stratification (see text). Red segments of height curve highlight four local minima in height that follow the occurrence of large sediment waves descending around the jet. The time of each large sediment wave occurrence is marked with a vertical line connecting to a pair of inverted color and frame-differenced images of the large sediment wave, which is highlighted in the images with a black arrow. (a) Black and white image taken from an oblique angle of the resultant deposit from this experiment. Black arrows mark four distinct concentric terraces at varying radii from the vent in the middle. (b) Top view of same deposit

a) **Low Total Particle Mass Injected**   b) **High Total Particle Mass Injected**
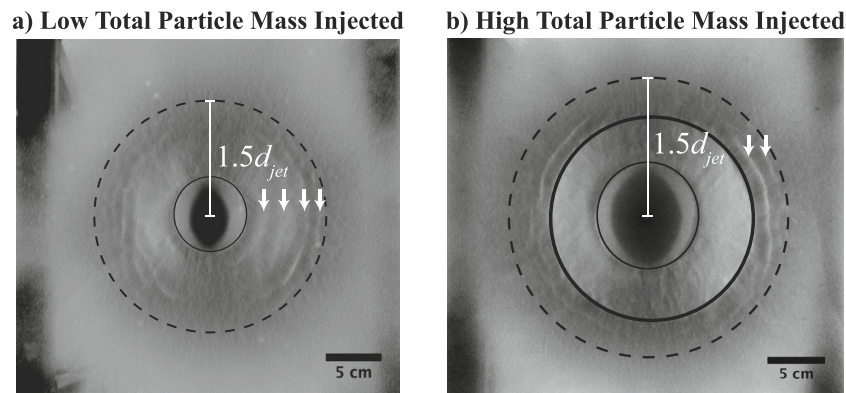
Fig. 21 Images of deposits emplaced by two coarse particle jets in the TC regime with different source particle volume fractions. (a) Deposit emplaced during experiment #30, in which 411 g total mass of particles was injected during the experiment. Terraces are marked with white arrows, rim on the deposit cone marked with a solid circle and the outer boundary of the enhanced settling annulus marked with a dotted circle. (b) Deposit emplaced during experiment #27, in which 628 g total mass of particles was injected during the experiment. The cone at the angle of repose of the coarse particles is bounded by solid circles and occurs between the nozzle and the terrace with smallest radius

   (c) For all steady-state jets, the frequency of periodic jet height oscillations with the second highest power overlaps with the frequency of large sediment waves, which is predicted by Eq. 10 (Fig. 17). The dominant frequency with the most power overlaps with N (Eq. 4). There is no well-defined power spectral slope. Therefore, there is no evidence of a continuous energy cascade and thus the dissipation mechanism does not involve predominantly mixing, or heat generated through fully developed turbulence.

   (d) For coarse particle jets, sediment waves descend to the tank base at a speed larger than the particle settling speed (Figs. 18 & 19).

   (e) Estimated particle volume fractions and frequencies of large sediment waves are larger for jets in this regime than for jets in the BP or PC regimes (Fig. 19b).

   (f) Jet height oscillations are linked to the frequency of occurrence of large sediment waves, which in turn are linked to the emplacement of terraces in the resulting deposit (Fig. 20).

   (g) The radius of the outermost terrace in the proximal deposit is less than $1.5\times$ the jet diameter at the average jet height. Terraces can be restricted to a smaller radial range of the proximal deposit for jets with higher overall injected particle mass (Fig. 21).

3. Partial Collapse regime

   (a) As jet strength increases within this regime (decreasing $-Ri_0$ for given ϕ; Fig. 8), the effective entrainment parameter increases from one that is approximately α_{ftn} to values similar to α_{pl}

(Fig. 14). A variable entrainment model underestimates the entrainment rate for monodisperse jets with buoyant interstitial fluid at the source, coarse particles in the range $4.5 \pm 2.0 < St_0 < 4.8 \pm 2.2$, $-Ri_0 < 1.8 \times 10^{-4}$ and $\phi_0 > 1.9 \times 10^{-2}$ (inset in Fig. 14). This same model overestimates the entrainment rate for monodisperse jets with fine particles in the range $0.3 \pm 0.2 < St_0 < 0.4 \pm 0.2$. The model underestimates the entrainment rate for a bidisperse jet with particles in the range $0.6 \pm 0.3 < St_0 < 4.0 \pm 1.9$

   (b) The average jet height is predicted by Eq. 7 with $C_{ftn} = 1.3$ for non-buoyant jets and $C_{ftn} = 0.7$ for jets with buoyant interstitial fluid (Fig. 15).

   (c) For steady-state coarse particle jets, the two dominant frequencies of periodic jet height oscillations overlap with the frequencies of large and small sediment waves, which are predicted by Eqs. 10 and 12 (Fig. 17; Table 4).

   (d) A well-defined power spectral slope is comparable to a classical Kolmogorov scaling between the source and overshoot fountain frequencies indicating that there is a continuous energy cascade from large to small sediment waves and that the predominant energy sink in this frequency range is by turbulent dissipation (right column in Fig. 17). For frequencies above the overshoot fountain frequency, the spectral slope is comparable to the Ozmidov scaling, indicating that the predominant energy sink in this frequency range is linked to mixing across density interfaces by the rising jet and descending sediment waves.

   (e) For strong coarse particle jets near the BP regime (Fig. 8), the velocity of sediment waves can decrease to the terminal settling velocity of

particles and sediment waves can disperse before reaching the tank base. For weaker coarse particle jets in the middle of the PC regime and near the TC regime, sediment wave speed stays above the terminal settling speed of the particles and descend to the tank base where they transform into gravity currents (Figs. 18 & 19).

Discussion: eruption column gravitational stability expressed through sediment wave dynamics, cloud structure and deposit architecture

Plinian eruptions often emerge in the BP regime, transition to the PC regime and end in the TC regime (Carey et al. 1988; Wilson 1993; Kaminski and Jaupart 2001; Hildreth and Fierstein 2012; Castruccio et al. 2016). To accurately reconstruct eruption column dynamics from remote sensing observations of umbrella cloud structures, time series of jet height oscillations and analyses of deposit architectures, it is necessary to understand the evolution of an eruption column from the BP to TC regime through a PC regime that spans a particularly large $-\text{Ri}_0$-ϕ parameter space for coarse- as well as fine-particle jets. Accordingly, we organize the next discussion in terms of five overarching themes:

1. Particle sedimentation within the enhanced settling annulus evolves continuously from predominantly individual particle settling to progressively more time-dependent and periodic sedimentation via small and large sediment waves from the BP→PC→TC regimes ("Links between the BP and TC regimes through the evolution of sediment waves in the PC regime: new conceptual models").
2. The character of jet height oscillations reflects dynamical contributions from the lower and overshoot fountain regions of an eruption column, which shift with eruption regime, and the response of the density stratification of the ambient fluid (cf. Eqs. 4, 10 and 12; "Links between source parameters and eruption regimes through sediment waves").
3. Coarse particles ($1 < \text{St}_0 < 10$) enhance entrainment into jets in the BP and PC regimes ("Effects of particle size, particle buoyancy and sediment waves on entrainment").
4. The negative buoyancy of coarse particles increases the likelihood that sediment wave mixtures reach the ground and, in turn, increase the likelihood for jet column collapse ("Effects of particle size, particle buoyancy and sediment waves on entrainment")
5. Transitions from BP → TC regimes are expressed through changes in the relative contributions of large

and small sediment waves (Fig. 17), which affect both the structure of resultant volcanic clouds ("Controls on ash cloud structure by sediment wave dynamics") and architectures of deposits ("Links between sediment wave dynamics and deposit architecture")

Following this discussion and bearing in mind the simplifications of our experiments compared to volcanic jets that involve, for example, complex effects related to interstitial fluid buoyancy ("Interstitial fluid buoyancy"), we compare predictions from our conceptual models to remote sensing observations and deposit analyses of several well-studied Plinian eruptions as case studies ("Case studies: Implications for observations of explosive eruption columns and their deposits"). A useful outcome is that our work identifies specific observations that require additional mechanics to those considered in this study, thereby defining a clear path of new research for future studies.

Links between the BP and TC regimes through the evolution of sediment waves in the PC regime: new conceptual models

To illustrate how these predictions are expressed in direct observations as well as deposits, we apply the results summarized in "Principal qualitative results: a summary" and "Principal quantitative results" to revise current well-established conceptual models of plinian eruption column regimes (Fig. 1). Specifically, this new view highlights the:

1. Sensitivity of eruptive regime to $-\text{Ri}_0 \leftrightarrow \phi_0$ conditions, depending on particle inertial effects modulated by the predominant particle size, which may evolve during an eruptive episode.
2. Increasing importance of descending sediment waves governing eruption column collapse with the smooth transition from the BP to PC to TC regimes (i.e. $-\text{Ri}_0$ and ϕ_0 increase smoothly).
3. Existence and structure of an enhanced settling annulus where the character of sediment waves exert a primary control on the architecture of the proximal deposit.

Guided by our experimental observations, we step through a plausible evolution of an eruption column as it transitions from the BP regime to the TC regime through a relatively extensive PC regime (Figs. 1 & 2). For this discussion, we assume that ϕ_0 remains constant and explore how changes in $-\text{Ri}_0$ govern eruption column regime transitions. Beginning in the BP regime, a typical monotonic decline in the excess pressure driving magma through a volcanic conduit and/or concomitant vent erosion can cause $-\text{Ri}_0$ to increase, driving an eruption towards a BP-PC regime transition (Fig. 8). Sediment waves descend farther below the umbrella cloud LNB within the enhanced settling annulus,

New Conceptual Models for Eruption Column Regimes
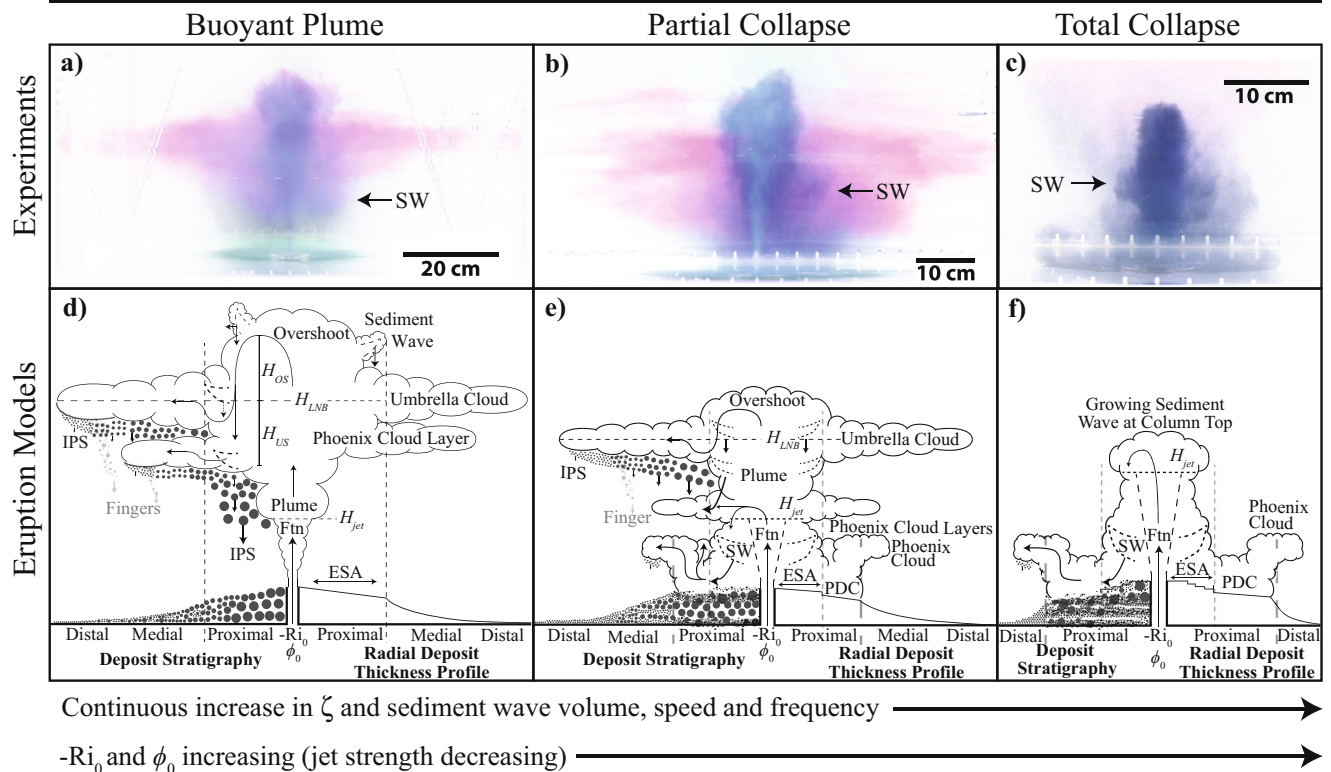
Fig. 22 Top panel: images of experimental jets in this study with steady source parameters and coarse particles, in the BP (a), PC (b) and TC (c) column regimes. All experiments show periodic sediment waves (black arrows) descending along the jet edge. Pink colors show spreading clouds for the BP and PC regimes. Gravity currents are shown spreading along the tank base for the TC regime. **Bottom panel**: new conceptual models of explosive eruption columns in the BP, PC and TC regimes. The size of sketched sediment waves (dotted outlines marked with "SW") increases from the BP to TC regime, reflecting an increase in sediment wave descent velocity and volume. The left side of each sketch shows the path of erupted mixture during ascent and descent, partitioning of erupted mixture into cloud layers or sediment waves, fingering or individual particle settling (IPS) sedimentation processes and the predicted deposit stratigraphy extending radially from the source (black triangles), which is labeled as the proximal, medial and distal sections of the deposit. The bottom right side shows the expected deposit thickness profile with increasing distance from the source. Arrows below figure show the change in sediment wave dynamics, $-Ri_0$ and ϕ_0 among the regimes. (d) Eruption column in the BP regime with H_{ftn} marking the transition from the "fountain"

to the "plume" region of the column. We do not specify the change in deposit thickness with distance outside the enhanced settling annulus. The variation in thickness depends on the relative contributions of sedimentation by fingers and individual particle settling, which can vary depending on the TGSD (see discussions in Carazzo and Jellinek 2012; 2013). **(e)** Eruption column in the PC regime. The fountain region (Ftn; e.g. Figs. 1g, 4 & 5b) is marked with diagonal dotted lines up to H_{ftn}. The enhanced settling annulus is bounded in the same way as for the BP regime, however, the proximal deposit in the PC regime extends to the farthest distance that a pyroclastic flow flows from the source region. The decline in deposit thickness with distance beyond the enhanced settling annulus is not to scale. It is exaggerated to show the overall change that is expected over distances much greater than the radius of the enhanced settling annulus. (f) Eruption column in the TC regime. The proximal deposit is defined in the same way that it is for the PC regime and there is only a distal deposit where relatively fine particles settle from phoenix cloud layers. Similar to e), the decline in deposit thickness with distance beyond the enhanced settling annulus is not to scale

dispersing before they reach Earth's surface (Fig. 22d). This process is expressed as tephra-gas mixtures undershooting to a lower height below the umbrella cloud (cf. Fig. 9 & Supplemental Video #1) and large amplitude oscillations (cf. Fig. 6 in Carazzo and Jellinek 2012). Whereas, larger particles with the highest inertia and terminal fall speeds settle individually from dispersing sediment waves, the remaining buoyant mixture rises and spreads

as phoenix cloud layers below the umbrella cloud. Under these transitional conditions, sediment wave-sediment wave interactions can cause sediment waves to merge and increase their downward momentum and buoyancy fluxes such that they descend to the ground to transform into pyroclastic flows. In contrast, sediment wave-phoenix cloud interactions can cause sediment waves to disperse higher in the atmosphere as positively buoyant phoenix cloud fluid

mixes with and increases the buoyancy of sediment wave interstitial fluid ("Qualitative observations: sediment waves, cloud intrusions and deposit architecture among regimes"; cf. Figs. 11 and 12).

As $-Ri_0$ increases to the parameter space well within the PC regime (Fig. 8), relatively high particle concentration sediment waves are larger in volume, descend around the eruption column at higher speed and transform into axisymmetric pyroclastic flows when they impact the ground, spreading out from the enhanced settling annulus (Fig. 22e). Effects of simultaneous partitioning of the tephra-gas mixture to buoyancy fluxes driving lateral cloud spreading and the vertical descent of sediment waves are expressed with multiple phoenix cloud layers spreading below the umbrella cloud and pyroclastic flows spreading from the eruption column base where sediment waves impact the ground. Sediment wave-sediment wave and sediment wave-phoenix cloud interactions occur with less frequency in the BP regime. In addition, phoenix clouds rising from pyroclastic flows can spread below or interact and merge with phoenix cloud layers spreading from dispersed sediment waves. Overall, ash clouds can spread at some or at all heights between the ground and the base of the umbrella cloud, producing a multiply layered ash cloud that is a characteristic feature of eruptions in the PC regime (Figs. 1b 22b and 26).

When $-Ri_0$ increases to the TC regime (Fig. 8), >90% of the erupted mixture volume collapses to form pyroclastic flows (Fig. 22f). This regime is characterized by relatively large volume and high particle concentration sediment waves that do not interact (analogous to panel d in Fig. 12). With impact at the ground sediment waves transform into axisymmetric pyroclastic flows with corresponding phoenix clouds ascending to spread into phoenix cloud layers.

We hypothesize that the reverse of this evolution, potentially in response to increasing volcanic gas fluxes or magma overpressures, is also a similarly continuous process: an eruption column in the TC regime becoming stronger and more gravitationally stable as $-Ri_0$ decreases and transitioning to the PC regime and then to the BP regime. In this scenario sediment waves become smaller in volume, less concentrated, descend at a slower velocity and increasingly produce non-axisymmetric pyroclastic flows (where they occur).

As a final comment in this part of the discussion, this evolution with increasing or decreasing $-Ri_0$ is deliberately simplified. The evolution can be complicated by, for example, abrupt changes in $-Ri_0$, ϕ_0 or St through transient shifts in source parameters and through re-entrainment of particles settling within the enhanced settling annulus (Veitch and Woods 2000).

Links between source parameters and eruption regimes through sediment waves

Observational constraints on the source parameters of explosive eruptions are typically limited to estimates of mass eruption rate on the basis of deposit mass and eruption duration or eruption column height (Mastin et al. 2009; Aubry et al. 2017b; Aubry et al. 2021). However, estimates of eruption source parameters independent of deposit mass, eruption duration and eruption column height are available for the 1980 eruption of Mt. St. Helens, which occurred in the PC regime (Carey and Haraldur 1985). Carey and Haraldur (1985) constrain the exit velocity to 200–330 m/s on the basis of pyroclast dispersal, Andrews and Gardner (2009) constrain the vent diameter between 25–37 m and the mixture bulk density to 2 kg/m^3, and combined with Jessop et al. (2016) conduit flow modeling, constrain the particle volume fraction exiting the vent to range between 1–22%. These estimates provide a range of volcanic jet strength between $O(10^{-3}) < -Ri_0 < O(10^{-1})$ demonstrating that the lower bound for $-Ri_0$ (i.e. maximum estimate of jet strength) and range of ϕ_0 places the 1980 eruption of Mt. St. Helens near the PC/TC regime boundary on Fig. 8, in agreement with direct observations from the field of simultaneous spreading of the umbrella cloud and PDCs, as well as observations of alternating air-fall and PDC layering in the proximal deposit (Criswell 1987; Carey et al. 1990).

If observations of ash cloud structure ("Controls on ash cloud structure by sediment wave dynamics") or inferences from deposit architecture ('Links between sediment wave dynamics and deposit architecture") indicate that an eruption is in the PC regime, these observations can independently constrain $-Ri_0$ to within one or two orders of magnitude, depending on estimates of ϕ_0 (Fig. 8; Carazzo and Jellinek 2012). Similarly, if these types of data indicate that the eruption is in the BP or TC regimes, this immediately bounds the minimum and maximum values of $-Ri_0$, respectively. Therefore, field observations of ash cloud structure and deposit architecture combined with Fig. 8 provide a useful new method for constraining eruption source parameters.

Consistency with previous studies: fountain dynamics govern periodic column collapse

Periodic oscillations of coarse- and fine-particle jet heights are related to the steady momentum and buoyancy fluxes of the jet mixture at the source and fluid LNB through Eqs. 10 and 12 (Table 4; Figs. 17 and 19). Our results in Fig. 17 show that the dominant frequency of periodic jet height oscillations is predicted with equation 10, in agreement with the classic fountain frequency scaling first proposed

by Turner ([1966](#)) and tested rigorously by Burridge and Hunt ([2013](#)) for the "forced" fountain regime ($-\mathrm{Ri}_0 < 0.5$). Neri and Dobran ([1994](#)) simulate collapsing eruption columns with $0.3 < -\mathrm{Ri}_0 < 6.8$, covering a range of fountain regimes from "very weak" to "forced", according to Burridge and Hunt ([2013](#)). For their simulation A2, with $-\mathrm{Ri}_0 = 1.7$ placing it in the "very weak" fountain regime (Burridge and Hunt [2013](#)), they report a range of dominant frequencies $0.02 < f < 0.06$ Hz of velocity oscillations at the top of the fountain (or jet) of the simulated eruption column (Figure [6](#)b in their study). The dominant frequency $f = 0.06$ Hz agrees with the predicted fountain frequency for very weak fountains, $f_{ftn} = 0.06$ Hz (Equation 3.23 in Burridge and Hunt, [2013](#)). Suzuki et al. ([2016](#)) observed periodic collapse of material from the fountain-plume transition height for two 3D numerical simulations of strong volcanic jets with source parameters near the BP-TC transition. Taken together, the results of Neri and Dobran ([1994](#)) and Suzuki et al. ([2016](#)) and this study, along with the fountain classification scheme presented in Burridge and Hunt ([2013](#)), strongly suggest that the collapse of eruption columns can be periodic and predicted if eruptive source parameters are known.

We extend the work of Neri and Dobran ([1994](#)) and Burridge and Hunt ([2013](#)) by applying an appropriate fountain scaling to the overshoot region of jets in the BP and PC regimes, consistent with our results in Fig. [17](#) and "Principal quantitative results".

For eruption columns in the TC regime, the mean top height of the eruption column, H_{ftn}, can be predicted with equation [7](#) (for example, see Fig. [15](#)) and will oscillate about this mean height at N and f_{ftn}, which can be predicted with Eqs. [4](#) and [10](#) (for example see bottom panel in Fig. [17](#) Turner [1966](#)). The growth and collapse of the top of the column is expressed through annular sediment waves collapsing periodically from H_{ftn} at f_{ftn} (Fig. [17](#)) which, in turn, generate axisymmetric gravity currents flowing radially from the base of the eruption column (Fig. [22](#)f). Oscillations of H_{ftn} at the fountain frequency f_{ftn} will be accompanied by oscillations in the jet radius r_{ftn} as sediment waves grow and collapse from this region. For example, although the jet column of the polydisperse experiment #43 (Fig. [13](#)) is occluded by gravity currents and phoenix clouds during steady-state, fluctuations in r_{ftn} correspond with the growth and collapse of large axisymmetric sediment waves (Supplemental Video [2](#)). Thus, real-time measurements of the eruption column top height and diameter provide two independent methods to measure f_{ftn} and, in turn, the frequency of column collapse leading to pyroclastic flows.

For eruption columns in the BP and PC regimes, fluctuations of H_{ftn}, consistent with equations [4](#) and [10](#), and H_{OS}, consistent with Eq. [12](#), will each contribute to eruption column top height fluctuations (Fig. [17](#)). A clue to which height fluctuation, H_{ftn} and H_{OS}, will contribute more to overall eruption column top height fluctuations is the ratio of the normalized power of f_{ftn} and f_{OS} in Fig. [17](#), defined as P_{ftn}/P_{OS}. For experiments in the BP regime $P_{ftn}/P_{OS} \approx 2.0$ and is similar for experiments in the PC regime with $P_{ftn}/P_{OS} \approx 4.0$, indicating that the contribution of fluctuations of H_{ftn}, arising from the BV-frequency N or source fountain frequency $f\,ftn$, contribute more than fluctuations of H_{OS}, arising from the overshoot fountain frequency $f\,OS$, to the overall power
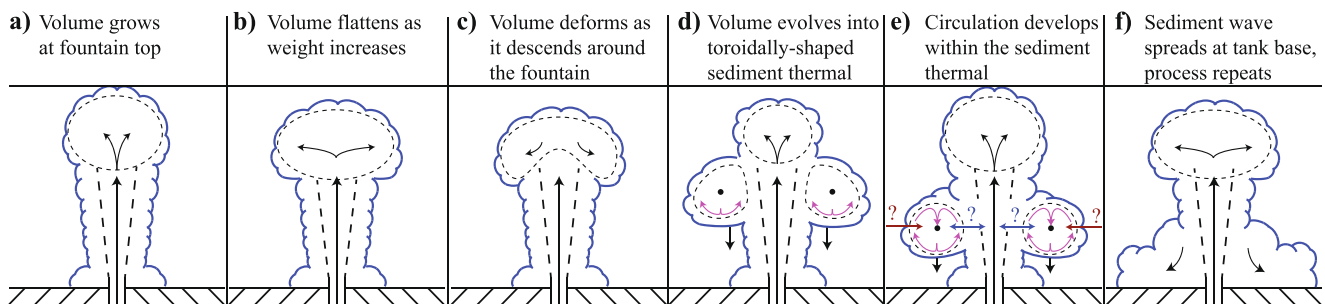
Fig. 23 Model sketches of the cycle of large sediment waves growing at the top and descending around multiphase jets in the TC regime. Blue outline marks visible boundary of multiphase flow, vertical dashed lines mark inner upward flow of the fountain, dashed circle marks sediment wave control volume and black arrows indicate flow of fountain mixture. (a) Sediment wave volume grows at top of fountain supplied by a steady volume flux. (b) Sediment wave volume at fountain top flattens due to the restoring buoyancy force of the ambient density stratification. (c) Downflows into growing sediment waves take material from the overshoot region, reducing overall jet height. (d) Descending sediment wave volume evolves into a toroidally shaped sediment thermal (Bush et al. 2003) descending around the fountain. Pink arrows indicate the onset of circulation within the sediment wave. The fountain height recovers and another sediment wave control volume begins to grow at the fountain top. (e) Circulation within the sediment wave develops in the form of two counter-rotating vortices with divergence and convergence zones at the base and top of the ring, respectively. Blue arrows and question marks indicate unknown exchange of mixture volume between descending sediment wave and upflowing fountain (cf. Bloomfield and Kerr 2000). Red arrows and question marks indicate unknown volume flux of ambient fluid into sediment wave. (f) Sediment wave descends to tank base to spread as a ground-hugging gravity current. The process repeats as the next growing sediment wave volume begins to flatten

of jet column top height fluctuations in the BP and PC regimes.

The largest overturning motions at the top of a jet are set by the diameter of the jet at this height (Fig. 23; Burridge and Hunt 2013). The sediment wave radius is defined as the lateral extent of a sediment wave from the jet boundary to its outermost part. We expect the sediment wave radius to be set by the average jet radius, r_{ftn} taken at H_{ftn} for large sediment waves descending next to jets in the PC and TC regimes and r_{LNB} taken at H_{LNB} for small sediment waves descending next to jets in the PC and BP regimes. Assuming sediment waves do not grow significantly during descent through entrainment, consistent with our experiments, we expect the outermost part of large and small sediment waves to impact the tank base within $1.5r_{ftn}$ and $1.5r_{LNB}$, respectively (Fig. 21; see "Links between sediment wave dynamics and deposit architecture" for further discussion).

The spectral slopes of multiphase jet height oscillations (right column of Fig. 17) provide insight into how mechanical energy delivered to multiphase jet columns is dissipated in each regime. For the BP and PC regimes, the maximum mechanical energy in the spectra enters at f_{ftn}, which induces a response of the tank stratification at the frequency N that sets the lowest frequency of jet height oscillations (a fundamental mode). In the BP regime 50% of the maximum mechanical energy enters at f_{OS}. In the PC regime, the response of the stratification generates turbulence at frequencies between N and f_{OS} and excites large and small sediment waves at these frequencies, respectively, with 25% of the maximum mechanical energy entering at f_{OS}. In both regimes at frequencies above f_{OS} mechanical energy is dissipated according to the Ozmidov -11/3 scaling, which indicates energy carried by sediment waves is consumed by molecular mixing across density interfaces.

Michaud-Dubuy et al. (2018) use experiments to investigate fine-particle jets with $2 \times 10^{-3} < -\text{Ri}_0 < 2.3 \times 10^{-2}$ and $10^{-3} < \phi_0 < 10^{-2}$. They find that the fountain mixture either collapses to the tank base or particles decouple from the fluid at the fountain top and settle individually while the fluid rises as a buoyant plume (Fig. 7 in their study). They propose a model for the growth and collapse of a spherical volume of mixture at the top of a multiphase fountain, which they use to predict the period of height oscillations (see equation 3.5 in their study) and recover the classic fountain frequency scaling (Eq. 10) with a constant of $F_{ftn} = 0.5$, which is consistent with that found previously for fountains in Burridge and Hunt (2013). For our relatively stronger and higher particle volume fraction multiphase jets in the TC regime, with $-\text{Ri}_0 \sim O(10^{-4})$ and $\phi_0 > 10^{-2}$, we find $F_{ftn} = 0.7$, which is in agreement with that found for the lowest $-\text{Ri}_0$ range of fountains in

Burridge and Hunt (2013, see their Figure 11). Whereas Mingotti and Woods (2016) introduce a conceptual model that implies asymmetric collapse of the fountain top mixture in a spherical volume (Fig. 7a in their study), we observe the collapse of jets in the TC regime in this study to be characterized by annular sediment waves (Figs. 10 & 23), indicating that the fountain top mixture predominantly collapses in the shape of a torus. We do observe small sediment waves that fall asymmetrically on either side of multiphase jets in all regimes that may be well described by the spherical geometry assumed by Mingotti and Woods (2016). The shape of the collapsing mixture is important in the context of pyroclastic flows where a toroidal shape would generate axisymmetric pyroclastic flows flowing radially from the eruption column base (Fig. 10) as opposed to a spherical shape that would generate pyroclastic flows flowing radially from one side or another of the column base. We discuss the implications of sediment wave shape for deposit architecture in "Links between sediment wave dynamics and deposit architecture".

On the basis of our quantitative results in Fig. 17 and Table 4, we expect the commonly referenced "boiling over regime (Rowley et al. 1981; Criswell 1987; Pacheco-Hoyos et al. 2018; Suñe-puchol et al. 2019) of eruptions in the TC regime space of Fig. 8 to be potentially characterized by f_{ftn} (Eq. 10). In the limit of weak and relatively concentrated eruptions, with low u_0 and large ϕ_0, we expect f_{ftn} to be sufficiently high such that the interval between column collapse events becomes small enough that mass fluxes delivered to PDCs can be considered effectively continuous. In the deposit close to or within the enhanced settling annulus, we expect PDCs generated in this regime to emplace massive deposit layers lacking clear flow boundaries in the stratigraphy. In the limit of strong and relatively dilute eruptions, we expect f_{ftn} to be sufficiently low such that column collapse events generate PDCs intermittently or periodically, rather than continuously. In this case, we expect deposit layers emplaced by intermittent or periodic PDCs to have identifiable flow boundaries in the stratigraphy. It is important to note that transport processes occurring within PDCs can lead to layering within the PDC deposit stratigraphy (Brown and Andrews 2015; Dufek et al. 2015) and it may not be possible to determine whether PDC deposit layering originates from transport processes, variations in eruption source parameters or episodic column collapse. In addition, whether Eq. 10 can be reliably used to discriminate between intermittent or periodic column collapse versus boiling over requires further investigation of the applicability of this equation to fountain mixtures with more varied particle size distributions than those investigated in this study and a careful comparison of inferred eruption source parameters with inferred PDC intervals from deposit stratigraphy (e.g.

"Climactic eruption of Mount Pinatubo (1991): gradual BP→PC→TC evolution" & "Quilotoa, Ecuador, 0.8 ka: evolution of pyroclastic flows through the PC regime"; Rosi et al. 2001; Di Muro et al. 2008).

Effects of particle size, particle buoyancy and sediment waves on entrainment

We now turn to the effects of particle size (i.e. St #) on entrainment of ambient fluid into the jet column. Previous studies estimating entrainment into fountains investigate a range of $-\mathrm{Ri}_0 > 10^{-1}$, significantly larger than the $-\mathrm{Ri}_0 < 10^{-3}$ conditions we explore (Baines et al. 1990; Lin and Armfield 2004; Bloomfield and Kerr 2000; Carazzo et al. 2010). Figure 14 shows that the best-fitting effective entrainment parameter for our results is a function of $-\mathrm{Ri}_0$. A variable entrainment model (Appendix B; Kaminski et al. 2005; Carazzo et al. 2006) underestimates the rate of entrainment for monodisperse coarse ($3.8 < \mathrm{St}_0 < 6$) and a fine particle ($\mathrm{St}_0 \approx 0.5$) jet, as well as bidisperse jets ($10^{-1} < \mathrm{St}_0 < 10$), all with $-\mathrm{Ri}_0 < 1.8 \times 10^{-4}$ (inset in Fig. 14). In contrast, for two fine particle jets with $0.3 < \mathrm{St}_0 < 0.4$ and $-\mathrm{Ri}_0 > 2.3 \times 10^{-4}$ the variable entrainment model overestimates the rate of entrainment.

These results are broadly consistent with those from experiments on analog particle-laden jets in Jessop and Jellinek (2014) and also on grid-stirred turbulent entrainment and mixing in Lherm and Jellinek (2019) and supports the hypothesis that inertial particles with St $\sim$ 1 can enhance entrainment whereas particles with St < 1 can inhibit entrainment. With enhanced entrainment the density of our coarse-particle jets will evolve towards the density of the ambient fluid over a shorter height of rise than particle-free cases. This expectation predicts that inertial particles should help to stabilize multiphase jet columns in the BP regime. However, we find that the boundary between the BP and PC regime for coarse particle jets occurs at a $-\mathrm{Ri}_0$ approximately one order of magnitude lower than is the case for fine particle jets in Carazzo and Jellinek (2012; Fig. 24a-b). Therefore, although entrainment is enhanced, the net effect of the presence of inertial particles is to favor jet collapse.

Clues to the dependence on median particle size for the gravitational stability of multiphase jets include additional mixture buoyancy effects that are potentially enhanced compared to Carazzo and Jellinek (2012) through larger particle sizes for given particle concentrations ϕ_0. To capture the potential effects of median particle size on turbulent entrainment of ambient fluid into the jet and on gravitational stability we introduce a "jet stability number"

$$\Lambda_0 = -\mathrm{Ri}_0 \frac{\tau_{p,0}}{\tau_{s,0}} = \frac{g_0' r_0}{u_0^2} \left(\frac{\rho_p d_p^2}{18 f \mu_f} \right) \left(\frac{u_p}{r_0} \right) \quad (16)$$

where u_p is the settling velocity of the median particle size. Defined in this way, the jet stability number captures the effects of particle-fluid coupling on turbulent entrainment and on mixture buoyancy by modifying the source Richardson number with the ratio of the particle response time to fluid accelerations $\tau_{p,0}$ to the particle settling time $\tau_{s,0}$ through an eddy just above the source with radius r_0. Where $\tau_s < \tau_p$, particle settling is fast compared to eddy turnover time and the effective $-\mathrm{Ri}_0$ increases driving the jet towards the TC regime. Where $\tau_s \sim \tau_p$, particles remain in suspension and coupled to entraining eddies and $-\mathrm{Ri}_0$ is unchanged. Where $\tau_s > \tau_p$, particle inertial effects modify eddies near the jet source and enhance entrainment (cf. Jessop and Jellinek 2014; Lherm and Jellinek 2019), the effective $-\mathrm{Ri}_0$ decreases and jets evolve towards the BP regime. When cast in the parameter space of the jet stability number and particle volume fraction, multiphase jets in (Carazzo and Jellinek 2012) and this study consistently occur in the PC regime for $3 \times 10^{-7} < \Lambda_0 < 4 \times 10^{-5}$ and $7 \times 10^{-3} < \phi_0 < 6 \times 10^{-2}$ despite varying particle size distributions (Fig. 24c).
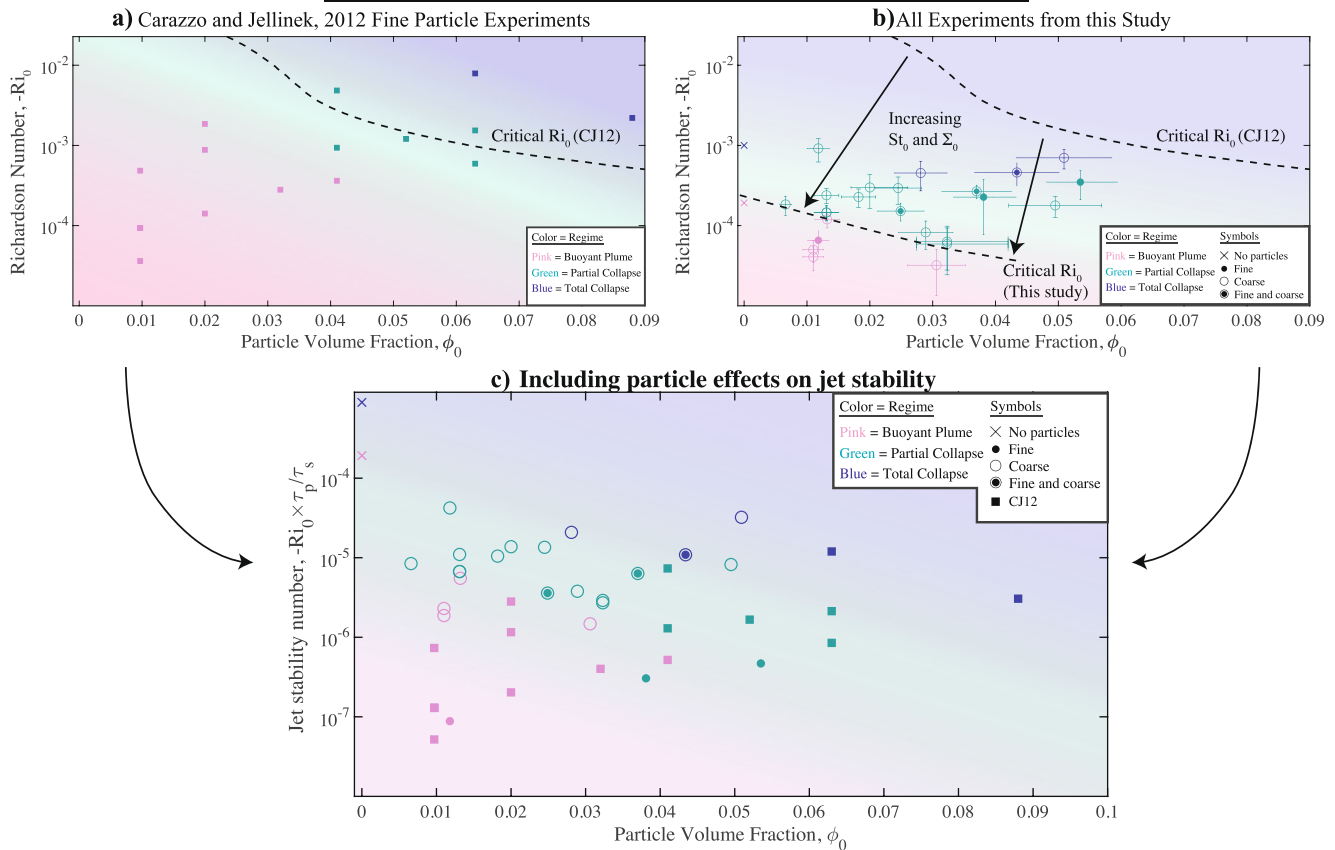
More generally, however, these comparisons must be carried out with caution. Although they are conducted with comparable stratification strengths, the Carazzo and Jellinek (2012) experiments as well as those by Jessop and Jellinek (2014) are carried out in a two-layer system with a stepwise rather than linear density gradient. Because the local -Ri conditions governing mixing and sedimentation at each level of jet rise are distinct in these two setups, predictions for both the influence of inertial particles on the effective entrainment parameter and for the precise conditions for a BP will differ in quantitative detail. Nonetheless, we suggest future studies investigate whether jets occurring near the BP/PC regime transition in $\Lambda_0 \leftrightarrow \phi_0$ space undergo late collapse at times beyond the duration of experiments conducted in Carazzo and Jellinek (2012) and this study.

Controls on ash cloud structure by sediment wave dynamics

Insights into and inferences from cloud structure

The structures of clouds spreading from the multiphase jets in this study are an expression of the underlying jet column regime (Figs. 1, 11 and panel c in Fig. 12). For jets with relatively low $-\mathrm{Ri}_0$ and ϕ_0 in the BP regime near the BP-PC regime transition (Fig. 8), the majority of the mixture volume descending from the overshoot region spreads laterally at a level of neutral buoyancy as an umbrella cloud. A relatively small fraction of the mixture buoyancy flux from the overshoot region is also carried by small asymmetric sediment waves below the umbrella

Influence of Particle Size on Source Conditions Favouring Collapse

a) Carazzo and Jellinek, 2012 Fine Particle Experiments

b) All Experiments from this Study

c) Including particle effects on jet stability

Fig. 24 $-Ri_0 \leftrightarrow \phi_0$ regime diagrams from Carazzo and Jellinek (2012) (a) and this study (b). Dotted lines show boundary between BP regime and collapsing regimes, which was determined with a 1D integral model in Carazzo and Jellinek (2012). Black arrows show qualitative change in boundary due to presence of inertial particles in jet mixtures from this study. (c) A modified multiphase jet regime diagram where the source Richardson number is multiplied by the source Stokes and Sedimentation number of the median particle size to form a "jet stability" number Λ_0 (Eq. 16). The jet stability number accounts for particle-fluid coupling and buoyancy effects on entrainment and the gravitational stability of jets, respectively

cloud (Fig. 11a and BP column of panel c in Fig. 12). The height of the overshoot region sets the gravitational potential energy that is released through the periodic descent of small sediment waves that overshoot the LNB into the undershoot region as momentum-driven fountains. These downflows are akin to those feeding the growth of gravitationally unstable particle boundary layers at umbrella cloud bases in Carazzo and Jellinek (2012) (their Figure 6). A critical difference to this earlier work is that this process occurs in a linear density gradient. As these periodic features descend, spread and mix with the ambient fluid density, buoyant interstitial fluid from the overshoot region detrains as rising phoenix clouds that spread and mix with ambient layers more dense than those at the umbrella cloud LNB to form phoenix cloud layers beneath the umbrella cloud. This process is apparent in experiment #52, where small sediment waves descend to heights below the umbrella cloud where they disperse. In particular, 32 s into the experiment, a phoenix cloud layer begins spreading below

the umbrella cloud (Supplemental Video 4 and BP column of panel c in Fig. 12). Although they may occur in concert, these are distinct processes from the production of internal cloud layering through the excitation of internal waves and diffusive particle convection, which can occur for very low $-Ri_0$ (Carazzo and Jellinek 2013), but may be similar to the processes driving multiple cloud layer spreading in Van Eaton et al. (2012).

Oscillations of the cloud base driven by flows from the overshoot region across the LNB to gravitationally unstable particle boundary layers forming at cloud bases are features of multiphase jets in the BP regime and can give rise to mammatus as well as to so-called "late collapse" events, where they grow to be very large in amplitude (Carazzo and Jellinek 2012). Undershooting eruption mixtures are also apparent in images of the 2011 eruption of Puyehue Cordon-Caulle, Chile (Fig. 25a). In the presence of a linear density gradient in the ambient, experiment #49 shows that for a jet initially occurring in the BP regime,
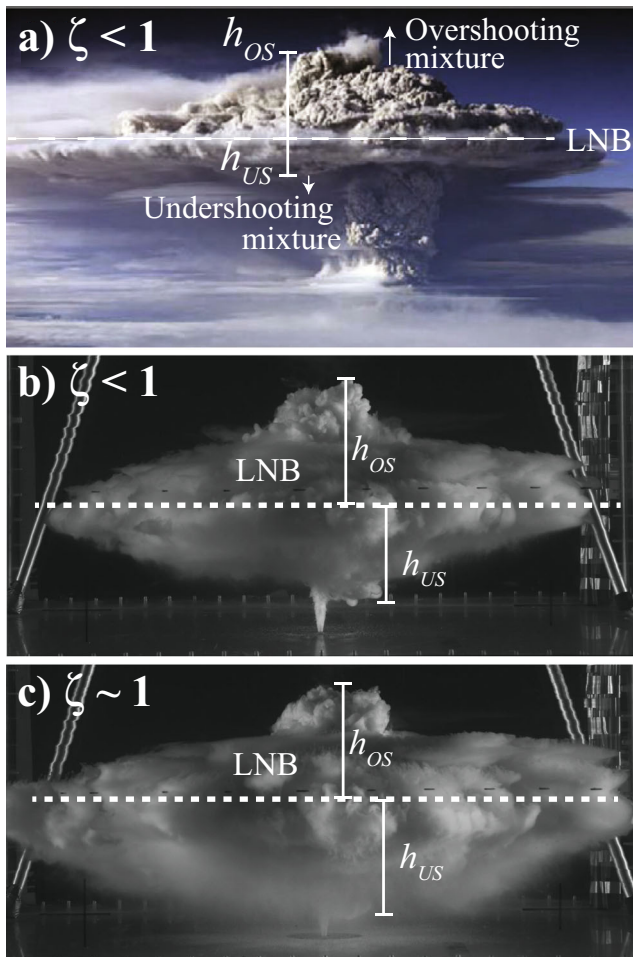
Fig. 25 (a) Eruption column and umbrella cloud during the eruption of Puyehue Volcano, Chile, 2011. The overshoot region is visible above the umbrella cloud and marked h_{OS} whereas undershooting tephra-gas mixture is visible below the umbrella cloud and marked h_{US}. The LNB is marked with a dotted white line, however all marked length scales are qualitative and not to scale. Reprinted from Carey and Bursik (2015) with permission from Elsevier. (b) Image taken 25.8 s into experiment #49 before a late partial column collapse occurs. White bars mark h_{OS} and h_{US} and the Collapse # (ζ) is less than one. (c) Image taken 41 s into the same experiment where the Collapse # is approaching unity. Late collapse occurs $\approx$12 s later

undershooting mixtures can reach lower heights next to the jet column over time and drive a transition from the BP to the PC regime (Supplemental Video 1). From this observation we infer a positive feedback cycle as follows: 1) Undershooting mixtures, which are more dense than the ambient fluid, are re-entrained into the upper regions of the sustained jet column; 2) The bulk density of the jet mixture as it passes the LNB is increased, compared to jet mixtures injected before undershoots are re-entrained, and the jet overshoot and mixture LNB heights are reduced; 3) Subsequent undershooting mixtures progressively reach lower heights next to the jet column; 4) The process repeats until undershooting mixtures reach the tank base. In this

scenario, undershooting mixtures are considered sediment waves, however, particle-free jets can exhibit this same behavior as particles are not required to drive undershoots of jet fluid as it spreads into an umbrella cloud, hence our use of the more general term "undershoots" to describe this process which applies to single or multiphase jets.

On the basis of observations of h_{US} increasing over time during experiments #49 and #50 ("Effects of particle size, particle buoyancy and sediment waves on entrainment"; Supplemental Video 1) and the undershoot positive feedback cycle driving jet columns towards collapse, we propose that the ratio of overshoot to undershoot heights, which reflects the partitioning of buoyancy flux from the overshoot region to lateral spreading and vertical motions provides a useful and intuitive metric for determining the stability of the plume region of an eruption column with source parameters near the BP-PC regime transition or in the PC regime (Fig. 8). We define this eruption column stability metric as the "Collapse Number"

$$\zeta = \frac{h_{US}}{h_{OS}}. \tag{17}$$

Here $\zeta < 1$ corresponds to a condition where the overshoot height is relatively large and the majority of the buoyancy flux from the overshoot region spreads laterally to drive the spread of an umbrella cloud (BP column in panel a in Fig. 12). This condition marks a stable umbrella cloud. By contrast, where $\zeta \geq 1$, the undershoot height is relatively large and a greater fraction of the buoyancy flux from the overshoot region is carried below the LNB to excite large sediment waves. This condition marks an unstable umbrella cloud and is indicative of potential eruption column collapse. This picture is consistent with the large amplitude undershoot conditions identified to lead to late collapse events in Carazzo and Jellinek (2012) and it is likely that this regime is an expression of a PC regime in the absence of a linear density gradient in the ambient fluid layer. This potential dynamical similarity with Carazzo and Jellinek (2012) suggests that Eq. 17 can be related to the source conditions through a model akin to Appendix B. However, developing and testing this hypothesis is not trivial and beyond the scope of this study. Of significant and practical use, the value of ζ is readily estimated with satellite and ground-based remote sensing observations and can serve as a method to monitor the stability of an eruption column in real-time.

Within the PC regime, phoenix clouds rise from descending sediment waves that completely or partially disperse during their descent, as well as from gravity currents flowing along the tank base (Fig. 11b and PC column of panel c in Fig. 12). In addition, intermittent sediment wave-sediment wave interactions and sediment wave-phoenix cloud interactions can lead to phoenix cloud intrusions at
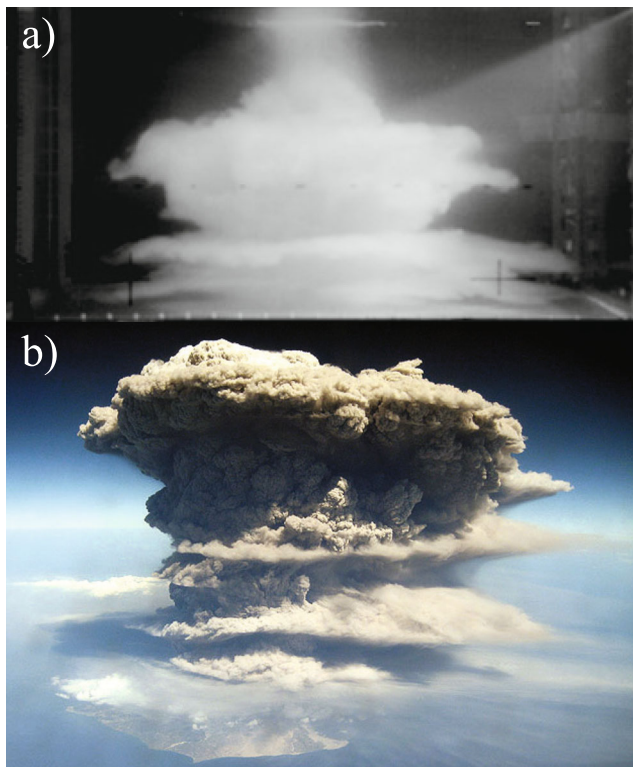
Fig. 26 (a) Image taken 40 s into experiment #14 in which a multiply layered particle cloud spreads from a polydisperse jet in the PC regime. (b) Image of a multiply layered ash cloud spreading from the eruption of Soufriere Hills Volcano, Montserrat (2010); from Wadge et al. 2014, Figure 1.28

many heights between the base of the umbrella and the tank (panels d and e in PC column of Fig. 12). Taken together, these sediment wave processes drive the formation of multiply layered clouds and are a distinctive feature of multiphase jets in the PC regime (Fig. 26, cf. Van Eaton et al. 2012).

Figure 26 shows a striking resemblance between the multiply layered particle cloud spreading from a multiphase jet in the PC regime and the multiply layered ash cloud spreading from the 2010 eruption of Soufriere Hills Volcano, Montserrat (Wadge et al. 2014). Our experiments suggest that the multiply layered ash cloud produced by this eruption is fed by an eruption column in the PC regime (Figs. 11 and 12). Moreover, the source parameters of this eruption column are not required to be unsteady, which is the conventional view. Our experiments demonstrate that steady source parameters can produce a multiply layered ash cloud. As a final remark here, Fig. 13 demonstrates that, when fine particles are present, descending sediment waves may be veiled by phoenix clouds rising and spreading around a multiphase jet column in the TC regime (see also Figure 11 in Carey et al. 1988). However, our analyses of height oscillations shows that the occurrence of sediment waves can be inferred from time series of the cloud height.

For coarse-, fine-, and bidisperse-particle jets in the TC regime > 90% of the mixture collapses as periodic sediment waves, carrying buoyant interstitial jet fluid to the tank base to form particle-driven gravity currents. As solid particles settle and compact during flow along the tank base, interstitial fluid rises as phoenix clouds that mix with the ambient stratification to collectively spread to form a single phoenix cloud layer (Fig. 12b). Sediment wave-sediment wave and sediment wave-phoenix cloud interactions do not occur in this regime (Fig. 12d–e). Significantly, the lack of sediment wave-sediment wave and sediment wave-phoenix cloud interactions may explain why intermittently rising phoenix clouds carry a similar buoyancy flux, consistent with the formation of a single cloud layer.

Although our results provide a promising diagnostic of eruptions in the TC regime, the dynamics of natural pyroclastic flows are more complicated than the gravity currents flowing along the tank base in our experiments and, thus, our predicted single cloud structure must be viewed cautiously. In particular, the distribution and magnitude of the buoyancy flux carried by intermittent phoenix clouds can be affected by various processes not captured by our experiments, including locally varying gas compressibility and fluidization (Roche et al. 2016), erosion of the substrate over which pyroclastic flows propagate (Roche et al. 2013) and time- and spatially varying processes governing the deposition of the suspended particle load over potentially complex topography (Dufek and Berganz 2007). Resultant variations in the buoyancy fluxes released to drive phoenix clouds, which can also impact the character of their mixing with the ambient atmosphere can lead to phoenix cloud layers spreading at various LNB heights.

Links between sediment wave dynamics and deposit architecture

A key new observation from this study are the terraced deposits that characterize the proximal deposit architecture emplaced by jets with coarse particles in the PC and TC regimes (Figs. 13, 21 and 22e–f). Figure 21 shows that the radius of the outermost terrace of any experiment is always within 1.5 jet diameters. The jet diameter, taken at H_{LNB} for jets in the PC regime and at H_{ftn} for jets in the TC regime, sets the maximum lateral length scale of any flow structure developing in this region of the jet. Therefore, we expect the radial extent of large annular sediment waves to be proportional to this length scale, which is consistent with our observations of their periodic descent within the enhanced settling annulus and their impact with the tank base within 1.5 jet diameters from the source (Figs. 20, 21 and 22). Further evidence for the formation of terraces upon impact of sediment waves with the tank base can be seen in Fig. 28 in which a top view of the first sediment

wave impacting the tank base is shown for a coarse particle mixture injected through an annular nozzle forming a jet in the TC regime. In Fig. 28d, the outermost terrace is within the radius of the first sediment wave as it impacts the tank base (Fig. 28a). On the basis of jet radius at H_{LNB} (PC) or H_{ftn} (TC) setting sediment wave radius combined with the observations of the experiment in Fig. 28, we conclude that each terrace is the result of coarse particles settling rapidly during impact of a large sediment wave with the tank base. Outward flow of particle-driven gravity currents may erode or augment the deposit topography as particles settle onto this terraced structure. However, Fig. 21 implies that the essential periodic terracing is preserved.

Predictions for the particle volume fraction of pyroclastic flows spreading around volcanic jets in the PC and TC regimes, and therefore the characteristics of the deposits they emplace, are informed by our entrainment rate results (Fig. 14), new conceptual models of eruption regimes (Fig. 22) and discussion in "Effects of particle size, particle buoyancy and sediment waves on entrainment". Jets in the PC regime (Fig. 8) have a higher rate of entrainment (Fig. 14) and higher top height (Fig. 15) than those in the TC regime. It follows that jets in the PC regime will entrain and mix with more ambient fluid cumulatively over their rise height than those in the TC regime.

For volcanic jets in the PC and TC regime with similar ϕ_0 (cf. exps. #35, 36 & 46 with #27 in Table 2; Figs. 14 & 19b) we expect sediment waves descending next to volcanic jets in the PC regime to be more dilute and colder in temperature than sediment waves descending next to volcanic jets in the TC regime. In turn, gravity currents spreading from sediment waves impacting the ground will be more dilute and colder around volcanic jets in the PC regime than gravity currents spreading around volcanic jets in the TC regime. During the eruption of Soufriere volcano, St. Vincent (April 1979), Carey et al. (1988) observed dilute gravity currents originating from high up in the explosive eruption column. They note that "People who were overrun by the flow reported no sensations of high temperature, and there was no destruction associated with their passage." These observations are in agreement with our conceptual model of an eruption column in the PC regime (Figs. 22e & 27a) in which the source of spreading gravity currents is linked to sediment waves descending from H_{ftn} or H_{LNB}. This model where the source of pyroclastic flows is located relatively high in the eruption column is in stark contrast with the "boiling over" model in which pyroclastic flows are generated by the erupted mixture pouring over the sides of the volcanic vent (Rowley et al. 1981; Criswell 1987; Pacheco-Hoyos et al. 2018; Suñe-puchol et al. 2019).

Our conceptual models for the PC and TC regimes make predictions for the componentry of the pyroclastic flow deposits within the enhanced settling annulus. Sediment waves descending from H_{ftn} (Fig. 22e) for a volcanic jet in the PC regime will not carry the entire erupted mixture, resulting in a partitioning of erupted mass between collapsing sediment waves and umbrella cloud spreading (Neri and Dobran 1994; Neri et al. 2002; Kaminski et al. 2011). When this behavior occurs, we expect the coarser fraction of the jet mixture PSD to be carried by collapsing sediment waves while the finer fraction is preferentially carried into the umbrella cloud (Eq. 14). Consequently, within the enhanced settling annulus, deposit layers linked to pyroclastic flows should be relatively fines-depleted and associated with pyroclastic surge layers emplaced by relatively dilute pyroclastic surges spreading out of the enhanced settling annulus, the latter of which is in agreement with the observations of dilute gravity currents during the eruption of Soufriere volcano, St. Vincent (1979; Carey et al. 1988). In contrast, for a volcanic jet in the TC regime the entire erupted mixture will be carried by collapsing sediment waves and deposit layers within the enhanced settling annulus linked to pyroclastic flows should not be relatively fines-depleted. Therefore, for a volcanic jet evolving from the PC to TC regime, deposit layers within the enhanced settling annulus and lower in the deposit stratigraphy should be relatively fines-depleted compared to those higher in the deposit stratigraphy.

An important consideration when comparing the architectures of experimental deposits in this study to those of natural deposits is that the experimental deposits are emplaced on a flat tank base whereas natural deposits are often emplaced on uneven terrain. For natural eruptions in the PC regime near the TC regime transition and those in the TC regime (Fig. 8), and in particular CCF eruptions (see "Introduction"; Jessop et al. 2016), we expect deposits within the enhanced settling annulus to exhibit a terracing topography if they are emplaced on slopes below the angle of repose of the tephra mixture carried by sediment waves. For deposits within the enhanced settling annulus with slope angles greater than the angle of repose of the tephra comprising the deposit, terrace topography may be buried by a tephra cone (Figs. 21b and 28d). In this case, buried terraces may only be revealed with seismic surveys (Tani et al. 2008; Pope et al. 2018; Tsampouraki-Kraounaki and Dimitris 2018) or other remote sensing methods. However, for sediment waves impacting slopes with an angle much higher than the angle of repose of the tephra comprising the sediment wave terrace formation may be inhibited.

All annular nozzle experiments with coarse particles in Jessop et al. (2016) emplaced terraced deposits (Fig. 28b and 29c). Taken together with the results in Figs. 1, 4 and 7 and Table 2 in Jessop et al. (2016), which suggest caldera eruptions are more likely to undergo column collapse, and with our results, we predict fountain dynamics (Eqs. 7 & 10) to govern the behavior of CCF eruption
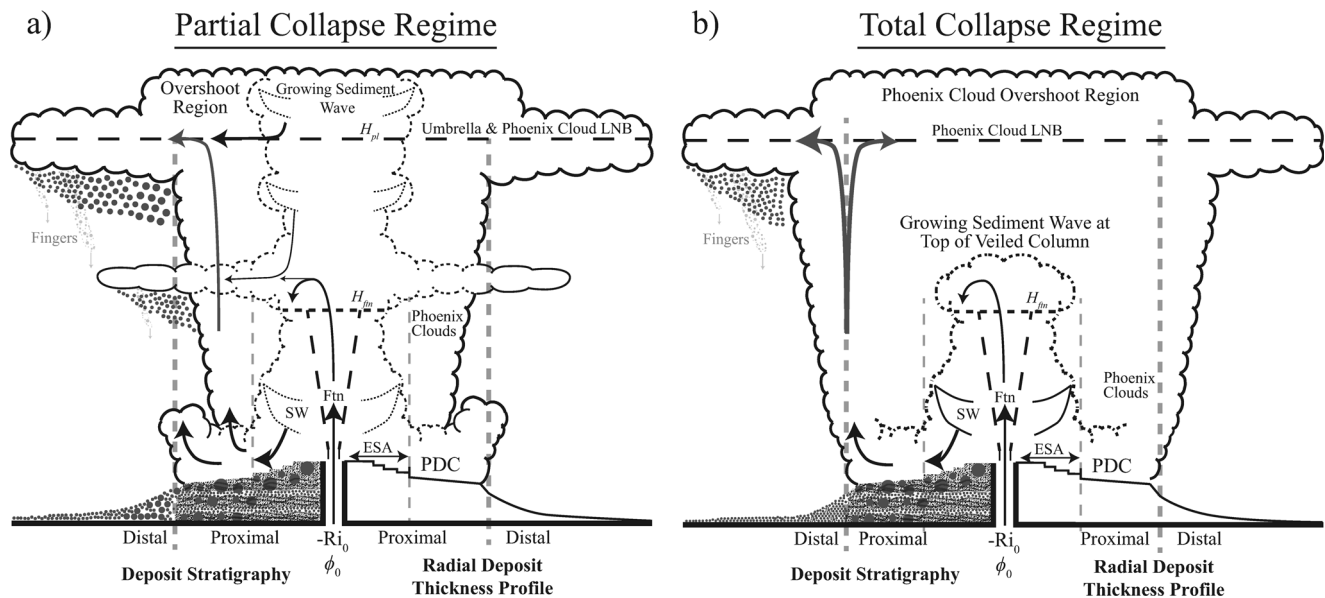
Fig. 27 (a) Compared to the conceptual model sketches in Fig. 22e–f, we present alternative conceptual model sketches for an eruption in the PC regime, with statistically stationary source parameters $-Ri_0 \leftrightarrow \phi_0$, (cf. Figs. 22e & 26) where phoenix clouds rise to a similar LNB as the spreading umbrella cloud. In this case, phoenix clouds completely veil the volcanic jet. (b) Alternative conceptual model sketch for an eruption in the TC regime (cf. Fig. 22f) where phoenix clouds rise higher

than the top of the veiled collapsing volcanic jet. Both of these models are constrained by the experimental results of this study, Fig. 26, and the observations on June 15, 1991, at 01:41 and 06:00–06:34 (PDT) of a co-ignimbrite eruption column (i.e. phoenix clouds) forming an oblate overshoot region above the umbrella cloud of the 1991 Pinatubo eruption (see Figures 3 & 4 in Holasek et al. 1996)

columns and that, in turn, proximal deposit terracing will be a characteristic feature of these eruptions. Distinct quasi-axisymmetric terracing is, for example, a well-described feature of a number of submarine deposits associated with CCF eruptions (Wright et al. 2006; Tani et al. 2008; Nomikou et al. 2012; Tsampouraki-Kraounaki and Dimitris 2018; Pope et al. 2018; Hooft et al. 2019). The largest terrace features in the proximal deposits around Santorini, Sumisu and MaCauley calderas are concentric terraces (Fig. 29). The surface of the deposits around Sumisu and MaCauley calderas are composed of unconsolidated tephra and Smith et al. (2003) identify >30 PDC units in the subaerial portion of the MaCauley deposit (Sandy Bay Tephra), indicating that the PDC flows that emplaced the surrounding submarine terraces could have been intermittent or periodic. We propose that these large-scale concentric terraces were emplaced by large axisymmetric sediment waves descending intermittently or periodically around explosive eruption columns in the PC or TC regimes. We expect terraced deposits to be better preserved and more common in submarine environments as opposed to subaerial environments where post-eruptive erosional processes modify eruption deposits within days after emplacement (Brown and Andrews 2015).
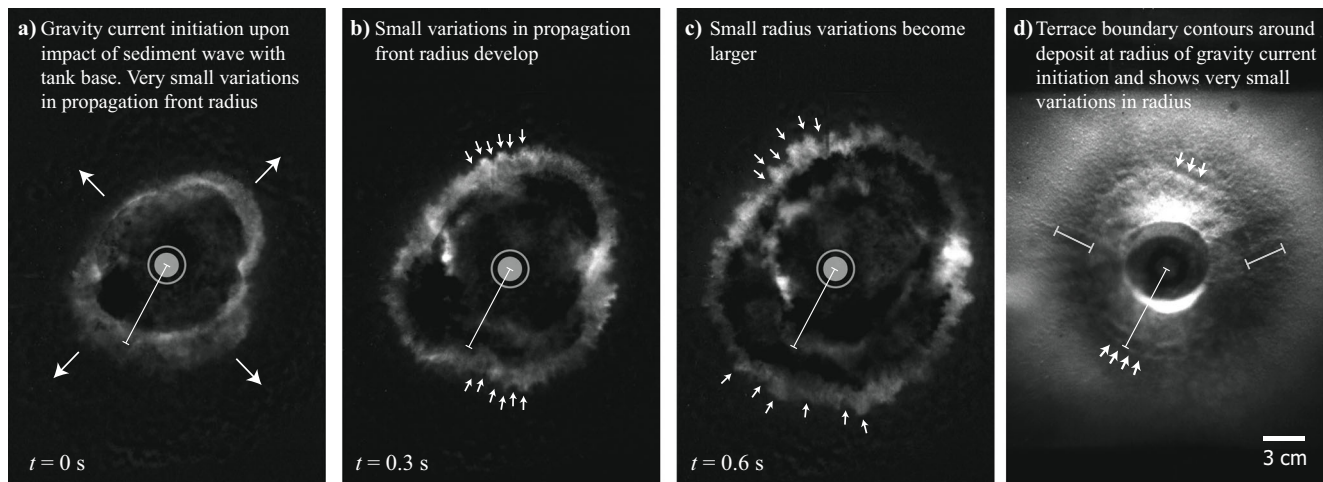
The terracing evident in bathymetry for Santorini and Sumisu (Fig. 29a and 29c) is notably broader than would be expected on the basis of the width of the enhanced settling

annulus even for annular vents (cf. Jessop et al. 2016). For volcanic jets erupted through "shallow" water layers with a depth $\leq H_{ftn}$ (Eq. 7), interactions with the sharp water-atmosphere density interface forming the free surface will affect the descent of sediment waves. In particular, we expect descending sediment waves to impact and spread at the free surface as jets or turbulent gravity currents (cf. Kotsovinos 2000) before descending through the water layer. This relatively larger diameter buoyancy source and effects of entrainment within the water column are likely to produce relatively broader terraces. This process along with additional interactions of overshoots of large sediment waves across the free surface with the seafloor are the focus of an ongoing investigation. We include this restricted discussion here to make clear the limits of the quantitative predictions from the results in "Quantitative results: links between source parameters and sediment wave dynamics".

Case studies: Implications for observations of explosive eruption columns and their deposits

Our conceptual models (Figs. 22 & 27) provide new insights into the processes governing the partitioning of erupted mass between umbrella and phoenix clouds spreading in the atmosphere and that which is carried to the ground by sediment waves. We make the following predictions for the mean and time-varying cloud

Top View of Experiment Simulating Caldera Eruption

a) Gravity current initiation upon impact of sediment wave with tank base. Very small variations in propagation front radius

t = 0 s

b) Small variations in propagation front radius develop

t = 0.3 s

c) Small radius variations become larger

t = 0.6 s

d) Terrace boundary contours around deposit at radius of gravity current initiation and shows very small variations in radius

3 cm

Fig. 28 Top view of gravity currents spreading axisymetrically from the base of a jet injected through an annular nozzle and occurring in the TC regime. (a) Propagation of gravity currents just after impact of sediment wave with the tank base. White arrows indicate propagation direction of gravity current fronts and white bar marks the radius of the enhanced settling annulus. Note the relatively smooth front of the spreading gravity currents. (b) As gravity currents spread, white arrows point to the development of small-scale variations in the radius of the gravity current propagation fronts from the vent. (c) Variations in the radius of the gravity current fronts become larger, implying lateral variations in propagation front velocities of gravity currents as they spread outside of the enhanced settling annulus. (d) Resulting terraced deposit from this experiment with white arrows marking small-scale variations in terrace radius from the vent. White bars highlight linear features extending radially from the vent that may be linked to lateral velocity variations in the gravity current propagation fronts highlighted in (b) and (c)

structure, deposit architecture and deposit texture in each regime:

1. **Buoyant Plume regime:** Volcanic jets with $-\text{Ri}_0 < 2.2 \times 10^{-4}$ and $\phi_0 < 3.5 \times 10^{-2}$ (Fig. 8)

   (a) Periodic oscillations of the volcanic jet top height are a superposition of oscillations of the fountain-plume transition height, H_{ftn}, the response of the density stratification of the ambient fluid N and the overshoot fountain height, H_{OS} (Figs. 4 & 17).

      (i) If N is known and H_{ftn}, H_{OS}, f_{ftn} and f_{OS} can be estimated from volcanic jet top height time series, then the momentum and buoyancy fluxes at the source and at the umbrella cloud LNB can be inferred (Eqs. 7, 11, 10 & 12).

   (b) Periodic oscillations of the overshoot fountain height H_{OS} are linked to relatively small volume non-axisymmetric sediment waves that can undershoot below the umbrella cloud and disperse before reaching the ground (Figs. 9, 11 & 12).

      (i) Dispersing sediment waves can lead to intermittent fallout of particles within the enhanced settling annulus and in turn, to discrete fallout layers that are laterally discontinuous.

      (ii) Buoyant interstitial fluid spreading from dispersing sediment waves can produce internal layering within the umbrella cloud or phoenix cloud layers below.
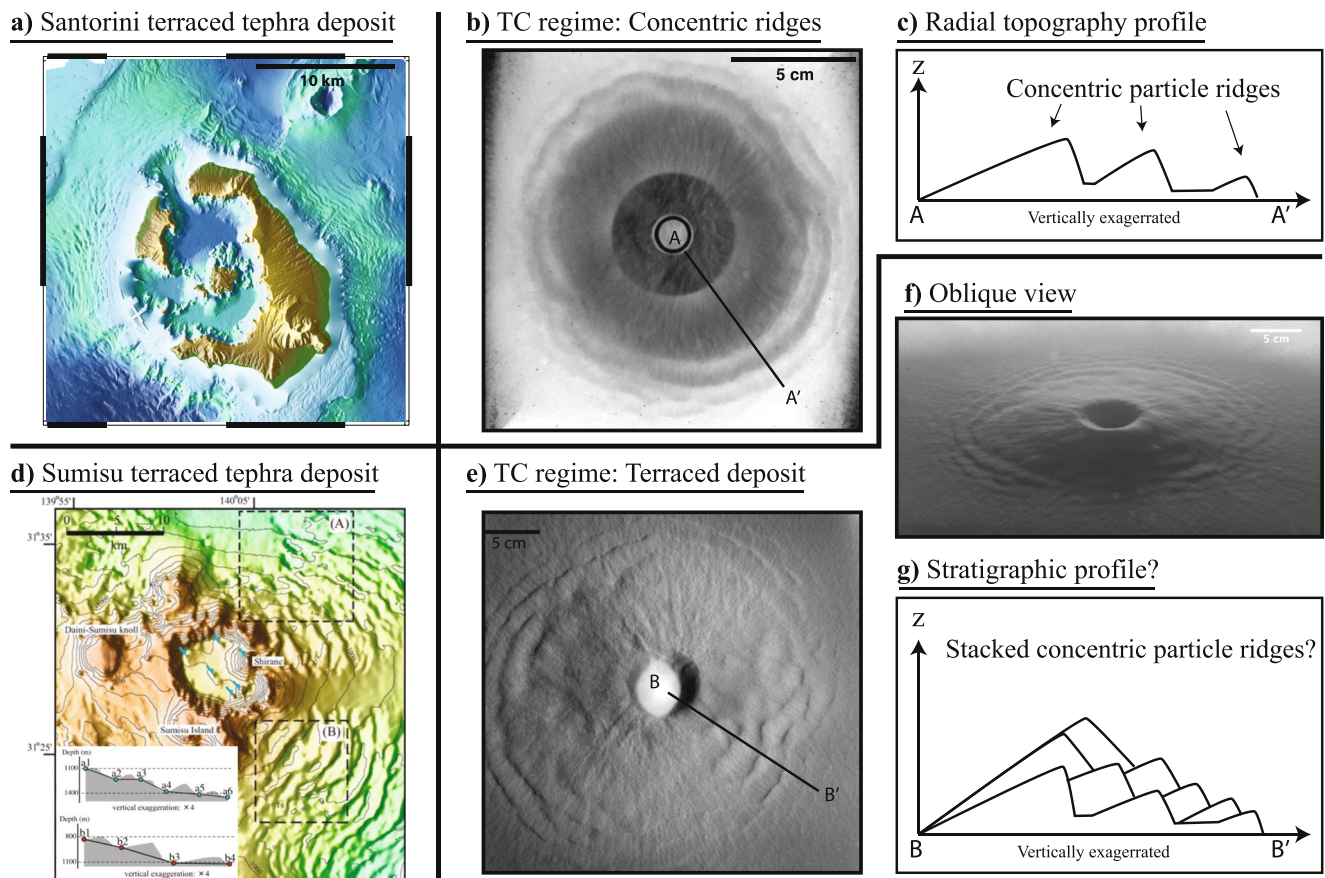
   (c) If $-\text{Ri}_0$ and ϕ_0 increase (Fig. 8), lower undershoots of the umbrella cloud below the LNB ($\zeta \rightarrow \geq 1$ signal a transition to the PC regime.

2. **Partial Collapse regime**: Volcanic jets with $2.4 \times 10^{-5} < -\text{Ri}_0 < 1.2 \times 10^{-3}$ and $6.0 \times 10^{-3} < \phi_0 < 5.7 \times^{-2}$ (Fig. 8)

   (a) Simultaneous spreading of umbrella cloud and pyroclastic flows can occur. Intermittent collapse of eruption columns does not require source parameters to vary.

   (b) Similar to the BP regime, periodic oscillations of the volcanic jet top height are a superposition of periodic oscillations of the fountain-plume transition height, H_{ftn}, the response of the density stratification of the ambient fluid N and the overshoot fountain height, H_{OS} (Figs. 4 & 17).

      (i) If N is known and H_{ftn}, H_{OS}, f_{ftn} and f_{OS} can be reliably measured from volcanic jet top height time series, then the momentum and buoyancy fluxes at the source and at the umbrella cloud

a) Santorini terraced tephra deposit

b) TC regime: Concentric ridges

c) Radial topography profile

d) Sumisu terraced tephra deposit

e) TC regime: Terraced deposit

f) Oblique view

g) Stratigraphic profile?

Fig. 29 (a) Bathymetry of proximal deposit around Santorini caldera, Greece exhibiting similar quasi-axisymmetric terraces reprinted from Hooft et al. (2019) with permission from Elsevier. (b) Proximal deposit emplaced by coarse particle jet in the TC regime injected with a low total particle mass through an annular nozzle. (c) Inferred radial topography profile along A-A' in (b), which resembles the large scale features of topographical profiles in (a). (d) Bathymetry Sumisu caldera, Izu-Bonin arc and surrounding proximal deposit from the 30-60 ka eruption. Insets are radial bathymetry profiles taken from zones (A) and (B) with dotted outlines. Note the inclination of upslope region of terraces that give terrace crests a ridge-like topography. Reprinted from Tani et al. (2008) with permission from Springer Nature. (e) Terraced proximal deposit emplaced by coarse particle jet in the TC regime. (f) Oblique view of terraced deposit in (e). (g) Hypothesis of stratigraphic profile along B-B' in (e). On the basis of observations in (b), terraced deposits are assumed to be composed of stacks of concentric particle ridges with a topographical profile similar to that in (a) and (e)

LNB can be inferred (Eqs. 7, 11, 10 & 12).

(c) Multiply layered ash clouds are a diagnostic feature of eruption columns occurring in the PC regime (Figs. 2, 11b, 12 & 26).

(d) Periodic oscillations of H_{OS} reflect small volume non-axisymmetric sediment waves that can disperse above the ground or descend to the ground and spread as pyroclastic flows. Both processes produce phoenix cloud layers.

    (i) The simultaneous occurrences of periodic and relatively small volume non-axisymmetric sediment waves and umbrella cloud spreading may be linked to alternating pyroclastic flow and air fall layers

in the proximal deposit that are laterally discontinuous (Fig. 25).

(e) Periodic oscillations of H_{ftn} are linked to relatively large volume axisymmetric sediment waves that transform into pyroclastic flows spreading axisymmetrically from the enhanced settling annulus (Figs. 11b, 12 & 17).

    (i) The simultaneous occurrences of periodic and relatively large volume axisymmetric sediment waves and umbrella cloud spreading is linked to alternating pyroclastic flow and air fall layers in the proximal deposit (Figs. 2 & 3).

(f) For eruption columns with $-\mathrm{Ri}_0 \leftrightarrow \phi_0$ near the PC/TC regime transition, quasi-axisymmetric and

regularly spaced terraces in the proximal deposit are linked to deposition from periodic and large volume axisymmetric sediment waves impacting the ground.

   (i) Terraces are expected to form within 1.5 jet diameters (taken at H_{ftn}) from the vent, which sets the radial extent of the enhanced settling annulus from the vent.

3. **Total Collapse regime:** Volcanic jets with $-Ri_0 > 2.7 \times 10^{-4}$ and $\phi_0 > 2.4 \times 10^{-2}$ (Fig. 8)

   (a) If H_{ftn} and f_{ftn} can be estimated from volcanic jet top height time series, then the momentum and buoyancy fluxes at the source can be inferred (Eqs. 7 & 10).
   (b) Periodic oscillations of H_{ftn} are linked to relatively large volume axisymmetric sediment waves that transform into pyroclastic flows spreading axisymmetrically from the enhanced settling annulus (Figs. 12 & 17).
   (c) Phoenix clouds rising above pyroclastic flows and spreading into phoenix cloud layers can veil the lower region of the volcanic jet (Fig. 13).
   (d) For proximal deposits with no layers linked to air fall from an umbrella cloud, quasi-axisymmetric and regularly spaced terraces characterize eruption columns with $-Ri_0 \leftrightarrow \phi_0$ occurring in the TC regime (Figs. 12, 20, 21, 28 & 29).

With these predictions in mind, to show the utility as well as limitations of our results we now revisit several well-studied eruption deposits in the context of fountain dynamics driving column collapse expressed as sediment waves. The following eruptions exhibit characteristics indicative of a BP→PC→TC or PC→TC regime evolution, both of which suggest that $-Ri_0$ increased during the eruption.

Climactic eruption of Mount Pinatubo (1991): gradual BP→PC→TC evolution

Rosi et al. (2001) combine evidence from satellite observations (Holasek et al. 1996) and deposit stratigraphy (Koyaguchi and Masami 1993; Paladio-Melasantos et al. 1996; Scott et al. 1996) to suggest that the 6 hr climactic phase of the 1991 Mount Pinatubo eruption (Philippines) produced a column that emerged near the BP/PC regime transition (Fig. 8), gradually evolved to the PC regime, and ultimately to the TC regime. We now discuss this hypothesis, with supporting satellite and deposit observations (as detailed in Rosi et al. 2001), in the context of insights gained from our experiments and conceptual models in Fig. 22:

1. Phase I: Emergence as column near the BP/PC regime transition.

   (a) Observation/inference: Proximal deposit layers, indicating the occurrence of relatively small-volume pyroclastic flows with short runout distances, were emplaced simultaneously as the more distal air-fall layer C.
   (b) Model prediction: Fig. 22a-b predicts that sediment waves descending around eruption columns near the BP/PC regime transition will be relatively small-volume, dilute and impact the ground with low speed thereby traveling a relatively short distance from the base of the eruption column (cf. Figs. 8, 11, 12, 19a and 19b).

2. Phases II and III: Transition through PC regime

   (a) Observation/inference: during phase II, concurrent with continued air fall were spreading pyroclastic flows that were more voluminous, concentrated with tephra and had a larger runout distance than those in phase I. Further increases in pyroclastic flow volume, concentration and runout distance occurred during phase III.
   (b) Model prediction: As $-Ri_0$ and ϕ_0 increase among our experiments spanning the PC regime (Fig. 8), entrainment into the jet column is decreased (Fig. 14) leading to more concentrated and voluminous sediment waves. These sediment waves are concurrent with umbrella cloud spreading, impact the tank base with a higher speed and transform into gravity currents that travel a farther distance from the jet column base.
   (c) Observation/inference: overall decrease in maximum lithic size from the bottom to top of the more distal Layer C air fall deposit (Rosi et al. 2001). This observation implies an overall decrease in the particle size dragged upward by the plume region of the column and, therefore, an increase in $-Ri_0$.
   (d) Model prediction: Fig. 22a-b predicts that an increase of $-Ri_0$ of a jet column near the BP/PC regime transition (Fig. 8) will place the jet in the PC regime.
   (e) Observation/inference: gradual reduction of column height from 39.1 km to 32.1 km accompanying the change in pyroclastic flow properties during transition from phase II to phase III of the eruption.
   (f) Model prediction: For a given ϕ_0, our models predict that an increase in $-Ri_0$ is linked to a decrease in column height.
   (g) Observation/inference: fluctuations in column height during a period of overall gradual decrease in column height inferred from the occasional occurrence

of oversized clasts in the stratigraphy of air fall layer C.

(h) Model prediction: increased amplitude of height fluctuations about the mean height are indicative of decreased column stability and analogous to measurements of a factor of two increase in the standard deviation of jet height fluctuations in our experiments with increasing $-Ri_0$ and ϕ_0 spanning the BP-PC-TC regimes (Fig. 16).

(i) Observation/inference: inferred time interval between pyroclastic flow layer emplacement decreased from 16-24 min during phase II ("lower surges") to 3-13 min during phase III ("upper surges").

(j) Model prediction: Fig. 22b-c predicts an increase of sediment wave occurrence frequency as $-Ri_0$ and ϕ_0 for an eruption column increases from the PC to TC regime (Figs. 8 & 17).

3. Phase IV: Transition to TC regime

(a) Observation/inference: further increase in the volume of pyroclastic flows, their tephra concentration and runout distance compared to pyroclastic flows in previous eruption phases. This agrees with our observations of increased sediment wave volume and modeled particle volume fraction as, for a given ϕ_0, $-Ri_0$ increases for jets spanning the PC to TC regimes (Figs. 8, 11, 12 & 19b). No associated tephra fall out with this phase suggesting a full transition to an eruption column in the TC regime.

(b) Model prediction: as discussed in "Controls on ash cloud structure by sediment wave dynamics" and shown in Fig. 27 for an eruption column in the TC regime, phoenix clouds can rise to a similar height as the top of the volcanic jet and obscure observations of the jet core where fountain dynamics govern the behavior of sediment waves.

(c) Our results and Fig. 27 support the hypothesis of Rosi et al. (2001) that the overshooting top observed above the umbrella cloud during this phase of the eruption (Holasek et al. 1996) was formed by overshooting phoenix clouds rising from pyroclastic flows spreading around an eruption column in the TC regime (referred to as a "co-ignimbrite" column in Rosi et al. 2001).

In summary, the evolution of the climactic phase of the 1991 eruption of Mount Pinatubo most likely followed a BP→PC→TC regime evolution consistent with expectations drawn from the conceptual model in Fig. 22. A difference between our proposed model and the evolution of this eruption is that the phoenix clouds in phase IV rose to similar or higher heights than the maximum height of the veiled volcanic jet, analogous to Figure 11 in

Carey et al. (1988) and the alternative conceptual models in Fig. 27b.

Quilotoa, Ecuador, 0.8 ka: evolution of pyroclastic flows through the PC regime

The deposit analysis of the 0.8 ka plinian eruption of Quilotoa volcano in Ecuador by Di Muro et al. (2008) suggests a BP→PC→TC regime evolution on the basis of the following observations in the U1 stratigraphic unit (see Fig. 2c in their study):

1. A1 submember: lowermost air fall layer in U1 unit

(a) Observations: reverse grading of the lowermost part of this layer, which marks the onset of the climactic eruption phase that emplaced the U1 unit and lies beneath the first pyroclastic flow layers, indicates an eruption column increasing in height in the BP regime. This air fall layer also exhibits poor sorting in the proximal deposit.

(b) Model predictions: for the BP regime Fig. 22d suggests that the reverse grading is linked to an eruption column with an initially decreasing $-Ri_0$, for a given ϕ_0, until the column reaches its maximum height and predicts the emplacement of air fall layers without pyroclastic flow layers and intermittent sedimentation of particles within the enhanced settling annulus for volcanic jets near the $-Ri_0 \leftrightarrow \phi_0$ parameter space of the BP/PC regime transition (Fig. 8) as a result of small sediment waves dispersing below the umbrella cloud. Phoenix cloud interactions with sediment waves are most common for jets near the BP/PC regime transition (Fig. 12e) and these interactions will lead to complex sedimentation within the enhanced settling annulus that may result in a poorly sorted air fall deposit layer.

2. A2 submember (overlying A1): air fall layers intercalated with pyroclastic flow layers

(a) Observations/inferences: with increasing stratigraphic height the median particle and maximum clast sizes decrease where lithic content increases, possibly due to a lowering of the eruption column as a result of vent erosion and widening. Where these observations are made proximal to the vent, the A2 air fall deposit is intercalated with pyroclastic flow layers and is therefore an example of an alternating air fall–pyroclastic flow layered proximal deposit, which is a common feature of plinian eruption deposits (Fig. 2). The inferred

interval of pyroclastic flow layer emplacement in this unit decreases from > 9 min (S2 phase) to < 5 min (S3c phase). The areal extent of pyroclastic flow layers associated with the A2 submember are quasi-axisymmetric about the vent.

(b)　Model predictions: for the transition of an eruption column from the BP→PC regime, Fig. 22d-e predicts a lowering of the eruption column and decrease in median and maximum particle sizes in the air fall deposit. Figure 22d-e also predicts that during column lowering and transition to the PC regime, sediment waves will increase in frequency and periodically reach the ground to emplace pyroclastic flow layers in the proximal deposit while tephra from the umbrella cloud continues to emplace air fall layers in between pyroclastic flow layers. pyroclastic flows originating from large volume annular sediment waves are predicted to spread axisymmetrically from the base of the volcanic jet.

3.　B member: pyroclastic flow layers overlying A member and capping U1 unit

(a)　Observations: in the proximal deposit on the caldera rim, the B member overlies the A member with an abrupt contact between the two that shows evidence of erosion in some places. The massive matrix supported layers comprising the B member, with lower layers rich in lithic breccia and upper layers exhibiting dune morphologies, are interpreted as pyroclastic flow layers emplaced by an eruption column in the Total Collapse regime and have a longer runout distance than pyroclastic flow layers in the A member.

(b)　Model predictions: for an eruption column transitioning from the PC→TC regime Fig. 22e-f predicts the occurrence of annular sediment waves with increasing volume, concentration and runout distance as $-Ri_0$ decreases for a given ϕ_0.

Overall, the evolution of the 0.8 ka Quilotoa eruption column, inferred from deposit architecture, stratigraphy and componentry by Di Muro et al. (2008), is in good agreement with our conceptual models for a BP→PC→TC regime evolution and implies that, for a given ϕ_0, $-Ri_0$ increased gradually through the PC regime during the eruption (Figs. 8 & 22). Di Muro et al. (2008) interpret the increasing presence of lithics moving upward in layer U1, where juvenile componentry is relatively unchanging, as an indication of changing vent geometry during this period of the eruption that led to a change in eruption column behavior. An increasing presence of lithic particles in the eruption column equates to a change in the average particle

density, which is a process not included in our models, but one that would potentially increase the bulk density of the erupted mixture and, all other variables being equal, increase $-Ri_0$. Modification of vent geometry, all other variables remaining unchanged, would modify $-Ri_0$ as well and in the case of vent widening, would also increase $-Ri_0$.

Calbuco, Chile, 2015: sediment waves falling from fountain/plume transition height and LNB

In April, 2015 in Chile, the sub-plinian eruption of Calbuco volcano produced an eruption column that exhibited characteristics of the BP, PC and TC regimes on the basis of the following observations (Castruccio et al. 2016; Van Eaton et al. 2016):

1.　Phase 1: BP regime near the PC regime boundary

(a)　Observation/inference: visual observations of pyroclastic flows spreading from the base of the developing volcanic jet during eruption onset (see Figure 2a in Castruccio et al. 2016). Throughout the duration of this eruptive phase, visual observations of spreading pyroclastic flows and ash clouds spreading below the spreading umbrella cloud continued (Fig. 1b https://www.youtube.com/watch?v=UsUKMtpq3w8). The eruption column reached a statistically steady mean column height while the umbrella cloud spread at a constant rate, implying steady source parameters (Van Eaton et al. 2016). The overshooting top of the eruption column above the umbrella cloud persisted and fluctuated throughout this eruptive phase (https://www.youtube.com/watch?v=UsUKMtpq3w8). These observations suggest that the eruption emerged and remained in the PC regime with steady source parameters for the entirety of this eruptive phase (Van Eaton et al. 2016).

(b)　Model predictions: Figs. 8 and 22e predict that eruptions with $2.4 \times 10^{-5} < -Ri_0 < 1.2 \times 10^{-3}$ and $6.0 \times 10^{-3} < \phi_0 < 5.7 \times^{-2}$ occur in the PC regime with simultaneous spreading of the umbrella cloud, phoenix cloud layers below and pyroclastic flows along the ground. Our model predicts that sediment waves descended from H_{ftn} and transformed into pyroclastic flows. Above this height, the fluctuations of the overshoot region suggest that sediment waves descended from H_{LNB}. If these sediment waves dispersed before reaching the ground, they may be the source of the higher ash clouds observed to spread below the umbrella cloud. Figure 22e also predicts that phoenix cloud

layers will spread from the fountain–plume transition height in the eruption column; therefore, the multitude of ash cloud layers observed to spread below the umbrella cloud may have three distinct sources: (1) sediment waves descending from the overshoot region and dispersing before reaching the ground, (2) erupted mixture spreading directly from H_{ftn}, (3) phoenix clouds rising from pyroclastic flows and spreading into phoenix cloud layers. As a final note, three dimensional eulerian-langrangian numerical simulations of this eruptive phase by Cerminara et al. (2017) visually exhibit sedimentation waves comprised of 1-2 mm langrangian particles (modeled with one-way fluid→particle coupling where particle motions do not affect fluid phase dynamics, but with $St_0 \approx 1$ & $\Sigma_0 < 1$) descending from the overshoot region and to the northeast of the simulated eruption column (https://www.youtube.com/watch?v=erevLQDAtHw). The occurrences of sedimentation waves in these simulations is supported by the intermittent or periodic fluctuations of sedimentation mass flux measured at 7 km (for particles with $d_p = 2$ mm) and 10 km ($d_p = 1$ mm) from the vent. Although the langrangian particles are not modeled in a two-way coupling (inertial) regime by Cerminara et al. (2017), the intermittent or periodic sedimentation behavior of $St_0 \approx 1$ particles around an eruption column in the PC regime, visually linked to intermittent or periodic fluctuations of the overshoot region, are in agreement with our experimental observations and new conceptual model predictions.

2. Phase 2: BP→PC regime evolution

(a) Observations/inferences: Approximately two hours into the second eruptive phase, Van Eaton et al. (2016) observe a cessation of umbrella cloud spreading followed by an increase in proximal volcanic lightning rates and infer a decrease in mass flux delivered to the umbrella cloud at this time. Van Eaton et al. (2016) link this abrupt change in eruptive behavior to the occurrence of pyroclastic flows, which is supported by compositional changes in tephra in the stratigraphy of the deposit correlated to this period of the eruption (Romero et al. 2016; Castruccio et al. 2016). Castruccio et al. (2016) note that the pyroclastic flow deposits of this eruptive phase only represent $\approx 10\%$ of the total erupted volume, implying that the eruption column did not spend significant time in the TC regime. Van Eaton et al. (2016) and Castruccio et al. (2016) suggest these changes are indicative of a transition of the eruption column to the PC regime.

(b) Model predictions: For an eruption column transitioning from the BP→PC regime, Fig. 8 predicts the source parameters to change from $-Ri_0 < 2.2 \times 10^{-4}$ and $\phi_0 < 3.5 \times 10^{-2}$ for the BP regime to $2.4 \times 10^{-5} < -Ri_0 < 1.2 \times 10^{-3}$ and $6.0 \times 10^{-3} < \phi_0 < 5.7 \times^{-2}$ for the PC regime. During this transition, Fig. 22d-e predicts a decrease in the mass flux delivered to the umbrella cloud in favor of more of the volcanic jet mass flux partitioned into collapse via sediment waves from H_{ftn} and H_{LNB}. The dispersal of sediment waves above the ground or transformation into pyroclastic flows will drive the rise of phoenix clouds and spreading of multiple phoenix cloud layers below the umbrella cloud, favoring the occurrence of proximal lightning as proposed by Van Eaton et al. (2016).

Visual and remote sensing observations of the Phase 1 eruption column suggest an occurrence in the BP regime near the PC regime boundary with steady source parameters as the umbrella cloud, lower clouds and pyroclastic flows were observed to spread simultaneously. The combination of a spreading umbrella cloud underlain by spreading phoenix cloud layers represents a natural example of a multiply layered ash cloud that is characteristic of the PC regime, however estimates that $< 10\%$ of the Phase 1 deposit is linked to PDCs suggests a column in the BP regime near the PC regime boundary. The umbrella cloud and deposit observations for Phase 2 strongly suggest an eruption column occurring in the PC regime. The potential occurrences of sediment waves in numerical simulations of this eruption suggest that sediment waves descending from an overshoot region fluctuating in height are a fundamental feature eruption columns in the PC regime with a significant fraction of tephra in the $St_0 \sim 1$ range (Jessop et al. 2016). We are not aware of any observations of alternating airfall/pyroclastic flow layering in the proximal deposit, and in turn, estimates of the timing between pyroclastic flow layer emplacement.

Sumisu, Izu-Bonin Arc, 30-60 ka: terraced deposit from CCF eruption

The proximal deposit of the 30-60 ka eruption of Sumisu caldera has been studied by Tani et al. (2008) and is an example of an ancient CCF eruption deposit that has a striking resemblance to the terraced deposits observed in our experiments on the basis of the following:

1. Observation/inferences: The submarine flanks of Sumisu caldera are characterized by quasi-axisymmetric terraces comprised of unconsolidated tephra from the

30-60 ka CCF eruption (Fig. 29a). Seismic surveys suggest that terracing topography is restricted to the top layer of the volcano edifice, which overlies pre-30–60 ka eruption layers (Figure 8 in Tani et al. 2008). Radial topography profiles of these quasi-axisymmetric terraces (insets in Fig. 29a) show a non-monotonic decrease in deposit thickness with increasing radius from the caldera rim (Tani et al. 2008).

2. Model predictions: Figs. 22e–f and 27 predict that an eruption column in the PC regime near the PC/TC transition or in the TC regime will emplace a proximal deposit characterized by axisymmetric terraces with maximum radii equal to the radii of the enhanced settling annulus. The radial bathymetry profiles of Sumisu caldera show local high points at the crest of each terrace, similar to the observed radial topography of the concentric ridge deposit in Fig. 29c. Each concentric particle ridge in Fig. 29c shows a gradual decrease in thickness back towards the nozzle, in contrast to the abrupt decrease marking a terrace feature in the direction away from the nozzle. This asymmetry of the change in thickness of each concentric ridge about it's local high point is identical to that observed in the radial topography profiles of Sumisu. An additional prediction is that the impact and spread of sediment waves should drive erosion upstream near the impact zone and deposition downstream, consistent with expectations from studies of eroding ground-hugging gravity currents (Hall et al. 2008).

The bathymetry of the proximal deposit around Sumisu caldera is similar to proximal deposit terracing observed around the calderas of Santorini, Greece (Fig. 29b; Hooft et al. 2019) and Macauley volcano, Kermadec arc (Rotella et al. 2013). These observations suggest that quasi-axisymmetric terraces in proximal deposits around submarine calderas may be a characteristic feature of submarine CCF eruption deposits. Our models suggest that proximal terracing around these submarine calderas are linked to the occurrence of large annular sediment waves descending around CCF eruption columns in the PC or TC regime and that the distance to the outermost terrace may be linked to the geometry of the eruption column (Fig. 21). Although our model captures key qualitative features of these deposits, observed terrace widths are an order of magnitude or more larger than expected on the basis of the enhanced settling annulus radius for circular vents and potentially larger than expected also for annular vents explored in Jessop et al. (2016). As discussed briefly above, the enhanced radii of terraces may be related to interactions between descending sediment waves with a free surface and/or the seafloor. That our current results do not explain this key geometric property underscores a limit of the mechanics we investigate.

Conclusions

We conducted an extensive series of analog multiphase experiments (Tables 1 & 2) on volcanic jets for a range of source parameters inferred for explosive eruptions (Table 3) with the goal of answering the three motivating research questions presented in Section "Introduction". Informed by qualitative observations and quantitative results from our experiments, observations from the field and theory, we describe how fountain dynamics combined with the presence of particles govern the gravitational stability of volcanic jets and, in turn, the descent of sediment waves that drive commonly observed ash cloud structures and deposit architectures. Crucially, our observations of sediment wave behavior combined with a $-Ri_0 \leftrightarrow \phi_0$ regime diagram demonstrate that multiphase jets, and therefore volcanic jets, can transition smoothly among the BP↔PC↔TC regimes as source parameters gradually change during an eruption. Furthermore, the very broadly ranging conditions that mark the PC regime suggest that the majority of Plinian eruptions will occur within this previously underexplored regime. For volcanic jets, we describe how a $-Ri_0 \leftrightarrow \phi_0$ regime diagram can be used to predict the regime of an eruption column or, when combined with observations of cloud structure and deposit architecture, to constrain source parameters of an eruption column. In more detail, for each eruption column regime we make the following conclusions:

1. **Buoyant Plume:**

   (a) Inertial particles with $1 < St_0 < 10$, such as lapilli-sized pyroclasts in natural eruptions, influence the entrainment rate of ambient fluid and their presence in volcanic jets can influence eruption column rise and stability against gravitational collapse.

   (b) Measurements of eruption column overshoot height time series can be used to infer the momentum and buoyancy fluxes of the volcanic jet at the LNB of the umbrella cloud and to predict the occurrence frequency of small volume sediment waves descending around the jet column within the enhanced settling annulus.

   (c) The dispersal of small sediment waves drives the spread of phoenix cloud layers below the umbrella cloud and may lead to internal layering in the umbrella cloud.

(d) The occurrence and dispersal of small sediment waves leads to intermittent or periodic sedimentation of particles to the proximal deposit within the enhanced settling annulus.

(e) The collapse number, ζ, can be monitored with remote sensing methods and provides a metric for the stability of eruption columns, where $\zeta \geq 1$ indicates a transition to the PC regime.

2. **Total Collapse:**

(a) Measurements of eruption column top height time series can be used to infer the source momentum and buoyancy fluxes of volcanic jets and to predict the occurrence frequency of periodic, large volume annular sediment waves descending around the jet column within the enhanced settling annulus.

(b) Sedimentation occurs primarily via large sediment waves that emplace axisymmetric terraces or concentric ridges in the proximal deposit within the enhanced settling annulus.

(c) Upon impact with the ground, large sediment waves transform into pyroclastic flows spreading axisymmetrically out of the enhanced settling annulus.

(d) Phoenix clouds rising above pyroclastic flows spread into one or more phoenix cloud layers and can obscure observations of the eruption column.

3. **Partial Collapse:**

(a) The presence of coarse particles with $1 < \text{St}_0 < 10$ can increase the rate of entrainment into relatively strong volcanic jets.

(b) Volcanic jet top height time series are dominated by the superposition of signals related to oscillations of the fountain-plume transition height (lower fountain), the response of the density stratification of the ambient fluid and the overshoot height (overshoot fountain). Determination of these signals in volcanic jet height time series can be used to infer the momentum and buoyancy fluxes of the erupted mixture at the source and the LNB.

(c) Sediment waves descending around the jet column drive simultaneous partitioning of erupted mass among spreading umbrella clouds, phoenix cloud layers and PDCs.

(d) Large volume annular sediment waves descend periodically around the jet column within the enhanced settling annulus from the fountain-plume transition height with a frequency predicted by the ratio of the source buoyancy to momentum fluxes.

(e) Small volume non-axisymmetric sediment waves descend periodically from the overshoot region around the jet column within the enhanced settling annulus with a frequency predicted by the ratio of the buoyancy to momentum fluxes of the mixture at the umbrella LNB.

(f) Phoenix clouds rising from pyroclastic flows or dispersing sediment waves spread into phoenix cloud layers at multiple heights below the umbrella cloud and form a multiply layered ash cloud that is characteristic of this regime.

(g) Large sediment waves transform into pyroclastic flows spreading axisymmetrically out of the enhanced settling annulus whereas small sediment waves transform into pyroclastic flows spreading out from one side or another of the enhanced settling annulus.

(h) For jets near the PC/TC regime transition, large volume sediment waves emplace axisymmetric terraces in the proximal deposit within the enhanced settling annulus.

Rather than being a short-lived transient regime between endmember BP and TC regimes, growing evidence from field-, laboratory- and computer-based studies suggest that Plinian eruptions most commonly emerge and exist in the PC regime during eruptive phases where the majority of erupted material is emplaced. Our results support this new perspective on eruption column regimes as the PC regime covers an extensive parameter space on a $-\text{Ri}_0 \leftrightarrow \phi_0$ regime diagram. In addition, we find that the $-\text{Ri}_0$ and ϕ_0 ranges for the PC regime depend on the particle size distribution present in the multiphase jet. The presence of inertial particles, with $1 < \text{St}_0 < 10$, also influences the process of entrainment and and their contribution to mixture buoyancy favors the occurrence of sediment waves. Importantly, the presence of inertial particles can shift the BP/PC transition to smaller $-\text{Ri}_0$ and ϕ_0, thereby increasing the range of source parameters for which partial or total column collapses will occur. This net effect of inertial particles holds even for jet mixtures with positively buoyant interstitial fluid and can be captured by a jet stability number Λ_0 (Eq. 16) to compare multiphase jets with varying particle size distributions. However, a remaining question is whether critical values for the volume fraction of inertial particles exist, below which there are no influences on the $-\text{Ri}_0$ and ϕ_0 ranges for the PC regime, entrainment rates of ambient fluid into relatively strong jets or the occurrence of sediment waves.

We have demonstrated that individual Plinian eruptions often undergo a BP↔PC↔TC or PC↔TC regime evolution. Our conceptual models predict how these evolutions are governed by $-\text{Ri}_0$ and ϕ_0 and will be reflected by changes in column height fluctuations, sediment wave dyanmics, cloud structure, pyroclastic flow behavior and

deposit architecture. Real-time observations of simultaneous umbrella cloud, lower cloud and pyroclastic flow spreading and field observations of alternating air-fall and pyroclastic flow layering in proximal deposits as well as quasi-axisymmetric terracing around submarine CCF eruption deposits agree with many of our model predictions. Interestingly, our fine particle experiments in the PC regime suggest that eruptions near the BP/PC regime transition where $\zeta \rightarrow 1$ over time may undergo a "late collapse" driven by a positive feedback cycle of entrainment of particle-fluid mixtures undershooting below the umbrella cloud LNB and, ultimately, transition into the PC regime without source parameters changing. In addition to testing our Collapse number hypothesis as a monitoring tool, future studies should constrain the period of column overshoot height oscillations expected for natural eruptions to determine if these can be resolved with current remote sensing techniques.

Our results combined with those of Jessop et al. (2016) indicate that submarine CCF eruptions have a proclivity to occur in the PC regime near the PC/TC transition and in the TC regime. In turn, we expect these eruptions to emplace quasi-axisymmetric terraces or concentric ridges in the proximal deposit as a result of periodic, large volume and axisymmetric sediment waves operating as the dominant process of proximal sedimentation for these eruptions. Our PC and TC eruption column regime models, whereby collapse is governed by periodic, large volume sediment waves, are distinct from the boiling over model (Rowley et al. 1981; Criswell 1987; Pacheco-Hoyos et al. 2018; Suñe-puchol et al. 2019). Precisely how tephra is deposited upon impact of a large sediment wave with the ground and whether horizontal flow of ensuing pyroclastic flows modifies proximal deposit terracing is unclear.

To improve our understanding of the volume flux of erupted mixture delivered to cloud spreading in the atmosphere versus collapse and spreading via pyroclastic flows during eruptions, future studies should focus on constraining the volume flux of injected mixture carried by sediment waves descending around multiphase jet columns. In particular, the particle volume fraction of sediment waves and the buoyancy of their interstitial fluid most likely govern whether they disperse before reaching the ground and will be modified as they entrain ambient fluid during descent. Yet, the rate of volume exchange between fluid descending next to an upward flowing fluid jet is poorly constrained (Fig. 23e; Bloomfield and Kerr 2000) and, to the best of our knowledge, unknown for sediment waves descending next to multiphase jets. These areas of research are critical for determining how sediment waves can set the source conditions for intermittent or periodic PDCs and phoenix cloud layers spreading during explosive eruptions. In addition, our analog experiments provide a dataset that can be used to benchmark numerical simulations of multiphase jets, and in turn, numerical simulations can investigate the volume fluxes of multiphase jets, descending sediment waves and spreading gravity currents in greater temporal and spatial resolution.

Appendix A: Mixture bulk density, particle drag factor and Reynolds number

The bulk density of a solid-fluid phase mixture is given by

$$\rho = (1 - \phi)\rho_f + \phi\rho_p \tag{18}$$

for a monodispere PSD with $\phi = \phi_{cp}$ or ϕ_{fp}, particle density $\rho_p = \rho_{cp}$ or ρ_{fp}, and for a bidisperse PSD

$$\rho = (1 - \phi_{cp} - \phi_{fp})\rho_f + \phi_{cp}\rho_{cp} + \phi_{fp}\rho_{fp} \tag{19}$$

Eqs. 18 and 19 can be defined at the source with the density of interstitial jet water $\rho_f = \rho_{w,0}$, $\phi = \phi_0$, $\phi_{cp} = \phi_{cp,0}$ and $\phi_{fp} = \phi_{fp,0}$ (Jessop et al. 2016).

The particle drag factor, f_p, which is used to calculate the particle response time in Eq. 13 (particle Stokes number), and Reynolds number, Re_p, are defined as

$$f_p = 1 + 0.15Re_p^{0.687} + \frac{0.0175}{1 + 42,500Re_p^{-1.16}} \tag{20}$$

$$Re_p = \frac{U_s L}{v_w} \tag{21}$$

where U_s is the terminal settling velocity of the particle (Burgisser et al. 2005). f_p and Re_p can be defined at the jet source with $L = d_p$ and v_w is the kinematic viscosity of water.

Appendix B: 1D integral plume model: Effective entrainment parameter and jet conditions above source

One goal of this study is to investigate the effects of two-way and fully coupled particles and interstitial fluid buoyancy on the process of entrainment for the initial transient jet. Following the methods of Morton et al. (1956) and Bloomfield and Kerr (1998) and Carazzo and Jellinek (2012) , we numerically solve a 1D integral plume model with a Boussinesq approximation (density differences only accounted for in buoyancy terms) in which particles are conserved up to the maximum height of the jet, where $u(z) \rightarrow 0$, to determine an effective entrainment parameter value for the initial jet in an experiment. Using Eqs. 3a-3c

to set the initial conditions of the plume model, we solve for their change with height

$$\frac{dQ}{dz} = 2\alpha_e r(z)u(z) \tag{22a}$$

$$\frac{dM}{dz} = g'(z)r(z)^2 \tag{22b}$$

$$\frac{dB}{dz} = -N(z)^2 r(z)^2 u(z) \tag{22c}$$

until $u(z) \to 0$. To account for the change in ϕ_0 with height, we assume conservation of particles where no particles exit the jet mixture during rise (Carazzo and Jellinek 2012)

$$\phi(\text{z}) = \frac{\phi_0 Q_0}{Q(z)} \tag{23}$$

This set of equations is closed with Eq. 1 and the model is initiated with source parameters determined by Eqs. 3a-3c and the source particle volume fraction ϕ_0. We note that this method is limited to modeling the initial jet when it enters the quiescent tank environment and, therefore, cannot model re-entrainment of collapsing material or account for the dynamics of the oscillating overshoot region.

Once an effective entrainment parameter is determined for initial jet rise in each experiment, we model the jet conditions at the observed LNB height of the jet fluid, where $g'_f \to 0$, for jets in the BP and PC regimes. In particular, we estimate the momentum flux, M_{LNB}, buoyancy flux, B_{LNB} and particle volume fraction, ϕ_{LNB}, of the mixture. M_{LNB} and B_{LNB} are used in Eq. 12 to predict the oscillation frequency of the overshoot fountain, f_{OS} (see "Scaling natural volcanic jets to the laboratory setting"), whereas ϕ_{LNB} is compared with the descent velocity of sediment waves. We note that during the steady-state period of an experiment, this simple modeling approach does not capture mass and momentum exchange between the jet and mixture descending from the overshoot fountain along the jet edge. Additionally, this modeling approach does not capture processes such as entrainment of collapsing mixture.

To further investigate the effect of coarse and fine particles, with $0.2 < St_0 < 6$, on the process of entrainment, we use the Kaminski et al. (2005) and Carazzo et al. (2008) entrainment parameterization (variable entrainment model) to predict the maximum rise height of experimental jets

$$\alpha_e(z) = |\text{Ri}(z)|\left(1 - \frac{1}{A}\right) + \frac{1}{2}\frac{dlnA}{dz} + \frac{1}{2}C \tag{24}$$

where $|\text{Ri}(z)|$ is the local Richardson number. $A = 1.1$ and $C = 0.135$ and are constant for the model run. Maximum jet heights predicted with the variable entrainment model are compared to measured maximum jet heights during the initial transient phase of the experiment. These results are then used to determine if the variable entrainment model over- or underestimates entrainment for jets with particles.

References

Andrews BJ, Gardner JE (2009) Turbulent dynamics of the 18 May 1980 Mount St. Helens eruption column. https://doi.org/10.1130/G30168A.1

Aramaki S (1984) Formation of the Aira caldera, southern Kyushu, approx 22 000 years ago. J Geophys Res 89(B10):8485–8501. https://doi.org/10.1029/JB089iB10p08485

Aubry TJ, Carazzo G, Jellinek AM (2017a) Turbulent entrainment into volcanic plumes: New constraints from laboratory experiments on buoyant jets rising in a stratified crossflow. Geophys Res Lett 44(20):10198–10207. https://doi.org/10.1002/2017GL075069

Aubry TJ, Jellinek AM, Carazzo G, Gallo R, Hatcher K, Jack D (2017b) A new analytical scaling for turbulent wind-bent plumes: Comparison of scaling laws with analog experiments and a new database of eruptive conditions for predicting the height of volcanic plumes. J Volcanol Geotherm Res 343:233–251. https://doi.org/10.1016/j.jvolgeores.2017.07.006

Aubry TJ, Jellinek AM (2018) New insights on entrainment and condensation in volcanic plumes: constraints from independent observations of explosive eruptions and implications for assessing their impacts. Earth Plan Sci Lett 490:132–142. https://doi.org/10.1016/j.epsl.2018.03.028

Aubry TJ, Jellinek AM, Degruyter W, Bonadonna C, Radíc V, Clyne M, Quainoo A (2016) Impact of global warming on the rise of volcanic plumes and implications for future volcanic aerosol forcing. J Geophys Res 121(22):13326–13351. https://doi.org/10.1002/2016JD025405

Aubry TJ, Engwell S, Bonadonna C, Carazzo G, Scollo S, Van Eaton AR, Taylor IA, Jessop D, Eychenne J, Gouhier M, Mastin LG (2021) The Independent Volcanic Eruption Source Parameter Archive (IVESPA, version 1.0): A new observational database to support explosive eruptive column model validation and development. J of Volcanol Geotherm Res 417:107295–107326

Baines WD, Turner JS, Campbell IH (1990) Turbulent fountains in an open chamber. J Fluid Mech 212:557–592

Balachandar S, Eaton JK (2010) Turbulent Dispersed Multiphase Flow. Ann Rev Fluid Mech 42(1):111–133. https://doi.org/10.1146/annurev.fluid.010908.165243. ISBN 0066-4189\r1545-4479

Black BA, Neely RR, Manga M (2015) Campanian Ignimbrite volcanism, climate, and the final decline of the Neanderthals. Geology 43(5):411–414. https://doi.org/10.1130/G36514.1

Bloomfield LJ, Kerr RC (2000) A theoretical model of a turbulent fountain. J Fluid Mech 424:197–216. https://doi.org/10.1017/S0022112000001907

Bloomfield LJ, Kerr RC (1998) Turbulent fountains in a stratified environment. J Fluid Mech 389:27–54. https://doi.org/10.1017/S0022112099004772

Bloomfield LJ, Kerr RC (1999) Turbulent fountains in a confined stratified environment. J Fluid Mech 389:27–54

Bonadonna C, Ernst GGJ, Sparks RSJ (1998) Thickness variations and volume estimates of tephra fall deposits: the importance of particle Reynolds number. J Volcanol Geotherm Res 81(3-4):173–187. https://doi.org/10.1016/S0377-0273(98)00007-9

Bonadonna C, Costa A, Folch A, Koyaguchi T (2015) Tephra Dispersal and Sedimentation, 2nd edn. Elsevier Inc., Amsterdam. https://doi.org/10.1016/b978-0-12-385938-9.00033-x

Bonnecaze RT, Hallworth MA, Huppert HE, Lister JR (1995) Axisymmetric particle-driven gravity currents. J Fluid Mech 294:93–121

Brown RJ, Andrews GDM (2015) Deposits of Pyroclastic Density Currents, 2nd edn. Elsevier Inc., Amsterdam. https://doi.org/10.1016/B978-0-12-385938-9.00036-5

Burgisser A, Bergantz GW, Breidenthal RE (2005) Addressing complexity in laboratory experiments: the scaling of dilute multiphase flows in magmatic systems. J Volcanol Geotherm Res 141(3-4):245–265. https://doi.org/10.1016/j.jvolgeores.2004.11.001. ISBN 0377-0273

Burridge HC, Hunt GR (2013) The rhythm of fountains: The length and time scales of rise height fluctuations at low and high Froude numbers. J Fluid Mech 728:91–119. https://doi.org/10.1017/jfm.2013.263

Bush JWM, Thurber BA, Blanchette F (2003) Particle clouds in homogeneous and stratified environments. J Fluid Mech 489:29–54. https://doi.org/10.1017/S0022112003005160

Carazzo G, Jellinek AM (2013) Particle sedimentation and diffusive convection in volcanic ash-clouds. J Geophys Res Solid Earth 118(4):1420–1437

Carazzo G, Kaminski E, Tait S (2008) On the dynamics of volcanic columns: a comparison of field data with a new model of negatively buoyant jets. J Volcanol Geotherm Res 178(1):94–103. ISBN 0379-7112 https://doi.org/10.1016/j.jvolgeores.2008.01.002

Carazzo G, Kaminski E, Tait S (2010) The rise and fall of turbulent fountains: a new model for improved quantitative predictions. J Fluid Mech 657:265–284. https://doi.org/10.1017/S002211201000145X. ISBN 0022-1120

Carazzo G, Girault F, Aubry T, Bouquerel H, Kaminsky E (2014) Laboratory experiments of forced plumes in a density-stratified crossflow and implications for volcanic plumes. Geophys Res Lett 41(24):8759–8766

Carazzo G, Jellinek MA (2012) A new view of the dynamics, stability and longevity of volcanic clouds. Earth Planet Sci Lett 325-326:39–51. https://doi.org/10.1016/j.epsl.2012.01.025

Carazzo G, Kaminski E, Tait S (2006) The route to self-similarity in turbulent jets and plumes. J Fluid Mech 547:137–148. https://doi.org/10.1017/S002211200500683X. ISBN 0022-1120

Carazzo G, Girault F, Aubry T, Bouquerel H, Kaminski E (2014) Laboratory experiments of forced plumes in a density-stratified crossflow and implications for volcanic plumes. Geophys Res Lett 41(24):8759–8766. https://doi.org/10.1002/2014GL061887

Carey S, Sigurdsson H, Gardner JE, Cristwell W (1990) Variations in column height and magma discharge during the May 18, 1980 eruption of Mt. St. Helens. J Volcanol Geotherm Res 43:99–112. https://doi.org/10.1016/0377-0273(90)90047-J

Carey SN, Sigurdsson H, Sparks RSJ (1988) Experimental studies of particle-laden plumes. J Geophys Res 93(B12):314–328

Carey S, Bursik M (2015) Volcanic Plumes, 2nd edn. Elsevier Inc., Amsterdam. https://doi.org/10.1016/B978-0-12-385938-9.00032-8

Carey S, Haraldur S (1985) The May 18, 1980 Eruption of Mt. St. Helens. Modal Anal 90:2948–2958

Cas RAF, Wright JV (1987) Volcanic Successions: Modern and Ancient, 1st edn. Chapman & Hall, London. https://doi.org/10.1007/978-0-412-44640-5

Castruccio A, Clavero J, Segura A, Samaniego P, Roche O, Le Pennec J, Droguett B (2016) Eruptive parameters and dynamics of the April 2015 sub-Plinian eruptions of Calbuco volcano (southern Chile). Bulletin of Volcanology 78. https://doi.org/10.1007/s00445-016-1058-8

Cerminara M, Ongaro TE, Augusto N (2016) Large Eddy simulation of gas–particle kinematic decoupling and turbulent entrainment in volcanic plumes. Journal of Volcanology and Geothermal Research 326:143–171. https://doi.org/10.1016/j.jvolgeores.2016.06.018

Cerminara M, Ongaro TE, Paronuzzi S (2017) Three-dimensional numerical simulation of the april 2015 calbuco eruption: from the tephra deposit to the umbrella cloud. IAVCEI 2017 Scientific Assembly

Cioni R, Sulpizio R, Garruccio N (2003) Variability of the eruption dynamics during a Subplinian event: the Greenish Pumice eruption of Somma-Vesuvius (Italy). J Volcanol Geotherm Res 124(1-2):89–114. https://doi.org/10.1016/S0377-0273(03)00070-2. ISBN 0377-0273

Cioni R, Pistolesi M (2015) Plinian and Subplinian Eruptions. 9780123859389

Cole PD, Augusto N, Baxter PJ (2015) Hazards from Pyroclastic Density Currents, 2nd edn. Elsevier Inc., Amsterdam. https://doi.org/10.1016/b978-0-12-N00054-7. https://doi.org/10.1016/B978-0-12-385938-9.00054-7

Criswell CW (1987) Chronology and pyroclastic stratigraphy of the May 18, 1980, eruption of Mount St. Helens, Washington. J Geophys Res 92(B10):10237–10266

Crowe CT, Schwarzkopf JD, Sommerfeld M, Yutaka Tsuji (2011) Multiphase flows with droplets and particles. CRC press

Crowe CT, Troutt TR, Chung JN, Davis RW, Moore EF (1995) A turbulent flow without particle mixing. Aerosol Sci Tech 22(1):135–138

Crowe CT, Schwarzkopf JD, Sommerfeld M, Tsuji Y (1997) Multiphase Flows with Droplets and Particles. CRC Press, USA

Degruyter W, Bonadonna C (2013) Impact of wind on the condition for column collapse of volcanic plumes. Earth Planet Sci Lett 377-378:218–226. https://doi.org/10.1016/j.epsl.2013.06.041 ISBN 0012-821X

Del Bello E, Taddeucci J, Vitturi MM, Scarlato P (2017) Effect of particle volume fraction on the settling velocity of volcanic ash particles: insights from joint experimental and numerical simulations. Nature Publishing Group. https://doi.org/10.1038/srep39620

Di Muro A, Neri A, Rosi M (2004) Contemporaneous convective and collapsing eruptive dynamics: The transitional regime of explosive eruptions. Geophys Res Lett 31(10):2001–2004

Di Muro A, Rosi M, Aguilera E, Barbieri R, Massa G, Mundula F, Pieri F (2008) Transport and sedimentation dynamics of transitional explosive eruption columns: the example of the 800 BP Quilotoa plinian eruption (Ecuador). J Volcanol Geotherm Res 174(4):307–324. https://doi.org/10.1016/j.jvolgeores.2008.03.002

Dobran F, Neri A (1993) Numerical simulation of collapsing volcanic columns. J Geophys Res 98(92):4231–4259. https://doi.org/10.1029/92JB02409

Dufek J, Bergantz GW (2007) Suspended load and bed-load transport of particle-laden gravity currents: the role of particle-bed interaction. Theor Comput Fluid Dyn 21(2):119–145.

https://doi.org/10.1007/s00162-007-0041-6. ISBN 0935-4964

Dufek J, Ongaro TE, Olivier R (2015) Pyroclastic Density Currents, 2nd edn. Elsevier Inc., Amsterdam. https://doi.org/10.1016/B978-0-12-385938-9.00035-3

Durant AJ, Shaw RA, Rose WI, Mi Y, Ernst GGJ (2008) Ice nucleation and overseeding of ice in volcanic clouds. J Geophys Res Atmos 113(9):1–13. https://doi.org/10.1029/2007JD009064

Van Eaton AR, Amigo Á, Bertin D, Mastin LG, Giacosa R, González J, Valderrama O, Fontijn K, Behnke SA (2016) Volcanic lightning and plume behavior reveal evolving hazards during the April 2015 eruption of Calbuco volcano, Chile. Geophys Res Lett 43(7):3563–3571. https://doi.org/10.1002/2016GL068076

Edgar CJ, Cas RAF, Olin PH, Wolff JA, Martí J, Simmons JM (2017) Causes of complexity in a fallout dominated plinian eruption sequence: 312 ka Fasnia Member, Diego Hernández Formation, Tenerife, Spain. J Volcanol Geotherm Res 345:21–45. https://doi.org/10.1016/j.jvolgeores.2017.07.008

Elghobashi S (1994) On predicting particle-laden turbulent flows. Appl Sci Res 52:309–329

Elghobashi S, Truesdell GC (1993) on the 2-Way interaction between homogeneous turbulence and dispersed solid particles.1. turbulence modification. Phys Fluids a-Fluid Dyn 5(7):1790–1801. ISBN 0899-8213

Fischer HB (1979) Mixing in inland and coastal waters. 24/28 Oval Road. London, Academic Press

Fisher RV, Schmincke HU (1984) Pyroclastic Rocks. Springer, Berlin

Fisher RV, Orsi G, Ort M, Heiken G (1993) Mobility of a large-volume pyroclastic flow emplacement of the Campanian ignimbrite. Italy. 56(1)

Girault F, Carazzo G, Tait S, Ferrucci F, Kaminski É (2014) The effect of total grain-size distribution on the dynamics of turbulent volcanic plumes. Earth Planet Sci Lett 394:124–134

Glaze LS, Baloga SM, Wilson L (1997) Transport of atmospheric water vapor by volcanic eruption columns. J Geophys Res Atmos 102(5):6099–6108. https://doi.org/10.1029/96jd03125

Hahn GA, William IR, Thomas M (1979) Geochemical correlation of genetically related rhyolitic ash- flow and air-fall ashes, central and western Guatemala and the equatorial Pacific. Geological Society of America

Hall B, Meiburg E, Kneller B (2008) Channel formation by turbidity currents: Navier-Stokes-based linear stability analysis. J Fluid Mech 615:185–210. https://doi.org/10.1017/S0022112008003467

Herzog M, Graf HF (2010) Applying the three-dimensional model ATHAM to volcanic plumes: dynamic of large co-ignimbrite eruptions and associated injection heights for volcanic gases. Geophys Res Lett 37(19):1–5. https://doi.org/10.1029/2010GL044986

Hildreth W, Fierstein J (2012) The Novarupta-Katmai Eruption of 1912 — largest eruption of the Twentieth Century: Centennial Perspectives. US Geological Survey Professional Paper. 1411333802

Holasek RE, Self S, Woods AW (1996) Satellite observations and interpretation of the 1991 Mount Pinatubo eruption plumes. J Geophys Res 101(B12):27635–27655. https://doi.org/10.1029/96JB01179. http://doi.wiley.com/10.1029/96JB01179

Holford JM, Linden PF (1999) Turbulent mixing in a stratified fluid. Dyn Atmos Oceans 30(2):173–198

Hooft EEE, Heath BA, Toomey DR, Paulatto M, Papazachos CB, Nomikou P, Morgan JV, M R Warner (2019) Seismic imaging of santorini: subsurface constraints on caldera collapse and present-day magma recharge. Earth Planet Sci Lett 514:48–61. https://doi.org/10.1016/j.epsl.2019.02.033

Hoque MM, Mitra S, Sathe MJ, Joshi JB, Evans GM (2016) Experimental investigation on modulation of homogeneous and

isotropic turbulence in the presence of single particle using time-resolved PIV. Chem Eng Sci 153:308–329

Houghton B, Carey RJ (2015) Pyroclastic Fall Deposits, 2nd edn. Elsevier Inc., Amsterdam. https://doi.org/10.1016/B978-0-12-385938-9.00034-1

Houghton BF, Wilson CJN, Fierstein J (2004) Complex proximal deposition during the Plinian eruptions of 1912 at Novarupta, Alaska. Bulletin of Volcanology. https://doi.org/10.1007/s00445-003-0297-7

Hoyal DCJD, Bursik I, Atkinson F (1999) Settling-driven convection: a mechanism of sedimentation from stratified fluids. J Geophys Res 104:7953–7966

Hunt GR, Burridge HC (2015) Fountains in industry and nature. Ann Rev Fluid Mech 47(1):195–220. https://doi.org/10.1146/annurev-fluid-010313-141311

Huybers P, Langmuir C (2009) Feedback between deglaciation, volcanism, and atmospheric CO2. Earth Planet Sci Lett 286(3-4):479–491. https://doi.org/10.1016/j.epsl.2009.07.014

Hwang W, Eaton JK (2006) Homogeneous and isotropic turbulence modulation by small heavy ($ St \sim 50$) particles. J Fluid Mech 564:361–393

Jessop DE, Jellinek AM (2014) Effects of particle mixtures and nozzle geometry on entrainment into volcanic jets. Geophys Res Lett 41(11):3858–3863. https://doi.org/10.1002/2014GL060059

Jessop DE, Gilchrist J, Jellinek AM, Roche O (2016) Are eruptions from linear fissures and caldera ring dykes more likely to produce pyroclastic flows? Earth Planet Sci Lett 454:142–153. https://doi.org/10.1016/j.epsl.2016.09.005

Kaminski E, Tait S, Ferrucci F, Martet M, Hirn B, Husson P (2011) Estimation of ash injection in the atmosphere by basaltic volcanic plumes : the case of the Eyjafjallajökull 2010 eruption. J Geophysical Res. 116:1–10. https://doi.org/10.1029/2011JB008297

Kaminski É, Jaupart C (2001) Marginal stability of atmospheric eruption columns and pyroclastic flow generation. J Geophys Res 106(B10):21785. https://doi.org/10.1029/2001JB000215. ISBN 0148-0227. http://doi.wiley.com/10.1029/2001JB000215

Kaminski E, Tait S, Carazzo G (2005) Turbulent entrainment in jets with arbitrary buoyancy. J. Fluid Mech. 526:361–376. https://doi.org/10.1017/ S0022112004003209

Kolmogorov AN (1941) The local structure of turbulence in incompressible viscous fluid for very large Reynolds numbers. Proc R Soc London. Ser A-Math Phys Sci 434(1890):9–13. https://doi.org/10.1098/rspa.1991.0075. ISBN 0962-8444

Kotsovinos NE (2000) Axisymmetric submerged instrusion in stratified fluid. J Hydraul Eng 126(6):446–456. https://doi.org/0733-9429/00/0006-0446-0456

Koyaguchi T, Suzuki YJ (2018) The condition of eruption column collapse: 1. A reference model based on analytical solutions. https://doi.org/10.1029/2017JB015308.

Koyaguchi T, Masami T (1993) Origin of the giant eruption cloud of Pinatubo, June 15, 1991. J Volcanol Geotherm Res 55(1-2):85–96. https://doi.org/10.1016/0377-0273(93)90091-5. ISBN 0377-0273

Lherm V, Jellinek AM (2019) Experimental constraints on the distinct effects of ash, lapilli, and larger pyroclasts on entrainment and mixing in volcanic plumes. Bull Volcanol 81(12):1–11. https://doi.org/10.1007/s00445-019-1329-2

Lin W, Armfield SW (2004) Direct simulation of fountains with intermediate Froude and Reynolds numbers. ANZIAM J 45:66. https://doi.org/10.21914/anziamj.v45i0.873

Linden PF (2000) Convection in the environment. In: Perspectives in fluid dynamics: a collective introduction to current research. Cambridge University Press, Cambridge, pp 289–345

Linden PF (1979) Mixing in stratified fluids. Geophys Astrophys Fluid Dyn 13(1):3–23

Lipman PW, Mullineaux DR (1981) The 1980 eruptions of Mount St Helens. U.S. Geological Survey Professional Paper, Washington

Lirer L, Pescatore T, Booth B, Walker GPL (1973) Two Plinian pumice-fall deposits from Somma-Vesuvius, Italy. Bull Geol Soc Am 84(3):759–772. https://doi.org/10.1130/0016-7606(1973)84<759:TPPDFS>2.0.CO;2

Mallouppas G, George WK, van Wachem BGM (2017) Dissipation and inter-scale transfer in fully coupled particle and fluid motions in homogeneous isotropic forced turbulence. Int J Heat Fluid Flow 67:74–85

Manzella I, Bonadonna C, Phillips JC, Monnard H (2015) The role of gravitational instabilities in deposition of volcanic ash. Geology 43(3):211–214. https://doi.org/10.1130/G36252.1

Mastin LG, Guffanti M, Servranckx R, Webley P, Barsotti S, Dean K, Durant A, Ewert JW, Neri A, Rose WI, Schneider D, Siebert L, Stunder B, Swanson G, Tupper A, Volentik A, Waythomas CF (2009) A multidisciplinary effort to assign realistic source parameters to models of volcanic ash-cloud transport and dispersion during eruptions. J Volcanol Geotherm Res 186(1-2):10–21. https://doi.org/10.1016/j.jvolgeores.2009.01.008

Michaud-Dubuy A, Carazzo G, Kaminski E, Girault F (2018) A revisit of the role of gas entrapment on the stability conditions of explosive volcanic columns. J Volcanol Geotherm Res 357:349–361. https://doi.org/10.1016/j.jvolgeores.2018.05.005

Mingotti N, Woods AW (2016) On turbulent particle fountains. J Fluid Mech 793:1. https://doi.org/10.1017/jfm.2016.167

Mittal T, Delbridge B (2019) Detection of the 2012 Havre submarine eruption plume using Argo floats and its implications for ocean dynamics. Earth and Planetary Science Letters 511:105–116. https://doi.org/10.1016/j.epsl.2019.01.035

Morton BR, Taylor G, Turner JS (1956) Turbulent gravitational convection from maintained and instantaneous sources. Proc R Soc A Math Phys Eng Sci 234(1196):1–23. https://doi.org/10.1098/rspa.1956.0011. 00804630

Morton BR (1959) Forced plumes. J Fluid Mech 5(1):151–163

Neri A, Dobran F (1994) Influence of eruption parameters on the thermofiuid dynamics of collapsing volcanic columns. J Geophys Res 99(B9):11833–11857

Neri A, Di Muro A, Mauro R (2002) Mass partition during collapsing and transitional columns by using numerical simulations. J Volcanol Geotherm Res 115(1-2):1–18. https://doi.org/10.1016/S0377-0273(01)00304-3. ISBN 0377-0273

Newhall C, Self S, Robock A (2018) Anticipating future Volcanic Explosivity Index (VEI) 7 eruptions and their chilling impacts. Geosphere 14(2):572–603. https://doi.org/10.1130/GES01513.1

Nomikou P, Carey S, Papanikolaou D, Croff Bell K, Sakellariou D, Alexandri M, Bejelou K (2012) Submarine volcanoes of the Kolumbo volcanic zone NE of Santorini Caldera, Greece. Global Planet Change 90-91:135–151. https://doi.org/10.1016/j.gloplacha.2012.01.001.2107274096 https://doi.org/10.1016/j.gloplacha.2012.01.001

Ogden DE, Glatzmaier GA, Wohletz KH (2008) Effects of vent overpressure on buoyant eruption columns. Implications for plume stability. https://doi.org/10.1016/j.epsl.2008.01.014. www.elsevier.com/locate/epsl

Oster G, Masahide Y (1963) Density gradient techniques. Chem Rev 63(3):257–268. https://doi.org/10.1021/cr60223a003. ISBN 0009-2665

Ozmidov RV (1965) On the turbulent exchange in a stably stratified ocean. Atmos Oceanic Phys Series1 1(8):853–860

Pacheco-Hoyos JG, Aguirre-Díaz GJ, Dávila-Harris P (2018) Boiling-over dense pyroclastic density currents during the formation of the ~ 100 km3 Huichapan ignimbrite in Central Mexico: Stratigraphic and lithofacies analysis. J Volcanol Geotherm Res 349:268–282. https://doi.org/10.1016/j.jvolgeores.2017.11.007

Paladio-Melasantos ML, Solidum RU, Scott WE, Quiambao RB, Umbal JV, Rodolfo KS, Tubianosa BS, Delos Reyes PJ, Alonso RA, Ruerlo HB (1996) Tephra falls of the 1991 eruptions of Mount Pinatubo. Fire and mud ;eruptions and lahars of Mount Pinatubo Philippines, Philippine Institute of Volcanology and Seismology, Quezon City

Papale P, Mauro R (1993) A case of no-wind plinian fallout at Pululagua caldera (Ecuador): implications for models of clast dispersal. Bull Volcanol 55(7):523–535. https://doi.org/10.1007/BF00304594. ISBN 1538-3652 (Electronic)\r0003-987X (Linking)

Pope EL, Jutzeler M, Cartigny MJB, Shreeve J, Talling PJ, Wright IC, Wysoczanski RJ (2018) Origin of spectacular fields of submarine sediment waves around volcanic islands. Earth Planet Sci Lett 493:12–24. https://doi.org/10.1016/j.epsl.2018.04.020

Prata F, Bill R (2015) Volcanic ash hazards to aviation, 2nd edn. Elsevier Inc., Amsterdam. https://doi.org/10.1016/b978-0-12-N00052-3. https://doi.org/10.1016/B978-0-12-385938-9.00052-3

Prata F, Woodhouse M, Huppert HE, Prata A, Thordarson T, Carn S (2017) Atmospheric processes affecting the separation of volcanic ash and SO2 in volcanic eruptions: Inferences from the May 2011 Grímsvötn eruption. Atmos Chem Phys 17(17):10709–10732. https://doi.org/10.5194/acp-17-10709-2017

Raju N, Meiburg E (1997) Dynamics of small, spherical particles in vortical and stagnation point flow fields. Phys Fluids (1994-present) 9(2):299–314

Rampino M. R., S. Self (1992) Volcanic Winter and Accelerated Glaciation Following the Toba Super-Eruption. Letters to Nature 359(September):50–52

Ridley DA, Solomon S, Barnes JE, Burlakov VD, Deshler T, Dolgii SI, Herber AB, Nagai T, Neely RR, Nevzorov AV, Ritter C, Sakai T, Santer BD, Sato M, Schmidt A, Uchino O, Vernier JP (2014) Total volcanic stratospheric aerosol optical depths and implications for global climate change. Geophys Res Lett 41(22):7763–7769. https://doi.org/10.1002/2014GL061541

Robock A (2015) Climatic Impacts of Volcanic Eruptions, 2nd edn. Elsevier Inc., Amsterdam. https://doi.org/10.1016/B978-0-12-385938-9.00053-5

Roche O, Buesch DC, Valentine GA (2016) Slow-moving and far-travelled dense pyroclastic flows during the Peach Spring super-eruption. Nature Commun 7:1–8. https://doi.org/10.1038/ncomms10890

Roche O, Niño Y, Mangeney A, Brand B, Pollock N, Valentine GA (2013) Dynamic pore-pressure variations induce substrate erosion by pyroclastic flows. Geology 41(10):1107–1110. https://doi.org/10.1130/G34668.1

Romero JE, Morgavi D, Arzilli F, Daga R, Caselli A, Reckziegel F, Viramonte J, Diaz-Alvarado J, Polacci M, Burton M, Perugini D (2016) Eruption dynamics of the 22-23 April 2015 Calbuco Volcano (Southern Chile) Analyses of tephra fall deposits. J Volcanol Geotherm Res 317(April 2015):15–29. https://doi.org/10.1016/j.jvolgeores.2016.02.027

Rosi M, Paladio-Melosantos ML, Di Muro A, Leoni R, Bacolcol T (2001) Fall vs flow activity during the 1991 climactic eruption of Pinatubo Volcano (Philippines). Bull Volcanol 62(8):549–566. https://doi.org/10.1007/s004450000118

Rotella MD, Wilson CJN, Barker SJ, Wright IC (2013) Highly vesicular pumice generated by buoyant detachment of magma in subaqueous volcanism. Nature Geosci 6(2):129–132. https://doi.org/10.1038/ngeo1709

Rowley PD, Kuntz MA, Macleod NS (1981) Pyroclastic-flow deposits. In: Lipman PW, Mullineaux DR (eds) The 1980 eruptions of mount st. helens, washington. Geological Survey Profession54 al Paper 1250. U.S. Geological Society

Schmidt A, Carslaw KS, Mann GW, Wilson M, Breider TJ, Pickering SJ, Thordarson T (2010) The impact of the 1783-1784 AD Laki eruption on global aerosol formation processes and cloud condensation nuclei. Atmos Chem Phys 10(13):6025–6041. https://doi.org/10.5194/acp-10-6025-2010

Schmidt A, Carslaw KS, Mann GW, Rap A, Pringle KJ, Spracklen DV, Wilson M, Forster PM (2012) Importance of tropospheric volcanic aerosol for indirect radiative forcing of climate. Atmos Chem Phys 12(16):7321–7339. https://doi.org/10.5194/acp-12-7321-2012

Scollo S, Bonadonna C, Manzella I (2017) Settling-driven gravitational instabilities associated with volcanic clouds : new insights from experimental investigations. Bulletin of Volcanology 79. https://doi.org/10.1007/s00445-017-1124-x

Scott WE, Hoblitt RP, Torres RC, Self S, Martinez MML, Nillos Jr. T (1996) Pyroclastic flows of the June 15, 1991, climactic eruption of Mount Pinatubo. University of Washington Press

Thomas S, Gurioli L, Houghton BF, Cioni R, Cashman KV (2011) Column collapse and generation of pyroclastic density currents during the A.D. 79 eruption of Vesuvius: the role of pyroclast density. Geology 39(7):695–698. https://doi.org/10.1130/G32092.1. 00917613

Sigurdsson H, Carey SN, Fisher RV (1987) The 1982 eruptions of El Chichon volcano, Mexico (3): physical properties of pyroclastic surges. Bulletin of Volcanology

Smith IEM, Stewart RB, Price RC (2003) The petrology of a large intra-oceanic silicic eruption: the Sandy Bay Tephra, Kermadec Arc, Southwest Pacific. J Volcanol Geotherm Res 124(3-4):173–194. https://doi.org/10.1016/S0377-0273(03)00040-4

Sparks RSJ (1986) The dimensions and dynamics of volcanic eruptions columns. Bulletin of Volcanology

Suñe-puchol I, Aguirre-díaz GJ, Dávila-harris P, Miggins DP, Pedrazzi D, Costa A, Ortega-obregón C, Lacan P, Hernández W, Eduardo G (2019) The Ilopango caldera complex, El Salvador : Origin and early ignimbrite-forming eruptions of a graben / pull-apart caldera structure. J Volcanol Geotherm Res 371:1–19. https://doi.org/10.1016/j.jvolgeores.2018.12.004

Suzuki YJ, Costa A, Cerminara M, Ongaro TE, Herzog M, Van Eaton AR, Denby LC (2016) Inter-comparison of three-dimensional models of volcanic plumes. J Volcanol Geotherm Res 326:26–42. https://doi.org/10.1016/j.jvolgeores.2016.06.011

Suzuki YJ (2005) A numerical study of turbulent mixing in eruption clouds using a three-dimensional fluid dynamics model. J Geophys Res 110:1–18. https://doi.org/10.1029/2004JB003460

Suzuki YJ, Takehiro K (2013) 3D numerical simulation of volcanic eruption clouds during the Shinmoe-dake eruptions. Earth Planets Space 65:581–589. https://doi.org/10.5047/eps.2013.03.009

Tani K, Fiske RS, Tamura Y (2008) Sumisu volcano, Izu-Bonin arc, Japan: site of a silicic caldera-forming eruption from a small open-ocean island. Bull Volcanol 70:547–562. https://doi.org/10.1007/s00445-007-0153-2

Thomson DJ (1982) Spectrum estimation and harmonic analysis. IEEE 70(9):1055–1096

Tsampouraki-Kraounaki K, Dimitris S (2018) Seismic stratigraphy and geodynamic evolution of Christiana Basin, South Aegean Arc. Marine Geology 399(January):135–147. https://doi.org/10.1016/j.margeo.2018.02.012

Turner JS (1966) Jets and plumes with negative or reversing buoyancy. J Fluid Mech 26(4):779–792. https://doi.org/10.1017/S0022112066001526

Turner JS (1979) Buoyancy effects in fluids. The Pitt Building, Trumpington Street. Cambridge University Press, Cambridge

Turner JS (1986) Turbulent Entrainment: the development of the entrainment assumption, and its application to geophysical flows. J Fluid Mech 173:431–471

Valentine GA, Gregg TKP (2008) Continental basaltic volcanoes - Processes and problems. J Volcanol Geotherm Res 177(4):857–873. https://doi.org/10.1016/j.jvolgeores.2008.01.050

Valentine GA, Giannetti B (1995) Single pyroclastic beds deposited by simultaneous fallout and surge processes: Roccamonfina volcano, Italy. J Volcanol Geotherm Res 64(1-2):129–137. https://doi.org/10.1016/0377-0273(94)00049-M

Valentine GA, Wohletz KH (1989) Numerical models of plinian eruption columns and pyroclastic flows. J Geophysical Res. 94(B2) 1867–1887

Van Eaton AR, Herzog M, Wilson CJN, McGregor J (2012) Ascent dynamics of large phreatomagmatic eruption clouds: the role of microphysics. J Geophys Res Solid Earth 117(3):1–23. https://doi.org/10.1029/2011JB008892. ISBN 0148-0227

Veitch G, Woods AW (2000) Particle recycling and oscillations of volcanic eruption columns. J Geophys Res 105(B2):2829–2842

Wadge G, Voight B, Sparks RSJ, Cole PD, Loughlin SC, Robertson REA (2014) An overview of the eruption of Soufriére Hills Volcano, Montserrat from 2000 to 2010. Geological Society, London, Memoirs

Walker GPL (1973) Explosive volcanic eruptions - a new classification scheme. Geologische Rundschau 62

Walker GPL, Croasdale R (1970) Two Plinian-type eruptions in the Azores. J Geol Soc 127:17–55

Wang H, Law AW (2002) Second-order integral model for a round turbulent buoyant jet. J Fluid Mech 459:397–428. https://doi.org/10.1017/S0022112002008157

White JDL, Ian Schipper C, Kano K (2015) Submarine explosive eruptions, 2nd edn. Elsevier Inc., Amsterdam. https://doi.org/10.1016/B978-0-12-385938-9.00031-6

Wilson CJN (2001) The 26.5 ka Oruanui eruption, New Zealand: an introduction and overview. J Volcanol Geotherm Res 112(1-4):133–174. https://doi.org/10.1016/S0377-0273(01)00239-6. 6473748199

Wilson CJN, Hildreth W (1997) The bishop tuff: new insights from eruptive stratigraphy. J Geol 105(4):407–440. https://doi.org/10.1086/515937. https://www.journals.uchicago.edu/doi/10.1086/515937

Wilson CJN (1993) Stratigraphy, chronology, styles and dynamics of late Quaternary eruptions from Taupo volcano. New Zealand

Wilson CJN, Hildreth W (1998) Hybrid fall deposits in the Bishop Tuff, California: a novel pyroclastic depositional mechanism. Geology 26(1):7–10. https://doi.org/10.1130/0091-7613(1998)026<0007:HFDITB>2.3.CO;2

Woodhouse MJ, Hogg AJ, Phillips JC, Sparks RSJ (2013) Interaction between volcanic plumes and wind during the 2010 Eyjafjallajökull eruption, Iceland. J Geophys Res Solid Earth 118(1):92–109

Woods AW (1988) The fluid dynamics and thermodynamics of eruption columns. Bull Volcanol 50:169–193

Woods AW (1995) The dynamics of volcanic eruption columns. Rev Geophys 33:356–360

Woods AW (2010) https://doi.org/10.1146/annurev-fluid-121108-145430. 0066-4189. http://www.annualreviews.org/doi/10.1146/annurev-fluid-121108-145430. Ann Rev Fluid Mech 42(1):391–412

Woods AW, Caulfield CP (1992) A laboratory sudy of explosive volcanic eruptions. J Geophys Res 97:6699–6712

Woods AW, Wohletz K (1991) Dimensions and dynamics of co-ignimbrite eruption columns. Nature 350(6315):225–227. https://doi.org/10.1038/350225a0. http://www.nature.com/doifinder/10.1038/350225a0

Wright IC, Worthington TJ, Gamble JA (2006) New multibeam mapping and geochemistry of the 30°-35° S sector, and overview, of southern Kermadec arc

Publisher's Note Springer Nature remains neutral with regard to jurisdictional claims in published maps and institutional affiliations.